Al_2O_3 layers deposited by atomic layer deposition for surface passivation and passivated contacts in high efficiency silicon based solar cells

Eirik Koch Jubskås

Thesis submitted for the degree of
Master in Materials Science and Nanotechnology
60 credits

Department of Chemistry
Faculty of mathematics and natural sciences

UNIVERSITY OF OSLO

Spring 2020

Al_2O_3 Layers Deposited by Atomic Layer Deposition for Surface Passivation and Passivated Contacts in High Efficiency Silicon Based Solar Cells

Eirik Koch Jubskås

© 2020 Eirik Koch Jubskås

Al_2O_3 Layers Deposited by Atomic Layer Deposition for Surface Passivation and Passivated Contacts in High Efficiency Silicon Based Solar Cells

http://www.duo.uio.no/

Printed: Reprosentralen, University of Oslo

Abstract

Al_2O_3 Layers Deposited by Atomic Layer Deposition for Surface Passivation and Passivated Contacts in High Efficiency Silicon Based Solar Cells

Dielectric surface passivation for solar cell technology have been extensively research previously, and one of the main breakthroughs within this field is atomic layer deposited AlO_x. AlO_x have been successful for two reasons; firstly, the high degree of chemical passivation, and secondly, the high concentration of fixed negative charges, leading to a high degree of field-effect passivation as well.

One of the objectives for this work is to present a deposition process optimized for passivation and investigate the different process parameters' effect on the surface recombination velocity (SRV). We conclude that the passivation quality of the films is highly temperature dependent, both during deposition and during post deposition annealing. The lowest SRV achieved was 0.4 cm/s and was obtained for a deposition temperature of 100 °C and a 400 °C annealing. However, good passivation has been achieved for temperatures between 50 °C and 200 °C, as well, with average values ranging from 3.52 cm/s to 14.2 cm/s. The concentration of fixed negative charges in the films, Q_f, was determined to range between $-5.2453 \cdot 10^{11}\ cm^{-2}$ and -$3.6173 \cdot 10^{12}\ cm^{-2}$ acquired using Capacitance-Voltage-measurements. Photoluminescence imaging under applied bias have been performed on the sample with highest concentration of negative charges, which was determined to be at $-2.5 \cdot 10^{12}\ cm^{-2}$. Both methods showed comparable results to previous work.

Simulations of a MIS structure with an ultrathin AlO_x layer have been performed in order to try identifying the oxide thickness range for quantum tunneling. A correlation between threshold voltage for quantum mechanical tunneling and insulator thicknesses was determined from these simulations.

A hybrid PEDOT:PSS / Si solar cell with ultrathin passivating AlO_x interlayers have been fabricated and IV measurements in the dark was performed to characterize the oxides passivation quality and tunneling efficiency. One solar cell utilizing a 1.7 nm oxide showed decent IV performance, indicating some potential for the material system.

Acknowledgements

First of all, I would like to thank my wife Anette. I could not have asked for a better home office colleague the last few months. A big thanks to my team of supervisors; Dr. Halvard Haug, thank you for me guiding through this process and being a huge source of information, readily available, almost 24/7. Dr. Kristin Bergum, thank you for introducing me to ALD, helping me with the reactor and learn about the process, and always being there to answer any questions I might have. Prof. Lasse Vines, thank you for helping me with the SIMS analysis and for just being an inspiration with regards to infinite work capacity. Prof. Erik S. Marstein, your enthusiastic being has been a great inspiration for me, always excited to see new results (even though not always great), thank you so much. Thank you all for the proof reading as well.

I would like to thank Dr. Philip M. Weiser for the FT-IR measurements and for all the great talks we've had. Thank you, Vegard S. Olsen, for giving me priority access to the lab when I needed it the most. I must also thank the team of engineers at MiNaLab, Halvor Dolva, Victor Bobal and Christoph Sieffert for their efforts in keeping the lab up and running so that we can continue to do exciting research. A big thanks to the team at the Physics I-Lab for fixing ALD parts quickly when I broke them.

Also, a big thanks to Vegard Rønning for helping out with the chamber cleaning, and for just being a good friend. Thank you, Michael N. Getz, for all the great discussions. Thank you, Erlend Hall, for the collaboration we had. I must also thank everyone at LENS and IFE, PhD's, master students, researchers and professors for all the good times and for making me feel so included. A special thanks to the LENS family, for all the cozy Zoom lunches and payday beers. I hope our paths cross again soon! Finally, I would like to thank my family and friends for being so supportive and proud of me. These have truly been strange times, for many reasons, but you have all made it so much better.

Table of Contents

Abstract ... *vi*

Acknowledgements ... *vii*

1 Introduction ... *1*

2 Theory ... *3*

2.1 Semiconductor Physics ... 3

2.1.1 Doping ... 6

2.1.2 Pn-junctions ... 8

2.1.3 Generation and recombination ... 13

2.2 Surface Passivation ... 19

2.2.1 AlO_x for Surface Passivation ... 22

2.3 Quantum Mechanical Tunneling ... 23

2.4 The Solar cell ... 25

2.4.1 Basic Solar Cell Physics ... 25

2.4.2 The effects of Surface Passivation ... 29

2.4.3 Solar Cell Passivation Schemes ... 30

3 Experimental Methods ... *35*

3.1 Atomic Layer Deposition ... 35

3.1.1 Process Description ... 35

3.1.2 Advantages and Shortcomings ... 39

3.2 Sample Processing ... 40

3.2.1 Sample cleaning ... 40

3.2.2 Thermal Atomic Layer Deposition ... 41

3.2.3 Annealing ... 42

3.2.4 Metallization ... 43

3.3 Characterization techniques and Sample Analysis ... 44

3.3.1 Spectroscopic Ellipsometry ... 45

3.3.2 Capacitance-Voltage Measurements ... 45

3.3.3 Quasi Steady-state Photoconductance ... 47

3.3.4 Photoluminescence Imaging 48

3.3.5 Photoluminescence Imaging under applied Voltage 50

3.3.6 Secondary Ion Mass Spectrometry 53

3.3.7 Fourier Transform Infrared Spectroscopy 53

4 Results and Discussion 55

4.1 Passivation Process Development and Optimization 55

4.1.1 Initial Experiment 55

4.1.2 Surface Passivation Quality 56

4.2 Cross Contamination of the ALD System 65

4.2.1 The effect on lifetime 65

4.2.2 Determining the Impurity Species 66

4.2.3 Cleaning Procedure and the Effects on Passivation Quality 72

4.3 Characterization of MIS-structures – Determining Qf 73

4.3.1 CV measurements 73

4.3.2 PL-V 76

4.4 AlO_x as a Tunneling Oxide Material 77

4.4.1 Simulations of I-V characteristic of MIS-structures 78

4.4.2 I-V measurements of PEDOT:PSS / AlO_x / Si solar cells 80

5 Conclusion and Further Work 82

5.1 Conclusion 82

5.2 Further Work 83

6 Bibliography 84

Appendix A – CV-analysis code (python) 94

Appendix B - Silvaco MIS simulation code 99

1 Introduction

In order to meet the ever-growing energy demand of the world, and simultaneously reduce the amount of pollution into the atmosphere, humanity is in dire need of several clean and renewable energy sources. One of the most promising and fastest expanding techniques of generating green energy is the use of the photovoltaic (PV) effect. If this effect is utilized correctly, it directly converts sunlight into usable electricity for the power grid. This is done by using solar panels, which consist of several solar cells connected and mounted together. Up until around year 2000, solar panels have mostly been used in a small scale to provide power in remote locations, too far away from the main grid to be able to connect to it (e.g. cabins, light houses, etc.). However, for the last twenty years, there has been a significant growth in the volume of the industry, and in 2017 the PV industry grew faster than any other power generating industry [1]. This production volume has resulted in a substantial reduction in the prices of solar panels, making the installation cost a large portion of the price, therefore it is essential to have the highest energy conversion efficiency possible. Now, technologies based on crystalline Si (c-Si) wafers give the lowest solar electricity cost compared to other solar cell technologies. This parameter is measured in $/$W_p$, where W_p is the power output at peak production in watts. Because of its low cost, c-Si technology dominated the market with a share of ~90% in 2018 [2].

The Si wafer accounts for a substantial part of the cell cost, so in order to keep decreasing the cost of the cells, it is desired to decrease the wafer thickness. However, reduced thickness leads to challenges regarding incomplete absorption of charge carriers due to insufficient absorption (transmission losses), and partly by incomplete collection of charge carriers, as a larger fraction of the electron-hole pairs (EHP) are lost at the surface in a process called recombination. This means that the photo exited EHPs in the cell does not escape the cell and therefore is not available to us as usable current. A lower charge carrier concentration also lowers the voltage of the cell, and both of these mechanisms leads to loss in the conversion efficiency. A substantial part of the recombination in Si solar cells takes place at the surface, and at the metal contacts to the exterior electrical circuit. A solution to the surface recombination loss issue is to passivate these areas, which means to alter the electrical properties there, preventing parts of the recombination processes.

Surface passivation are being achieved by coating the Si surface with different materials, including SiN_x, Al, as well as SiO_2 [3]. However, it is SiN_x and Al Back Surface Field (Al-BSF) that are the most studied and widely used for surface passivation purposes in the industry compared to SiO_2. It should be noted that SiO_2 can be used as a thick isolating back layer. For the SiN_x front side case, the material is deposited at the front of the cell by plasma enhanced chemical vapor deposition (PECVD). The precursors used for this technique (SiH_4, NH_3) is very rich in hydrogen, which is incorporated in the film because of the low deposition temperature. Thus, the technique has the added benefit that H can provide bulk passivation, so the process is beneficial from that aspect as well. SiN_x can be used to cap a thin insulating oxide layer with local contacts which usually covers 1-5% of the backside area. This kind of cell is called a Passivated Emitter and Rear Contact (PERC) cell [4]. Al_2O_3 is a material that have be used as surface and contact passivation as a tunneling oxide [5], [6]. It is deposited on the back side of the cell between the p-type Si in the cell wafer itself and the back metal contact. In order for the device to take advantage of the tunneling phenomena through the oxide, i.e. transfer charge carriers through it, the thickness must be 2 nm or less [6], [7]. The contact that covers this tunneling oxide needs to have high conductivity and can consist of a heavily doped poly-Si layer. Al on the other hand, works as a p-type dopant in Si, so when Al is applied as a back contact on a p-type based solar cell, Al atoms diffuse into Silicon creating the Back Surface Field. The Back Surface Field is not to be mistaken with field effect passivation, which will be described later in this thesis. Although similar in effect, there are key differences in the mechanism creating the effect.

During this project, different possibilities related to passivating contacts and surfaces of solar cells will be explored. Al_2O_3 will be deposited onto monocrystalline Si wafers by Atomic Layer Deposition (ALD), in order to have good interface quality and thickness control. The carrier lifetime measurements have been done using techniques like photoluminescence (PL) imaging and quasi steady state photoconductance (QSSPC), which are important measures for the passivation quality. Some electrical characterization has also been performed in order to determine the field-effect passivation, e.g. CV and PLV. Thus, both the surface passivation and tunneling currents has been studied. In addition, device simulations was considered, as to put this work into context, and to back up experimental results. The object for this work is to develop an efficient surface passivation process at MiNaLab and characterize the samples using the mentioned techniques to be able to compare the passivation quality to existing results from the literature.

2 Theory

In this chapter, the theoretical basis for this thesis will be described. First, the fundamentals relevant for the understanding of the methods and the results in this work within semiconductor physics will be presented. Material passivation will be presented next and then a small introduction to the quantum tunneling effect. In the end, some solar cell physics and principles will be explained. As silicon by far the most used material in solar cells today and is the material used for the experiments herein, the chapter will utilize this in the examples. Finally, an introduction to the principles of passivation, and surface passivation in particular will be described. The theoretical foundation for this chapter is based on the books by Streetman [8], Smets [9] and Nelson [10], as well as various published papers and reviews.

2.1 Semiconductor Physics

A semiconductor is a material which has an electrical conductivity lower than a metal and higher than an insulator. The differences in conductivity originates from the energy-bands in these materials, which are described qualitatively in Figure 2.1. Energy bands in this context refers to the range of allowed energy states for electrons, i.e. a continuum of discrete states. In the figure, one can see the highest occupied band and the lowest unoccupied band, namely the *valence band* and *conduction band*, respectively, for the three material types. The energy difference between these bands are called the bandgap. This is a characteristic property unique to every material, which describes a specific energy; the minimum energy required for exciting

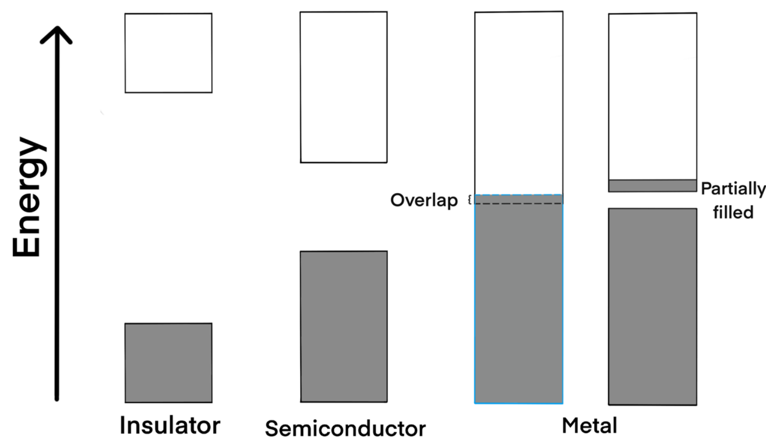

Figure 2.1: An illustration of how the valence band (grey rectangles) and conduction band (white rectangles) are relative to each other in the different material types. Metals have overlapping energy bands, or partially filled conduction bands, shown here.

an electron from the valence band up to the conduction band. This energy band gap arises from the Pauli *exclusion principle*, which states that two or more identical fermions cannot occupy the same quantum state within one quantum mechanical system [11]. In this case, the fermion considered is the electron.

When two atoms are put together to form a bond (see Figure 2.2) the binding electrons forms new states which are both consisting of an electron with positive spin and an electron with negative spin (or spin up and spin down). Some states are higher in energy, which means less chemically stable, which are antibonding, and some states are lower in energy, and therefore more chemically stable, which are bonding. This difference in energy is the energy gap and now there are two discrete energy levels. If more atoms are put together, more discrete levels are created. If so many atoms are put together that they form a material, what is effectively achieved is an infinite number of discrete energy states that can, for all practical purposes, be described as being a continuum of states from the lower energy level to the top energy level within that band [12].

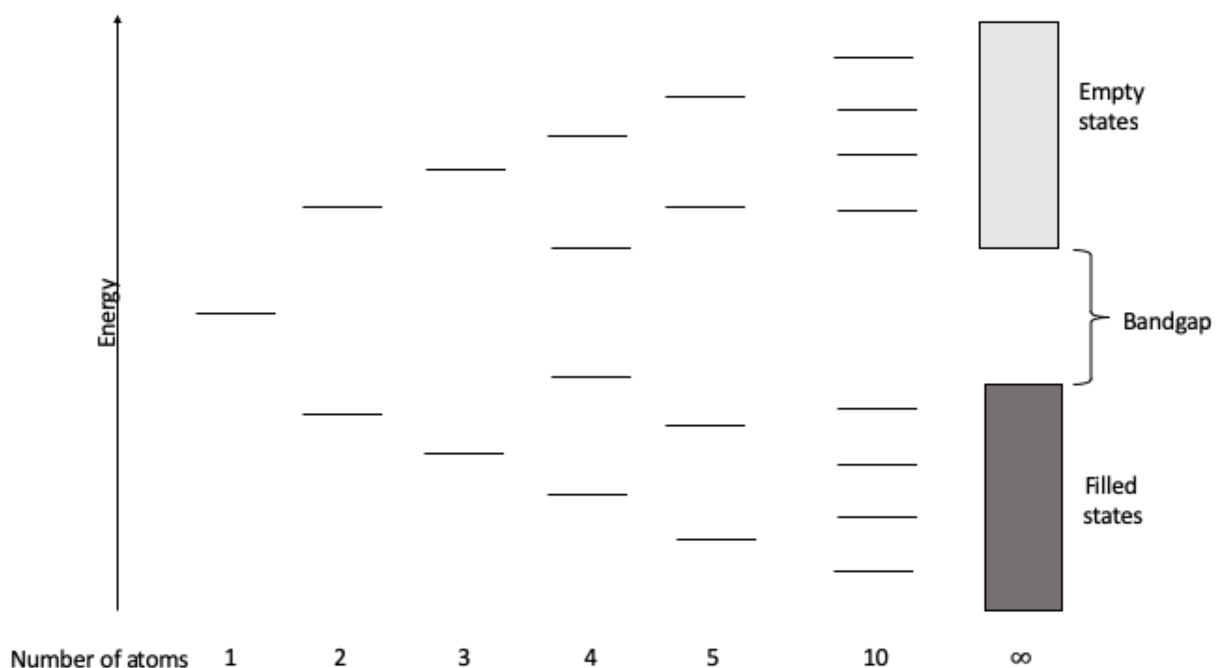

Figure 2.2: Schematic illustration of the development of energy levels from single atoms, to a solid material. This illustration is of a semiconducting material.

In an insulator the energy gap is larger compared to semiconductors. Because of its size in insulators, a high amount of energy is required to excite electrons from the fully occupied valence band up to the empty conduction band, making the material unable to conduct any

electrical current under non-extreme conditions. For metals, on the other hand, the highest occupied band is only partially full, giving the electrons room to move around almost freely, hence the high conductivity of metals. At 0K, semiconductors are like insulators in the fact that the valence band is full, and the conduction band is empty, however, the bandgap of a semiconductor is smaller. Because of this, electrons only need a little "push" of optical, electrical or thermal energy to be able to cross the bandgap and enter the conduction band [8]. The thermally excited electrons come from the fact that the heat supplied to the material can give enough energy to push some electrons over the energy barrier, hence increasing conductivity. This can occur as soon as the material temperature is above 0K.

Electrons within a solid compound can be described by *Fermi-Dirac statistics* [8, pp. 109-112]. This is the probability that an available energy state in the material is occupied by an electron, at a given temperature, and is given in equation (1) as,

$$f(E) = \frac{1}{1 + e^{(E-E_F)/kT}}, \qquad (1)$$

where E is the energy level of the state, E_F is the fermi energy, k is Boltzmann's constant and T is the temperature in kelvin. At 0 K the probability of occupancy is 1 up to the fermi energy, E_F, then falls abrupt to 0, which implies that all available states up to E_F are filled and all available states above E_F are empty.

It is known that the electron concentration in the conduction band is equal to the *hole* concentration in the valence band in a perfect material (the concept of a "hole" will be explained in Section 2.1.1., but for now consider it as a positive particle that can be described by similar physics as an electron), and that semiconductors does not have any available states inside the bandgap. This is only for a perfect, undoped material. In a real material, defect states inside the bandgap often occur. Since the probability of a state at E_F being occupied is 0.5 and the Fermi distribution is symmetrical around E_F, we can conclude that the Fermi level of an *intrinsic* semiconductor is in the center of E_g. An intrinsic semiconductor is a material where there are no *dopants* introduced (doping will be explained in the next section). This is illustrated in Figure 2.3, where f(E) is shown across the Band gap. This figure also shows the effect doping has on the charge carrier distribution. In the figure we can see that the fermi distribution function is non-zero within the bandgap, indicating that there is some probability of a state here being

occupied here. However, the function only describes the probability of occupancy of *available* states at any given energy, and there are no states inside the bandgap, hence, there are no electrons with these energies.

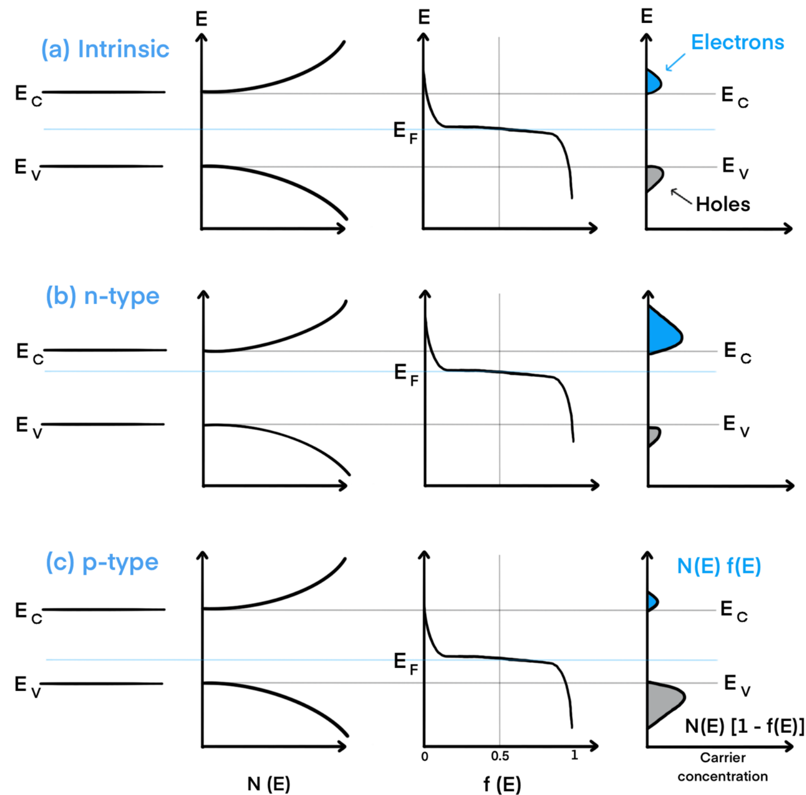

Figure 2.3: This figure shows how doping effects the density of states, fermi-distribution and carrier concentration in (a) an intrinsic, (b) a n-type and (c) a p-type semiconductor. The figure is inspired by Figure 3-16 in *[8, p. 113]***.**

In Figure 2.3 (a), an intrinsic semiconductor is shown. Here, there are some probability of having an electron in the conduction band and a hole in the valence band, although it is small. By doping the material, the Fermi level is shifted higher, as shown in Figure 2.3 (b), or lower, as in Figure 2.3 (c). Shifting the fermi level implies a shift in the carrier concentration in the material. This phenomenon emerges from introducing an energy level within the band gap, close to the conduction band or the valence band, depending on the dopant.

2.1.1 Doping

There are two main kinds of doping; one which makes electrons easier to excite up into the conduction band, and one which absorbs electrons out of the valence band, hence allowing other electrons to move within that band. These two ways are called *donor doping* and *acceptor doping*, respectively. Donor atoms introduce an extra electron into the crystal lattice, acceptor

dopants remove one electron, i.e. introduce a hole. A hole is a quasi-particle, which makes describing current transport in an acceptor doped material much easier to calculate. This will become clear in the next paragraph.

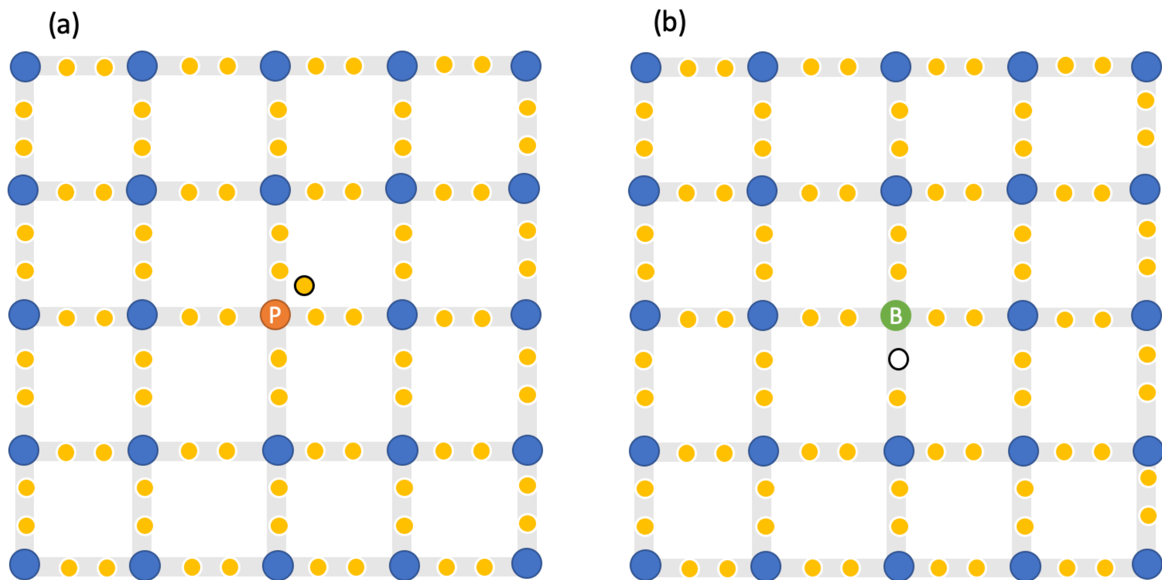

Figure 2.4: This illustrates the doping process as described by the bonding model for (a) n-type and (b) p-type doping.

When a foreign element is introduced into the compound with the purpose of doping it, an element which has a different valence from the host material is chosen. The effect of this is described in Figure 2.4 (a) and (b), for donors and acceptors, respectively. The figure shows that when a phosphorous-atom (P) is added to the crystal structure of Si, the P-atom takes a substitutional site[1]. However, P has one valence higher than Si, so there is one electron not occupied by bonding. This electron is much easier to move around compared to the electrons contributing to the chemical bonds of the material, which means that P is a donor in Si [9, pp. 50-51]. In Figure 2.4 (b) Boron (B) is at a substitutional site in Si. B has one lower valence than Si, meaning one out of the four bonds is not satisfied. At this site, the lack of one electron enables other electrons occupied in bonds to move to this spot. Now, the unsatisfied bond has moved in the crystal. To view this mechanism as electrons moving into an unoccupied state is overly complex, with so many electrons interacting with that state and each other. A simplification is to consider the empty state as a hole moving around. This is used to describe

[1]This means that the P-atom is located at a Si-position in the crystal lattice and forms a bond with the surrounding Si-atoms.

transport of charge in acceptor-doped (p-type) materials and talk about "hole current" rather than electron current.

The two types of doping discussed in the previous paragraph are essential to most of the practical uses of semiconductors. They allow us to control the conductivity of our material and it can be applied to a variety of different applications. The whole transistor industry is based upon semiconductors, and their ability to control electrical signals. And this ability emerges from doping and the formation of junctions between areas of different doping.

2.1.2 Pn-junctions

Pn-junctions form the basis for a variety of semiconductor devices, e.g. transistors, optical detectors, light emitting diodes and solar cells. This section will discuss how these junctions are fabricated and the physics making them useful for us. Si will be used as an example as it is the most commonly used semiconductor in the industry, as well as being the material used for the experiments in this work.

As discussed in a previous section, the doping of a material will alter its electrical characteristics, and one can either promote the conduction of electrons or holes by choosing different dopant atoms to incorporate into our material. However, if two regions of n- and p-type doped material are put together, the junction formed between these two regions is what is known as a pn-junction[2]. This is a *rectifying junction*, meaning it will only allow current through one direction, or with one particular bias-polarization. The origin of this will be discussed later. A pn-junction does not explicitly consist of two different materials. On the contrary, these junctions are usually made out of one material with two zones of different dopants and doping levels. This can be achieved by having a base-doping in the bulk of the material. Let us consider Si with a uniform B concentration of 10^{15}cm^{-3} (p-type), and then dope a thin n-type layer at the surface with, for instance 10^{20}cm^{-3} of P. By doping the material in this way, an effective n-type doping in the thin layer given by

$$n_0 = p_0 + N_d^+ + N_a^-, \tag{2}$$

---

[2] You could call it a np-junction and get away with it too, thought.

where n_0 is the electron concentration, p_0 is the hole concentration, N_d^+ and N_a^- is the donor and acceptor concentration, respectively. Here, the concentration grading of the P-atoms in the Si is not considered, which would change the junction to some extent.

When considering the simplified case for creating a junction like this, the junction is abrupt with no grading in dopant concentration. This is fairly close to the real case when the junction is fabricated using a technique called epitaxial growth, which will not be elaborated on in this work. However, other ways of fabricating such a structure will create a more graded junction. To visualize the abruptness of the junction considered, it is helpful to think of the two regions as separate blocks of material prior to the formation, meaning that the n-side has a uniformly high concentration of donors and electrons, and similarly for the p-side with acceptors and holes. The moment these blocks connect to form the junction, the large concentration difference between the two regions induces a flux of electrons into the p-side, and also a flux of holes into the n-side. However, as the donor atoms near the junction lose their respective electrons and simultaneously the acceptors lose their holes, the dopant atoms become charged. Hence, the n-side near the junction becomes positive and the p-side near the junction becomes negative. As this happens, an electric field arise across the junction, from the positive n-side, to the negative p-side. Thus, a drift current of both charge carriers counteracting the initial flux of carriers emerges. This current is described for electrons by equation (3),

$$J_n = q\mu_n nE - qD_n \nabla \mathrm{n}, \tag{3}$$

where q is the elementary charge, μ_n is the mobility of electrons, E is the E-field, D_n is the diffusivity and ∇n is the concentration gradient of electrons. The first part of equation (3) is the drift driven current and the second part is the diffusion driven current. At equilibrium, these currents cancel each other $\left(J_n = J_p = 0\right)$, effectively stopping any charge transport across the junction.

As these opposing currents reach equilibrium, a region with static charge s has emerged from the junction. This is called the *depletion region*, or *space charge region*, which is because the region is effectively depleted of all mobile charge carriers. The region's extent into each side of the junction is determined by the doping concentrations on each side. The number of static charges on each side must be equal to achieve equilibrium, meaning that the extend of the depletion region can be unevenly distributed. This can be seen in Figure 2.5 (a)

and Figure 2.5 (b), which leads to Figure 2.5 (c) where the electric field distribution is shown. This distribution is described by Poisson's equation, which in this instance is given by

$$\frac{dE(x)}{dx} = \frac{q}{\epsilon}(p - n + N_d^+ - N_a^-), \tag{4}$$

where ϵ electrical permittivity of the material at hand and relates the charge concentration to the electric field. When a material is doped with high concentrations of n-type doping into a moderately doped p-type material, the depletion region will extend much further into the p-type region than into the n-type region.

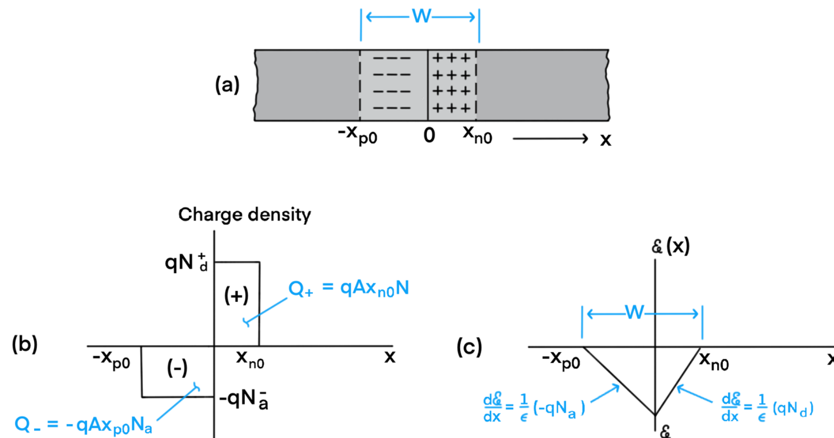

Figure 2.5: The figure shows the effect of having a higher n-type concentration than p-type in (a) the effects on the distribution of charges, $x = 0$ is the interface, (b) on the charge density and (c) on the electric field distribution. Equations in (b) describeds the number of charges in the region, and in (c) we can see Poisson's equation. The figure is inspired by Figure 5-12 in *[8, p. 201]*.

As the junction reaches equilibrium and the depletion region expansion has stopped and stabilized, a potential difference between the sides of the junction emerges (assuming the material outside of this region is neutral, which is called the depletion approximation). This is the *contact potential*, V_0. One might think that such a potential could be exploited for current, but that is not the case. The contact potential is merely an equilibrium characteristic canceling the diffusion currents. It is therefore not possible to measure this by placing a voltmeter across the device, since there would form new contact potentials at the voltmeter-probes canceling the built-in potential of the junction [8, p. 197]. The function of the contact potential is to separate the energy bands of the materials on each side of the junction. In equilibrium, this means the

differentiating Fermi levels is aligned at the interface, hence bending the valence band, E_v, and conduction band, E_c, as shown in Figure 2.6. From the figure one can see how V_0 relates to the potential difference between the E_{cp} and E_{cn} through the difference in the Fermi level energies of the different sides of the junction. This is described by the following expression;

$$qV_0 = E_{Vp} - E_{Vn}, \tag{5}$$

where E_{Vp} and E_{Vn} is the valence band energy for the p- and n-side, respectively.

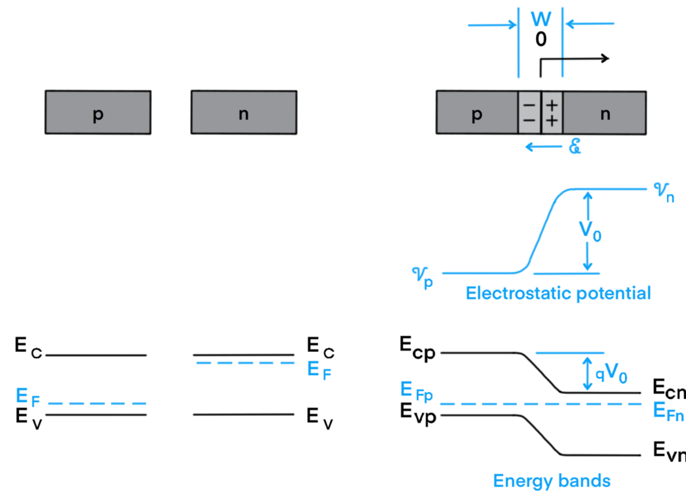

Figure 2.6: Illustration of how the energy bands react to the formation of a pn-junction, (a) prior to and (b) after formation. The figure is inspired by Figure 5-11 in *[8, p. 196]*.

The contact potential can also be related to the width of the depletion region through equation (6),

$$V_0 = \frac{1}{2}\frac{q}{\epsilon} N_d x_{n0} W \tag{6}$$

where W is the depletion region width. An important note is that $N_d x_{n0} = N_a x_{p0}$, which implies that the area beneath the lines on the n and p side in Figure 2.5 (b) must be equal. The equation shows that the contact potential and depletion region width is related to the dopant concentration. By using the fact that X_{n0} can be written as $\frac{WN_a}{N_a+N_d}$ and substituting this into equation (6) we get,

$$W = \left(\frac{2\epsilon V_0}{q} \left(\frac{N_a + N_d}{N_a N_d} \right) \right)^{1/2} \tag{7}$$

describing the width of the depletion region in terms of contact potential and the doping concentrations.

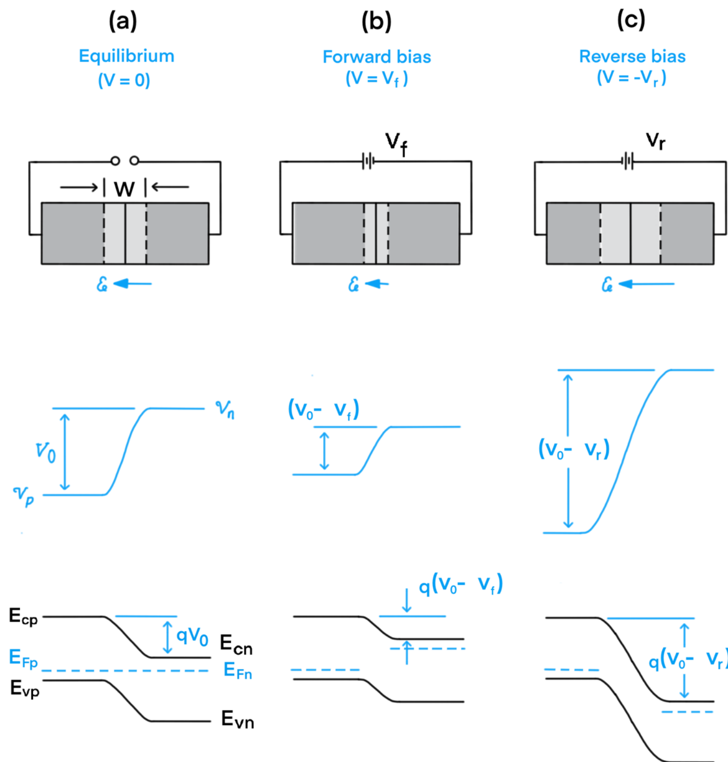

Figure 2.7: Showing a pn-junction under different bias situations. The Potential barrier and depletion region width is affected by the bias. The figure is inspired by Figure 5-13 in *[8, p. 206]***.**

Assuming equilibrium once again, the ions in the depletion region are not mobile, and all the mobile carriers that diffuse into this region are swept across the junction as a result of the electric field discussed earlier. Electrons are swept from the p-side to the n-side, and vice versa for holes. This means that a pn-junction is able to separate the charge carriers that enters the depletion region. This also implies that when applying an outside bias across the junction, it is only possible to transfer current through the junction in one direction, assuming the applied bias in the reverse direction is below the breakdown voltage, so the junction does not break down. This describes the most basic semiconductor component known as the diode. When a forward bias is applied to such a device, the depletion region becomes narrower and the potential difference becomes smaller, hence current can more easily flow through. However, if a reverse bias is applied, the bias is added to the contact potential, consequently, the potential

barrier increases for the charge carriers, so no current can flow. This current-voltage behavior is described mathematically by the diode equation, given by

$$J(V) = J_0\left(e^{\frac{qV}{nkT}} - 1\right), \tag{8}$$

where J_0 is the saturation current density given by the thermal charge generation at $V = 0$, q is the elementary charge, V is the applied voltage, n is an ideality factor, k is Boltzmann's constant and T is the temperature in kelvin. The effect of different bias situations is shown in Figure 2.7. This is the basic operation of a diode, which also describes the rectifying characteristic mentioned earlier in the text.

In order to achieve current transport in any semiconducting material, mobile charge carriers must be generated. However, they must also recombine at specific locations in the device in order to be exploited as current. This will be discussed in the next section.

2.1.3 Generation and recombination

When discussing semiconductor materials from a solar cell perspective, it makes sense to explore what processes takes place when the material is being illuminated. As the sample is illuminated, the photons transfer energy to the electrons in the valence band. If the energy of the photons is larger than the band gap energy of the semiconductor, the electron will be exited across this energy gap and into the conduction band. When this occurs, the thermal equilibrium is pushed towards having more electrons and holes present, than in the equilibrium state. In the excited state, the electron will diffuse randomly until it inevitably recombines with a hole in the valence band. This is known *as band-to-band* or *direct generation/recombination*.

There are different generation and recombination processes, which is highly dependent on the type of semiconductor. First of all, there are two classes of semiconducting material; the *direct bandgap* and the *indirect bandgap* materials. The difference between the two is easiest explained using the illustrative graph in Figure 2.8, which shows the electron momentum space, where the x-axis is the momentum vector, **K**, and the y-axis is energy. The left side represents the direct bandgap material. Here, the top of the valence band is directly beneath the low-point of the conduction band. This means that an electron at the top of the valance band only requires the energy difference of the bandgap to be excited, so a photon-electron interaction is sufficient.

The diagram on the right side shows the indirect bandgap case. Here, the valence band top and conduction band bottom does not match in momentum. This implies that it is not enough to only have a photon-electron interaction to excite the electron; momentum must be transferred to the electron as well. Since a photon practically retain no momentum at all, the electron receives this from quantized crystal lattice vibrational modes known as *phonons*, which are quasiparticles describing these vibrations. All materials with a temperature above 0K have phonons in them and but the energy of these is temperature dependent. In order for an electron to absorb a photon in an indirect bandgap material, a photon-electron-phonon interaction is needed. As the photon must have sufficient energy, the phonon must have the correct momentum. Hence, the absorption in an indirect semiconductor is more temperature dependent than its direct bandgap counterpart, and, as might be expected, the probability of the three-particle interaction is significantly lower than the two-particle interaction [10].

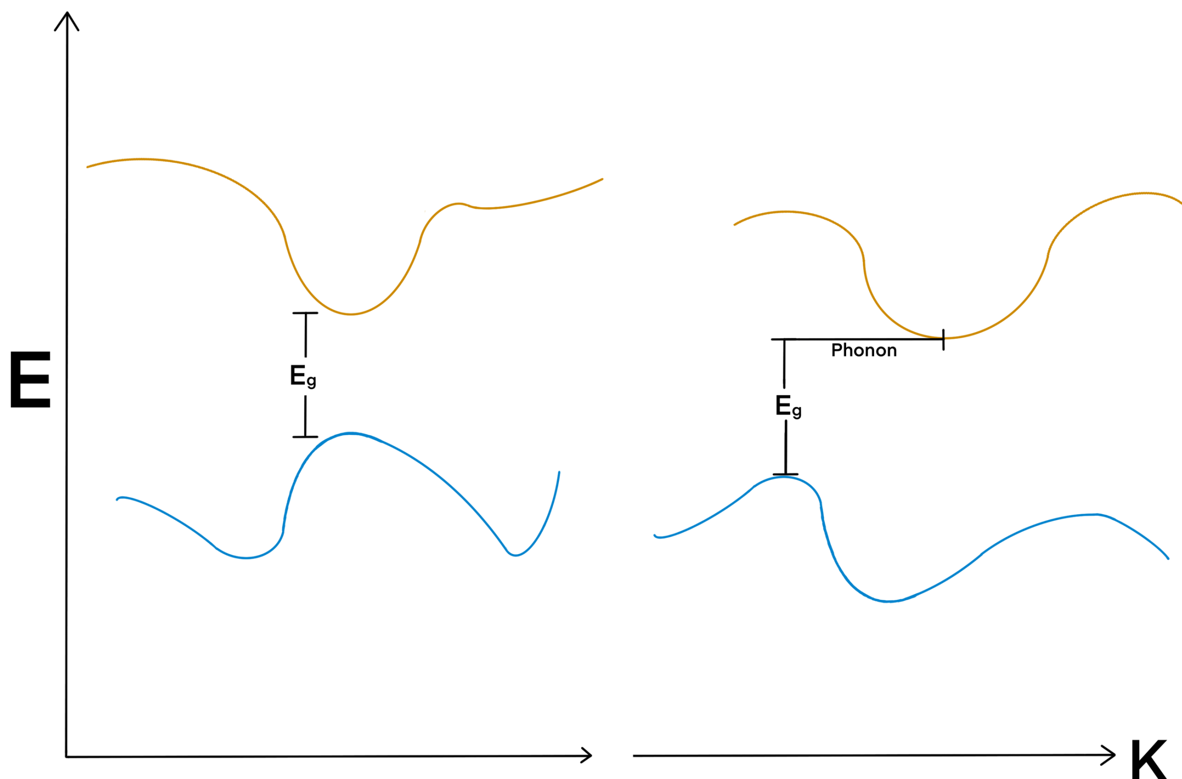

Figure 2.8: Illustration showing the difference in k-space between direct and indirect bandgap materials.

The energy transfer discussed above is called a direct excitation process, or a band-to-band process, being that it does not involve any other aspects than a pure material and a photon. As the equivalent recombination process occurs, a photon and a phonon are emitted if the indirect material. This process is called *radiative recombination*, and the probability of occurrence with regards to material type is the same as for the excitation case. Since an electron

needs to have a hole available in the valence band in order to recombine, the rate at which this occurs is proportional to the concentration of electrons in the conduction band and the concentration of holes in the valence band, and is given in equation (9),

$$R^* = \beta np, \tag{9}$$

where β is the proportionality factor taking material specific characteristics into account. From this we get that if the holes and electrons is separated after excitation, i.e. lowering the concentration of one of the charge carriers say by a pn-junction, the recombination rate will decrease.

Let us shift the perspective a little bit. Consider that the charge carriers move at a certain velocity in the material when they get excited to a higher energy state, and that there is a given time from the generation to the recombination, the different materials can be compared with respect to how far the carriers travel during this period. This time period is known as *charge carrier lifetime* and is denoted τ. As the probability for radiative recombination is high in direct semiconductors, τ is short compared to indirect semiconductors. This means that if the excited charge carriers are to be exploited in direct bandgap materials, the distance from the excitation and the electrode must be very short in order to achieve efficient collection.

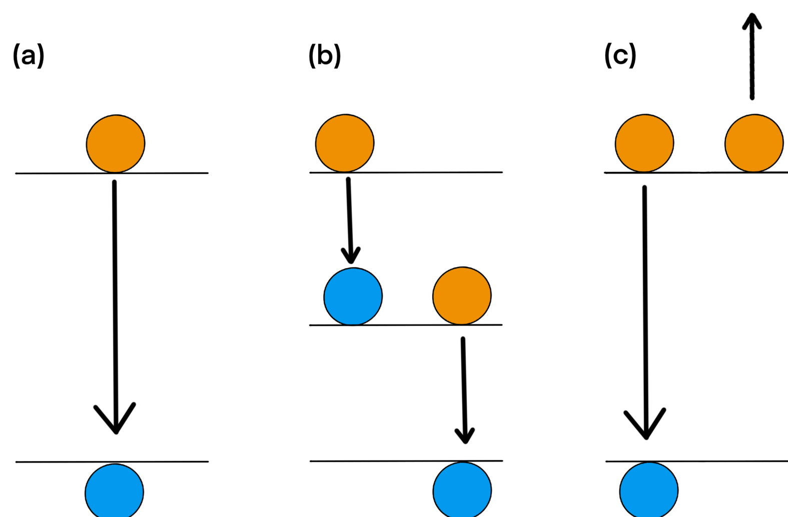

Figure 2.9: Schematic illustration of the different recombination mechanisms occurring in a semiconductor, orange circles serve as electrons, and blue as holes. (a) represents radiative, (b) represents SRH and (c) auger recombination.

Up until now, only band-to-band processes have been discussed. Let consider the other types of generation and recombination processes occurring in semiconductors. The two most important phenomena in an indirect semiconductor is *Shockley-Read-Hall* (SRH) and *Auger recombination*. These are illustrated in Figure 2.9, together with band-to-band recombination, where Figure 2.9 (a) shows the band-to-band, Figure 2.9 (b) shows the SRH and Figure 2.9 (c) is for Auger.

SRH recombination is a process which involves a defect state within the bandgap of the host material [13]. It includes four basic processes, electron capture, electron emission, hole capture and hole emission, depending on the type of doping. The defect state, or trap state, is created by impurities and imperfections in the crystal lattice, which means that it is greatly affected by the production method of the material and sample processing. Peaker et al. reported the effects metallic impurities has on solar cell efficiency, which is attributed to SRH recombination [14]. It was shown that some specific metallic impurities can impact the efficiency of a solar cell greatly, even at parts per billion (ppm) concentration levels. This is because the lifetime of minority carriers is indirectly proportional to the density of trap states described by,

$$\tau_{n,SRH} = \frac{1}{c_n N_T}, \quad \tau_{p,SRH} = \frac{1}{c_p N_T}, \tag{10}$$

where $c_{n/p}$ is the capture coefficients, describing the efficiency of the trap states and N_T is the trap state density [9, pp. 75-76]. Therefore, to obtain a low SRH recombination value, it is very important to use as pure a material as possible. For a c-Si slab with low trap density, typical values of τ can be around 1 ms. For efficient carrier collection in a solar cell, τ should be even higher; up to tens of milliseconds, however, silicon solar cells will work with lifetimes lower than 1 ms as well. Though this type of recombination generally is not radiating in nature, it gives of some surplus energy to the crystal lattice as phonons, i.e. heat.

The last recombination mechanism that will be discussed in this work is Auger recombination. In this mechanism, the energy and momentum are transferred from the recombining charge carrier to another charge carrier of the same type, pushing it deeper into its respective energy band. For electrons, this means that a recombining electron transfers its energy to another electron, which pushes this electron higher up in the conduction band. The excited electron soon transfers the excess energy to phonons, and falls back down to the conduction band edge, producing heat in the material. This process is very dependent upon the

charge carrier density in the material. This is because it is a three-particle interaction (electron-electron-hole), requiring the population of a specific charge carrier type to be so high as to increase the probability of such an interaction to occur.

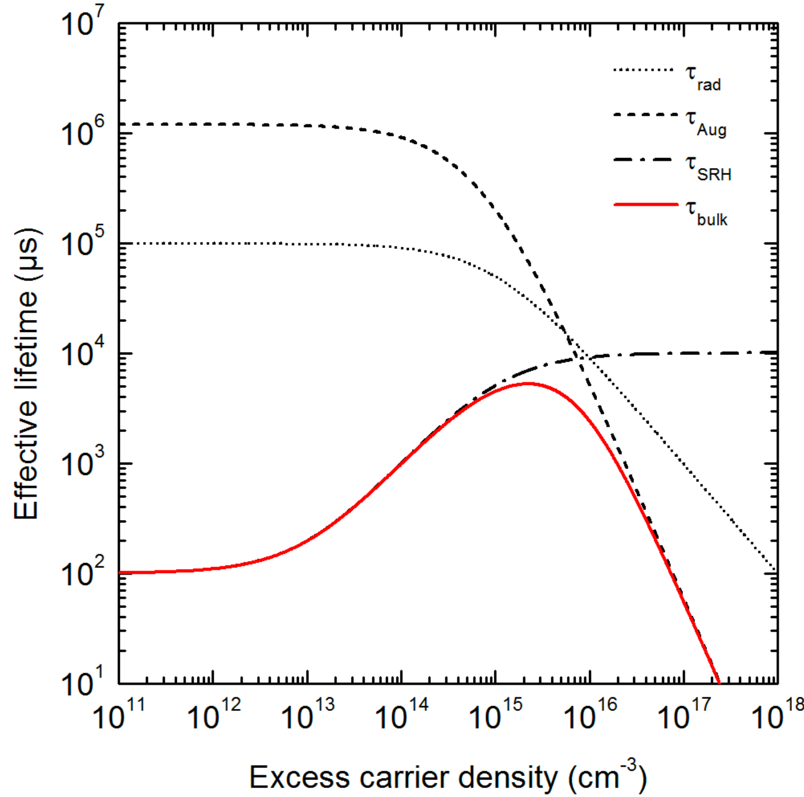

Figure 2.10: This plot shows the relationship between effective lifetime of the charge carriers and the injection level for the bulk recombination mechanisms. The plot is used with permission from H. Haug.

A distribution showing the excess carrier concentration dependent effective bulk lifetime, τ_{bulk}, is depicted in Figure 2.10, where $\tau_{\ bulk}$ is given by

$$\frac{1}{\tau_{bulk}} = \frac{1}{\tau_{Rad}} + \frac{1}{\tau_{SRH}} + \frac{1}{\tau_{Auger}} \tag{11}$$

where τ_{bulk} is given as a sum of the rate of each limiting part. This figure clearly shows that Auger becomes the dominant recombination process for Si as the injection level rises. However, solar cells usually operate at lower injection levels, so SRH is a more important factor. Higher doping leads to a higher degree of Auger recombination. Equation (12) describes the recombination rate of the electron-electron-hole process,

$$R_{eeh} = C_n n^2 p, \tag{12}$$

where C_n is a highly temperature dependent proportionality constant. This means that in highly doped regions at low injection levels, the auger lifetime can be approximated as,

$$\tau_{eeh} = \frac{1}{C_n N_D^2}, \tag{13}$$

implying that the higher the doping, the more prominent it becomes.

So far, all the recombination mechanisms discussed have been bulk processes. However, what happens at the surface must also be considered. At every material surface there will be defects in the form of unsatisfied bonds, which will introduce states within the bandgap and behave like SRH defects. The concentration of SRH defects in the bulk is treated per volume, and the SRH on the surface is treated per area. The biggest difference between bulk SRH and surface SRH is that the defects states on the surface tend to form a continuum of states within the bandgap, rather than just at specific energy levels, as with bulk defects. Unsatisfied bonds are valence electrons from the surface atoms not being able to find any other atoms to form a covalent bond with. When a material becomes thinner, as for instance when making a solar cell, the surface will become a more dominant part of the recombination. This makes sense, since the surface-to-bulk ratio becomes larger, making these effects having a larger impact. The magnitude of surface recombination is given as a surface recombination velocity, S, and is defined as

$$\frac{1}{S} = \frac{\Delta n_s}{U_s}, \tag{14}$$

where Δn_s is the excess carrier concentration at the surface and U_s is the surface recombination rate. S is a very important parameter for describing recombination attributed to surface effects only, and therefore a good parameter to describe the effective lifetime at the surface rather than using the effective lifetime itself. If equation (11) is considered and ad an element for the surface, we get

$$\frac{1}{\tau_{eff}} = \frac{1}{\tau_{Rad}} + \frac{1}{\tau_{SRH}} + \frac{1}{\tau_{Auger}} + \frac{1}{\tau_{Surf}}. \tag{15}$$

If a low value for S is assumed, an expression relating the surface lifetime to S can be introduced as,

$$\frac{1}{\tau_{eff}} = \frac{1}{\tau_{bulk}} + \frac{2S_{eff}}{W}, \quad (16)$$

where W is the thickness of the sample. Here we must also assume that S is equal on each side of the sample, i.e. a symmetrically passivated sample. By implementing equation (16), the thickness of the wafer is considered when describing the lifetime. This is important, since having a thick wafer with high bulk lifetime will show a completely different effective lifetime compared to a thin wafer having a similar bulk lifetime. When the distance traveled by an excited charge carrier, i.e. the diffusion length, in two wafers of with different thickness is similar, the charge carriers in the thin wafer will reach the surface much faster than in the thick wafer, and so contributing to an artificially lower lifetime for the thinner wafer.

2.2 Surface Passivation

There are several ways to counteract the surface recombination mechanisms described earlier, and some of these will be presented here.

The surface of any material typically consists of unsatisfied bonds, also called dangling bonds. For a Si surface the number of surface atoms is 7×10^{14} cm^{-2}, and on a non-passivated surface there have been measurements of 1×10^{13} surface states per cm^2 [15]. These states have to be "switched off" so the electron/hole transport can be efficient, and the recombination losses is at a minimum. This can be done with a variety of approaches, but they are usually divided into two main strategies: chemical passivation and field-effect passivation. In chemical surface passivation the defects are made inactive by introducing an element or a compound which neutralize them electrically. In solar cells this can be done by covering the surface with a dielectric[3]material. By using a dielectric for this purpose, the surface essentially "reflect" charge carriers back into the material by adding a large electrical barrier here. A band diagram showing this can be seen in Figure 2.11. There are dangling bonds on top of the dielectric as well, but because of the energy barrier the charge carriers cannot reach them and recombine.

Thermal SiO_2 has been used by the semiconductor industry for decades which made it a natural candidate for Si solar cell passivation. The early work has been reviewed by Aberle

[3] A dielectric material is another term for an insulating, or poorly conducting material.

et al. in [16] and more recently in [17], to which the interested reader is referred. SiO_2 has achieved very good surface passivation qualities, e.g. Kerr and Cuevas reported S_{eff} values as low as 1.72 cm/s and 7.01 cm/s for 1.5 Ωcm n-type and 1 Ωcm p-type silicon wafers, respectively [18]. This was achieved using a so-called *alnealing* technique, which refers to aluminum annealing processes.

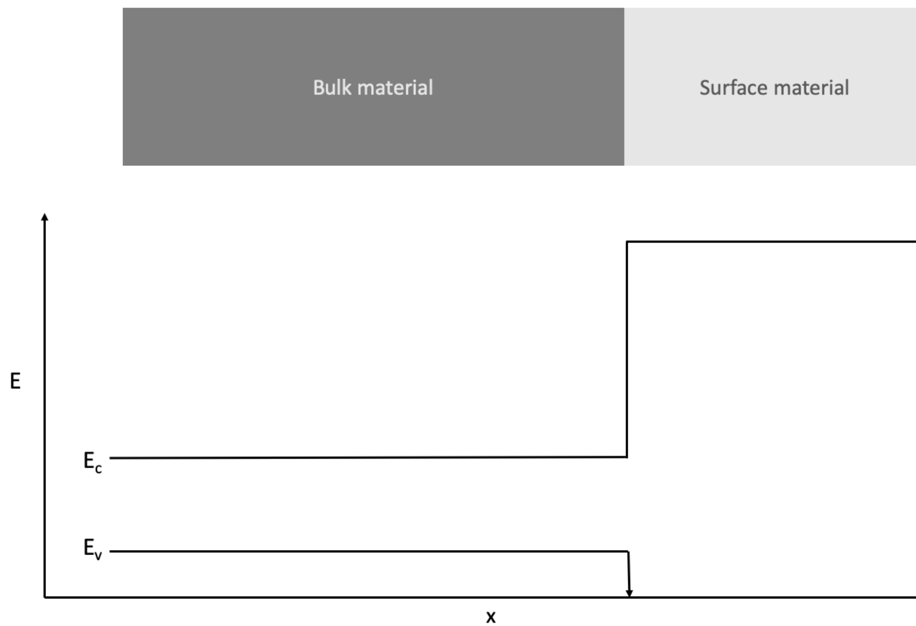

Figure 2.11: Illustration of how the dielectric effects the energy bands near the surface.

The far most common materials for surface passivation of Si is amorphous Si (a-Si:H) and silicon nitride (SiN_x:H, only for p-type Si), where a-Si:H is often used to passivate the surface so bulk lifetime can be measured. Sanyo (Panasonic) implemented an a-Si passivation layer in their Heterojunction with Intrinsic layer (HIT) cell, bringing attention to the a-Si/c-Si interface properties [19]. a-Si is a semiconductor, so a second or even a third material is needed in order to achieve passivation [20]. a-SiN_x:H is used for a variety of different electronic devices; a-SiN_x:H is among the most commonly used passivation materials in the PV industry. Specifically, it is used for passivating n-type emitters. In addition, it has the advantage of having very suitable optical properties, which makes it convenient as an antireflective coating as well [21]. And finally, the technique introduces a substantial amount of hydrogen into the film[4] which diffuses into the bulk, giving some added bulk passivation aspects to the technique [22].

---

[4] Hence the chemical formula a-SiN_x:<u>H</u>.

Note that a-SiN_x:H is used on the front side of the solar cell only, i.e. the side facing the sun. For the backside passivation of a Si solar cell with a p-type absorber, the most common technique, up until recently, was to deposit aluminum as a back electrical contact. Al is a p-type dopant in Si, so by applying this a p-p^+ junction is effectively made close to the rear surface, as Al atoms diffuse into the Si base. The effect of this on the energy bands is depicted in Figure 2.12. The junction acts as a barrier for the electrons, opposing the electrons and not the holes, essentially lowering the concentration of electrons in the vicinity of the back contact. As described in Section 2.1.3, if one of the charge carriers are not present, recombination cannot occur. Hence, the recombination rate at the rear side is lowered due to the lowered probability of a hole meeting an electron. This is an example of a field-effect passivation scheme and is known as aluminum back surface field, Al-BSF. This however, is only one of the possibilities regarding field effect passivation, and we will soon get back a second one [10, pp. 191-193].

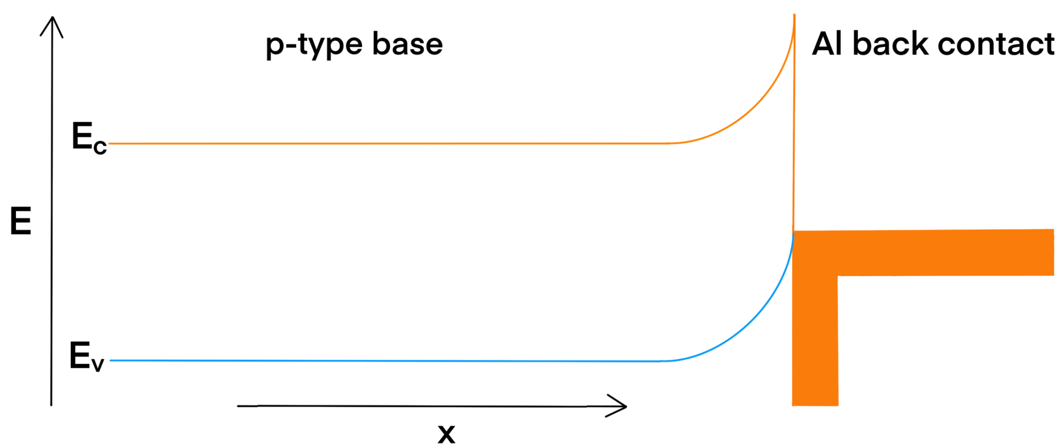

Figure 2.12: The effects of having an Al back contact on a solar cell with a p-type absorber. This results in the field effect passivation and an ohmic contact.

Another approach to surface passivation is to use a combination of both chemical passivation and field-effect passivation. An example of this is the SiO_2/Al_2O_3-stack, where both materials have excellent chemical passivation characteristics on Si, while Al_2O_3 have field-effect abilities as well [23]. By applying two layers of material with different characteristics, a combination of good chemical and field-effect passivation can be achieved. Also, by capping SiO_2 passivation layers with even a thin layer of Al_2O_3 improves the passivation quality, temperature and the long-term stability of the passivation [24], [25]. The HfO_2 have also shown to yield good passivating qualities on both p- and n-type Si [26]. Another approach is to use single layers of Al_2O_3, which will be discussed in the next section.

2.2.1 AlO_x for Surface Passivation

AlO_x as a surface passivation material is one of the mayor breakthroughs within dielectric surface passivation in the last two decades [27]. AlO_x have shown to be highly effective for surface passivation, deposited with a variety of different methods, including deposition techniques like ALD [23], [28], [26], [29], PECVD [30], atmospheric pressure CVD (APCVD) [31] and sputtering [32]. Aluminum oxide has the advantage of having good chemical and field-effect passivation simultaneously. However, this is only true if the aluminum oxide layer is thick enough [33]. If a film deposited using thermal ALD is thinner than 10 nm, the chemical passivation decreases rapidly. The field-effect, on the other hand, remains constant down to a film thickness of 2 nm [34]. The origin of the field-effect passivation characteristics of ALD aluminum oxide stems from fixed negative charges within the film [35]. These charges are located close to the Si/Al_2O_3 interface[5], so it makes sense that they are present even in films as thin as 2 nm. Figure 2.13 illustrates how the charges trigger an accumulation of holes near the Si/Al_2O_3 interface in a p-type material. This comes from an electric field originating from the mentioned charges. From this picture, it becomes clear that the field effect in Al2O3 is a much more suited for p-type material passivation than n-type.

As Figure 2.13 shows, an inversion layer forms inside the Si where the electron and hole concentrations are equal. This leads to a highly recombination active plane beneath the interface. This can, however, be countered by applying a thin layer of HfO_2 between the Si and the Al_2O_3 [26]. Simon et al. showed that even a few cycles of ALD HfO_2 were sufficient to lower the concentration of the fixed negative charges, Q_f, to 0, eliminating the field-effect. Another example on the control of Q_f is to ad ultrathin layers of ALD SiO_2 beneath the Al_2O_3 intentionally, rather than just the expected interface SiO_2 [36]. This research also showed a shift in the polarization of Q_f to positive when thicker SiO_2 layers were introduced. This indicates that it can be used for n-type Si as well, because it then avoids the inversion layer mentioned.

How these effects can contribute to better solar cells and the physics involved in converting solar radiation into electricity is discussed in Section 2.4.

---

[5] There is actually a thin SiO_2 layer at the Si/Al_2O_3 interface as well.

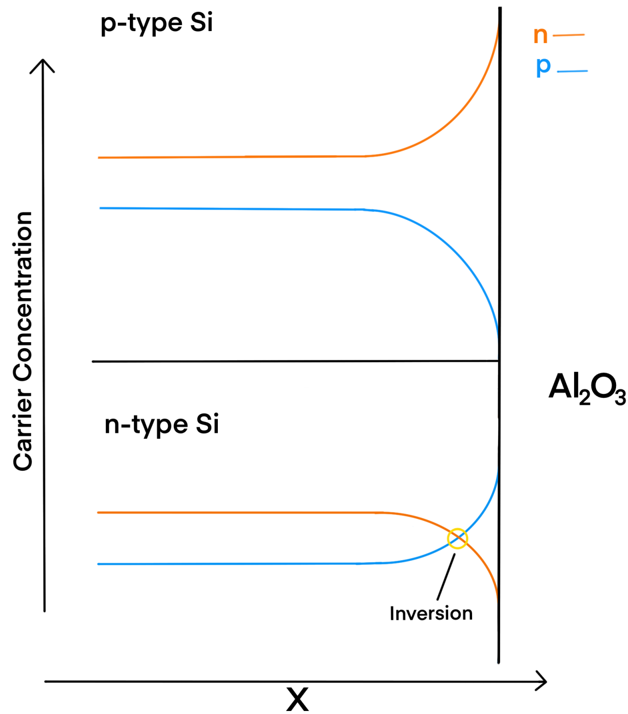

Figure 2.13: This figure shows the effects the negative fixed charges has on the carrier concentrations close to the Si/Al2O3-interface, for both n- and p-type Si.

2.3 Quantum Mechanical Tunneling

Electrons are quantum mechanical particles which can be described by a wavefunction using the Schrödinger equation,

$$i\hbar \frac{d}{dt}|\Psi(\mathrm{t})\rangle = \hat{\mathrm{H}}|\Psi(t)\rangle \tag{17}$$

where $\hbar$ is the reduced Planck's constant, $\hat{\mathrm{H}}$ is the Hamiltonian and $\Psi(t)$ is the state of the quantum system. One of the simplest quantum systems described by this equation is the infinite potential well (or particle-in-a-box), which consist of a potential well with infinite potentials at each side of a given length with zero potential [8, pp. 65-66]. The system with its three first solutions is shown in shown in Figure 2.14. In this system, the particle is trapped inside the potential as the wavefunction is forced to zero where the potential is infinite. This defines the boundary conditions of the problem: Ψ must be zero at the location of the infinite potential. If

the potentials are of finite magnitude and width, these boundary conditions change and Ψ is no longer forced to zero here.

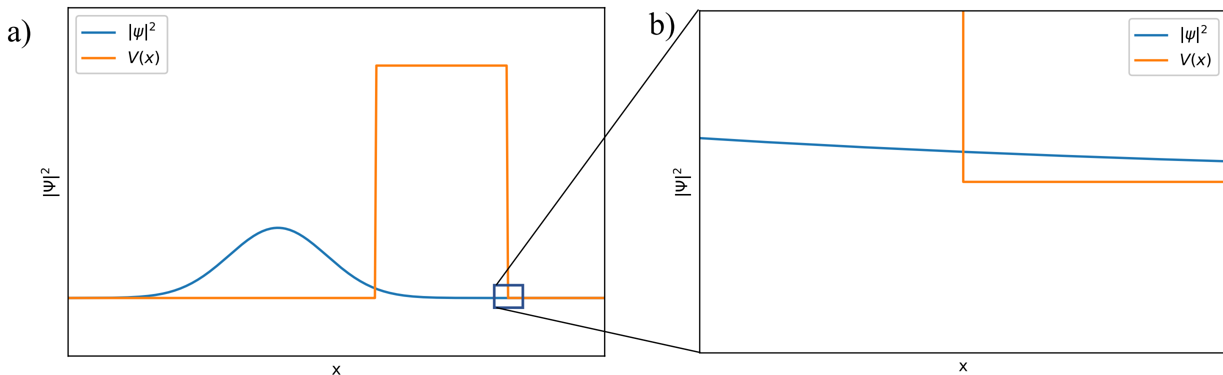

Figure 2.15: a) A solution to the Schrödinger equation with a finite potential barrier, b) showing the lowered wavefunction amplitude on the far side of the barrier, in arbitrary units.

$|\Psi|^2$ is the probability density of the particle, stating the probability of finding the particle at a certain point in space and time. When boundary condition for the finite potential well case is not 0, $|\Psi|^2$ actually penetrates the barrier and, if the width is small enough, there will be some probability of finding the particle on the far side of it. When this occur, it is called quantum mechanical tunneling and have recently been exploited within solar cell technology in the TOPCon cell structure, which will be discussed in Section 2.4.3.3. It is important to note that the potential barrier lowers the amplitude of the wavefunction. This can be seen in Figure 2.15, where b) is a closeup of the indicated area of a). An important point is that the particle does not travel *over* the barrier, but *through* it. Tunneling can also occur across pn-junctions [37].

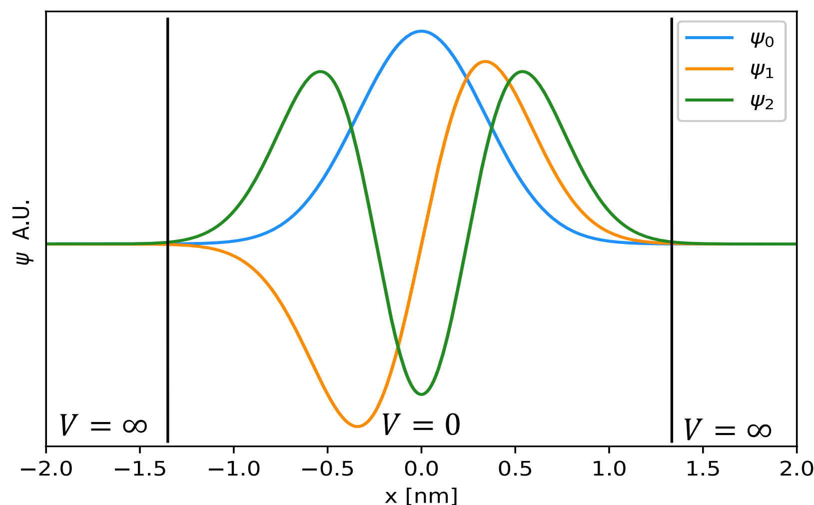

Figure 2.14: The potential well problem with solutions to the three first quantum states.

2.4 The Solar cell

Solar cells are optoelectronic devices which exploit light to generate electricity. An optoelectronic device is a component which utilizes the interaction of photons with semiconductors [8, p. 430]. This field includes optical sensors and detectors, and devices that convert light into current[6], like photodiodes as well as solar cells. This chapter will introduce the physics behind solar cells, what effect passivation have on different solar cells characteristics, and how different passivation schemes used today works.

2.4.1 Basic Solar Cell Physics

Solar energy collection by direct conversion of photons into excited electrons is described by the photovoltaic effect [9, p. 21]. This effect is similar to the photoelectric effect, the difference being that the photoelectric effect describes electrons getting ejected out of the material upon photon-electron interaction, rather than just being in an excited state still incorporated in the energy bands of the material. When a charge carrier has been excited from the valence band up into the conduction band, it may have excess energy compared to the band gap, and excited charge carriers will rapidly move towards the lowest possible energy. This leads to a process called thermalization, which is the process of giving up energy in excess of E_g as heat to the crystal lattice. Thermalization occurs in a matter of 10^{-15}s after the excitation have occurred [10, pp. 41-42]. This process is not to be confused with recombination - it merely “transports” the charge carriers to the conduction and valence band edges. In order to take advantage of the photovoltaic effect to produce power, a solar cell needs the separate the photo-generated electron-hole pairs. This is done by introducing an asymmetrical electrical junction, such as the pn-junction. As was described in Section 2.1.2, after the excitation, the charge carriers diffuse randomly in the material until they either recombine or are swept across a junction. Since the electrons/holes have to randomly walk in the material until they reach a junction, the time they spend doing this needs to be shorter than the τ_{eff}, otherwise the probability of them reaching the junctions before they recombine drops. Usually, there are two junctions in a solar cell; one at the frontside sweeping one charge carrier specie towards the front surface, and one at the backside sweeping the other specie across. Once the carriers have been swept across the

---

[6] And current into light, e.g. Light Emitting Diodes.

junctions, they can be collected by the contacts, but in order to be collected, they must avoid recombination at the surface and at the interface between the semiconductor and contact material.

The contacts for the outside circuit are made of metal which absorbs most of the incoming light hitting it. Hence, the front emitter contacts must cover the smallest area possible (or the emitter can be placed on the back side as well like the IBC cell structure). However, there is a trade-off between covered surface area and collection efficiency. The larger the contact, the better the collection efficiency, but on the other hand, a larger contact means less light absorbed in the semiconductor. Therefore, most solar cells made today have complex schemes to improve both the selectivity and the efficiency of the contacts and have also optimized the contact area.

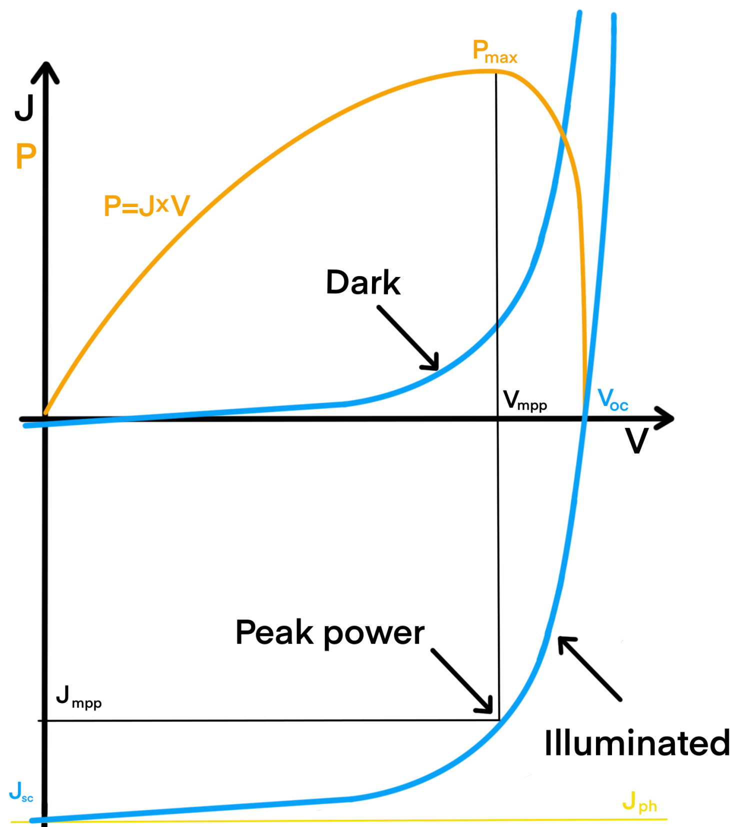

Figure 2.16: IV-characteristic for a solar cell in the dark and under illumination, combined with a plot of the power-curve. Inspired by Figure 8.10 in *[9, p. 98]*. **Here we can see that the peak power occurs when the product between the current density and the voltage is at its maximum point.**

A solar cell is in essence a large area semiconducting diode, which can be described by the diode equation given in equation (8). In Figure 2.16 the current-voltage characteristics of a

solar cell in the dark and under illumination is shown. By considering the behavior, one can see that the difference between the dark and illuminated cell is the same, with an added constant current density. So, by adding this, a new equation describing the solar cell behavior is achieved, like this,

$$J(V) = J_0 \left(e^{\frac{qV}{nkT}} - 1 \right) - J_{ph}, \tag{18}$$

where J_{ph} is the photogenerated current density. The sign is a convention for the direction of the current. There are some additional contributions to the description of a solar cell taking loss mechanisms into account, namely series resistance, R_s, and shunt resistance, R_p. The series resistance is the internal resistance within the solar cell, seen from the outside circuit. This resistance also includes ohmic losses at the contacts. The lower the series resistance, the less it contributes to loss of power output. The shunt resistance on the other hand, refers to a resistance to current transport through the cell, but outside of the junction, meaning this resistance needs to be as large as possible. As the pn-junction on a solar cell is usually formed through some sort of CVD technique, a junction is also formed at the edges of the cell. Current can simply move beside the junctions, and not cross it if they are not cut off electrically. This is done by a laser cutting away the pn junction at the edges, isolating them from the rest of the cell. Anyhow, when these resistances are considered, Equation (18) becomes like this;

$$J(V) = J_0 \left(e^{\frac{qV - JR_s}{nkT}} - 1 \right) + \frac{V - JR_s}{R_p} - J_{ph}. \tag{19}$$

In Figure 2.17, the equivalent circuit of the mathematical descriptions of the current-voltage characteristics discussed so far are shown. Another way of describing a solar cell mathematically is to implement an additional diode to the circuit in Figure 2.17 (b) parallel to the existing diode. By making the first diode ideal, i.e. $n = 1$, and the second diode non-ideal with $n > 1$, one can use this model to investigate an important characteristic of the efficiency of a solar cell, namely the fill factor.

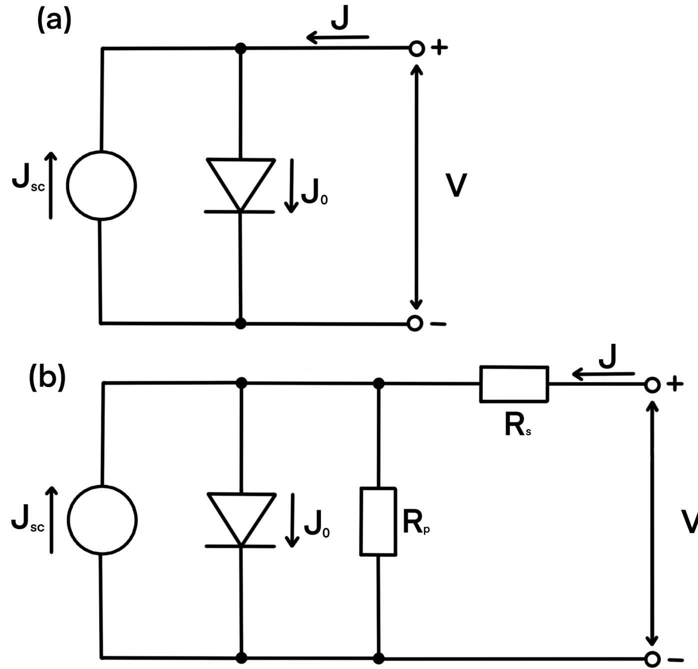

Figure 2.17: Equivalent circuit for (a) Equation (18), an ideal solar cell and (b) Equation (19), an ideal solar cell with resistive loss mechanisms added. Figure inspired by Figure 9.3 in *[9, p. 118]*.

The fill factor, FF, describes the ratio between the maximum power point and the product of V_{oc} and J_{sc};

$$FF = \frac{J_{mpp} V_{mpp}}{J_{sc} V_{oc}}. \tag{20}$$

V_{oc} is the open-circuit voltage of the solar cell, which implies that no current transport occurs. J_{sc} is the short-circuit current density, implying that $V = 0$. All these parameters are impacted by R_s and R_p, although to different degree. R_s affects mostly the FF, but also J_{sc} to some extent. This is because a larger portion of power becomes heat in R_s, making it unavailable for electricity production, which leads to a lower efficiency. R_p, on the other hand, usually only affects FF, but if low it can affect V_{oc} as well. A low R_p leads to more current “avoiding” (shunting) the pn-junction, and therefore lowering the efficiency. Figure 2.18 illustrates this in two plots where in Figure 2.18 (a) R_p is kept constant, and in Figure 2.18 (b) R_s is kept constant. Here, a clear trend towards a much lower FF can be seen as the MPP is changing in both cases.

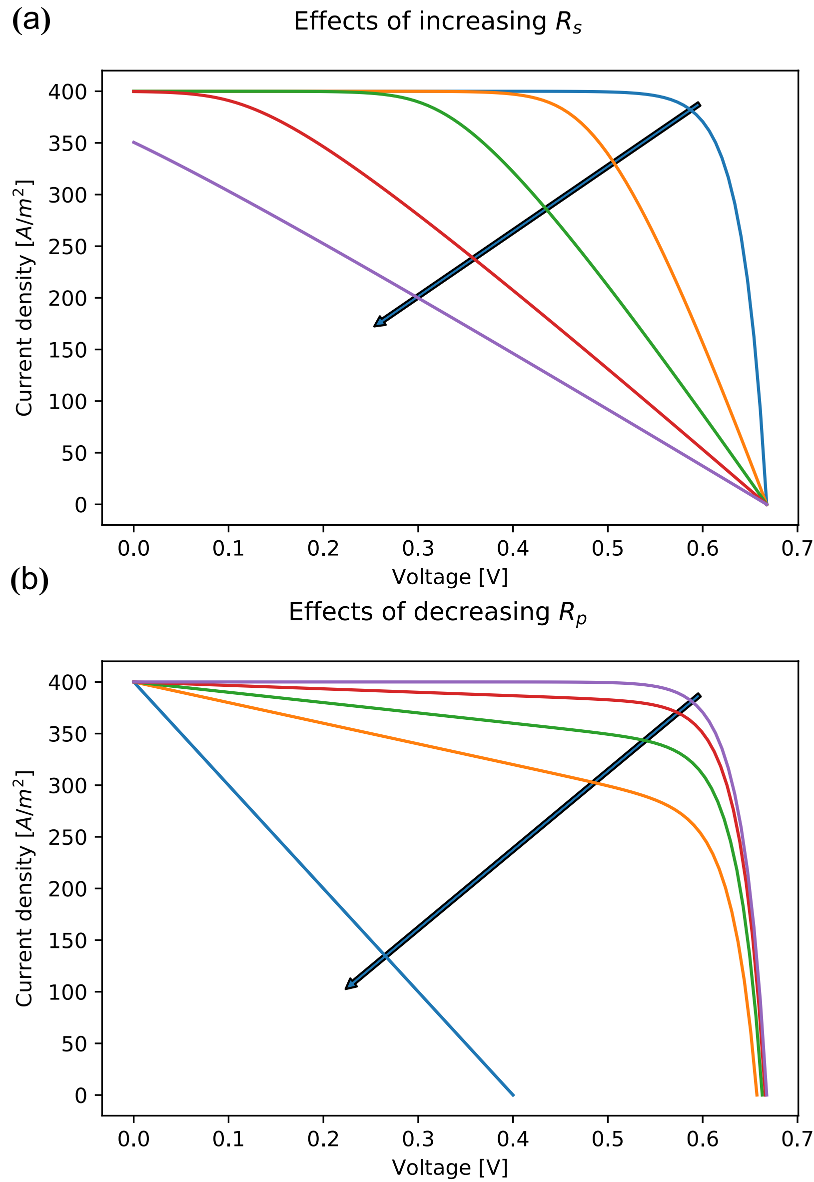

Figure 2.18: Plots showing the effects of (a) an increasing R_s and (b) a decreasing R_p, in accordance with the arrow. The maximum power point is shifted drastically as the resistances are altered, having a large impact on the FF. The purple line in (a) and the blue line in (b) represents extreme cases, where the cell would be defect.

2.4.2 The effects of Surface Passivation

To obtain an understanding of the impact different passivation qualities have on important solar cell parameters, simulations of different SRV's was performed using PC1Dmod6-2, with the resulting IV-characteristic shown in Figure 2.19. The figure shows how V_{oc} is being highly affected as the SRV increases above 10 cm/s, J_{sc} on the other hand, is only marginally influenced by the increased SRV up to 100 cm/s. This can be explained by the bandgap

utilization effect; As the surface recombination increases, the quasi-fermi levels are not able to split as efficiently, hence the bandgap is utilized to a lower degree.

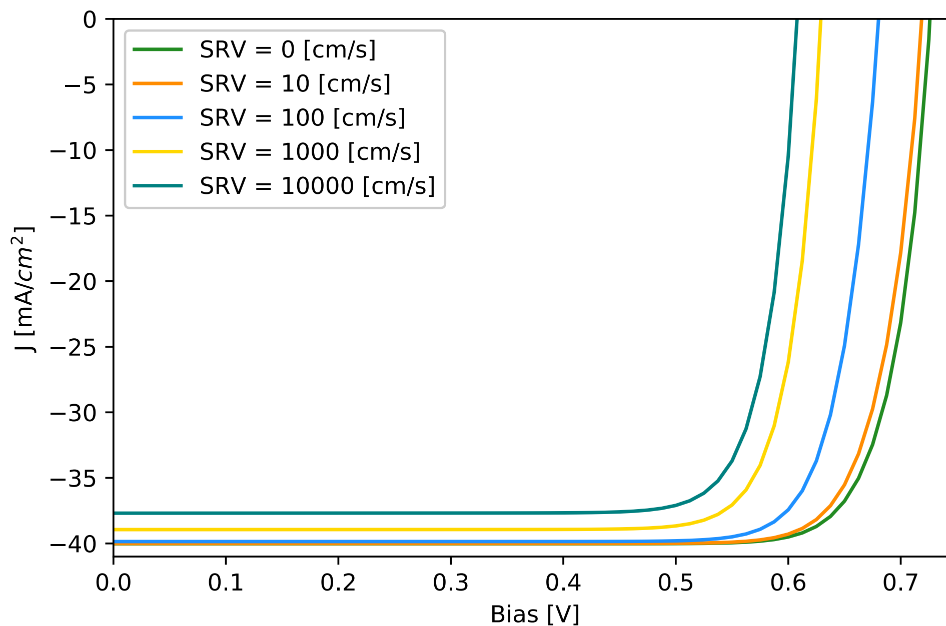

Figure 2.19: Plot of PC1D simulation data from a simple idealized solar cell structure in standard test conditions with varying SRV.

Another insight gained from Figure 2.19 is that as soon as the passivation quality provides SRV's less than 10 cm/s, the decision to decrease this value further has to take the economics into account. Developing new and better passivation processes can be expensive, while the gain in efficiency can be relatively low. On the other hand, if the existing processes can be used for cheaper materials, the impact can be substantial.

2.4.3 Solar Cell Passivation Schemes

As homojunction solar cell technologies and solar cell materials have been improved over the years, the limiting factor for the efficiency have been driven towards surface and interface recombination. Several different schemes to overcome these issues have been proposed, like the Aluminum Back Surface Field (Al-BSF) cell, the Passivated Emitter and Rear Cell (PERC) and recently the Tunnel Oxide Passivated Contacts (TOPCon) cells. These concepts have all different surface passivation schemes, which can utilize a range of materials, uncluding AlO_x. These technologies will be described in the following sections. Finally, a brief introduction to heterojunciton solar cells will be given.

2.4.3.1 The Al-BSF Cell

Up until recently, the Al-BFS cell have been the industry standard because of its simple and cost-effective production methods, yet relatively high performance. An illustration of the Al-BSF cell is provided in Figure 2.20. In this figure one can see the front contacts, most commonly silver, and the anti-reflective coating (ARC). This ARC-layer usually consists of SiN_X:H, which as discussed contributes to bulk passivation as well. As light travels in air and hits the solar cell, some portion of the light will be absorbed, and some portion will be reflected. This is determined by the angle of the incident light and the difference in refractive index of air and the material. Refractive index is the relation between light speed in vacuum and light speed in the material – decreasing speed of light leads to an increasing refractive index, and the larger the difference between refractive indexes of the material, leads to higher reflection. One approach to improve the absorption is to add an interlayer with an intermediate refractive index compared to the other two materials. SiN_x:H have a refractive index around 2 (varying with wavelength) which is a good match for air and Si, as they have values of 1 and 4.3, respectively. Since the difference between the refractive indexes of air and SiN_x:H is lower, the reflection decreases, and as more light is absorbed the overall efficiency increases.

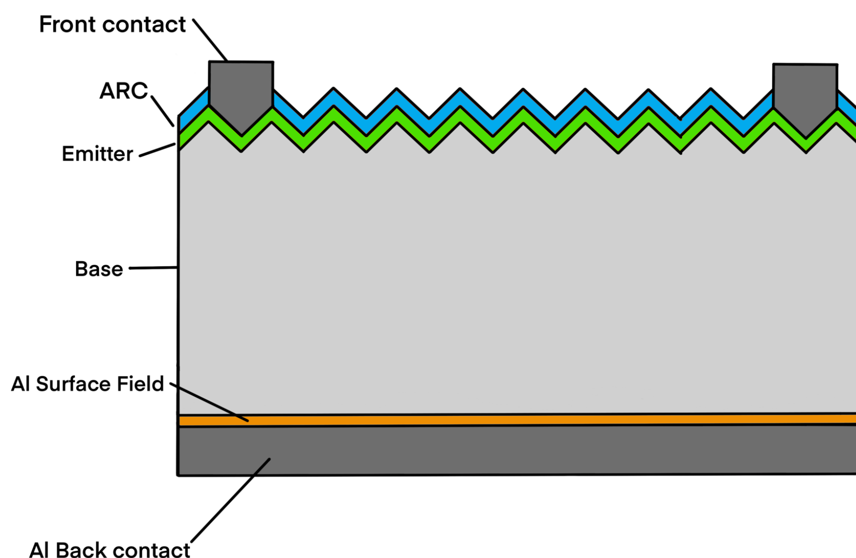

Figure 2.20: Schematic illustration of the Al-BSF cell structure.

Figure 2.20 shows the emitter and base, as well as the back-contact structure. The back contact covers the entire back surface of the cell structure, with the contact material being aluminum. When the contact firing is performed, some the aluminum diffuses into Si and dopes

a thin layer of the silico. The technology utilizes that aluminum is p-type dopant in Si, which makes this thin layer heavily p-type doped, forming an electric field between this heavily doped region and the less doped bulk substrate. This field opposes the minority carriers, lowering the concentration of that particular charge carrier specie, which ultimately lowers recombination at the back contact and enhancing the efficiency of the solar cell.

2.4.3.2 The PERC Cell

In later years, the solar cell manufacturers have started an industry wide change from Al-BSF cells to PERC cells [2]. This is achieved by introducing two additional deposition steps and a laser process step into the production pipeline. This scheme has both front and rear side passivation, and local contacts on the rear side. The backside passivation layer, in combination with the local contacts, lower the back-surface recombination velocity considerably, relative to the previous discussed Al-BSF cell [38], [39]. This can be understood by assuming that the recombination per area at any contact is equal. If the contact area is smaller, as it is in PERCs, the total recombination occurring at the contact will be lower. It is, however, a tradeoff between

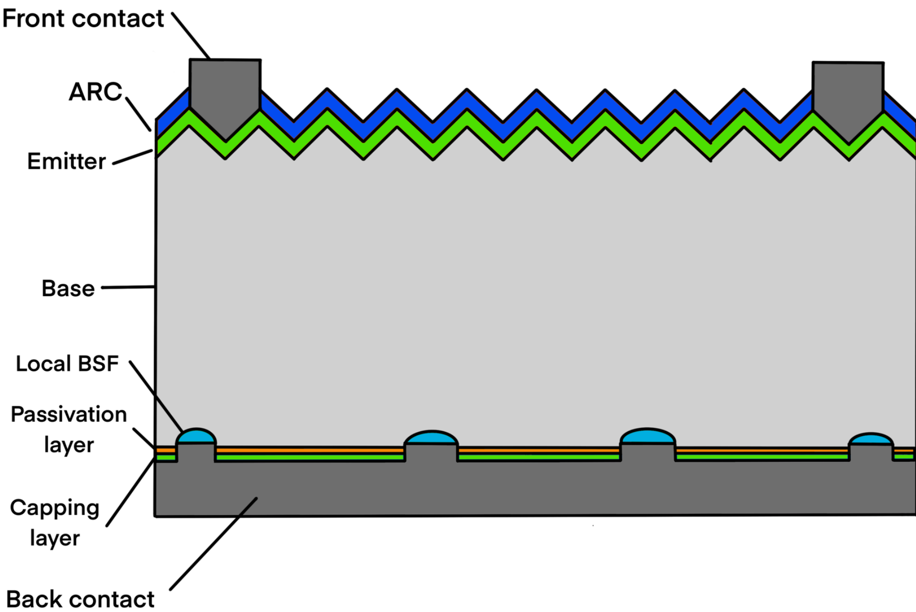

Figure 2.21: Schematic illustration of the PERC solar cell structure.

contact size and spacing between them, and the efficiency of current collection. An illustration of the PERC scheme is shown in Figure 2.21. The frontside structure of the PERC is identical

to the AL-BSF front side, it is the backside that differentiate them – the PERC has local contacts with field-effect passivation, and surface passivation in between the contacts. This lowers the contact area considerably, leading to less contact recombination. The backside surface passivation normally consists of a passivation layer of SiO_2 or AlO_x and a SiN_x:H-capping layer. The negative fixed charges in the AlO_x passivation layer provides an effective field effect passivation by creating an accumulation region in the p-type silicon base close to the rear surface.

2.4.3.3 The TOPCon Cell

Both of the previous approaches are commonly using a p-type Si base as standard. P-type Si has dominated the marked for many years, as it has advantage having longer minority carrier lifetime as well as of being simple to produce and easily doped. On the other hand, the p-type Si degrades over time as boron-oxygen complexes are formed during illumination, reducing the charge carrier lifetime in the material [40]. Recent years n-type Si is becoming more and more relevant as it does not have these issues but have some difficulties with regards to material production [41]. The TOPCon structure is based on n-type base, shown in Figure 2.22, which includes a passivation layer, or a passivation layer stack, on the front side, and a dielectric/p-type silicon stack on the backside. The dielectric layer is ultrathin, about 1.4 nm [42], which allows charge carriers to efficiently tunnel across it into the p-type Si and is then transported to the back contact. The efficiency of the tunneling decreases if the oxide is thicker, and the maximum tolerable oxide thickness is 2.0 nm, which when exceeded decreases the FF [43]. The

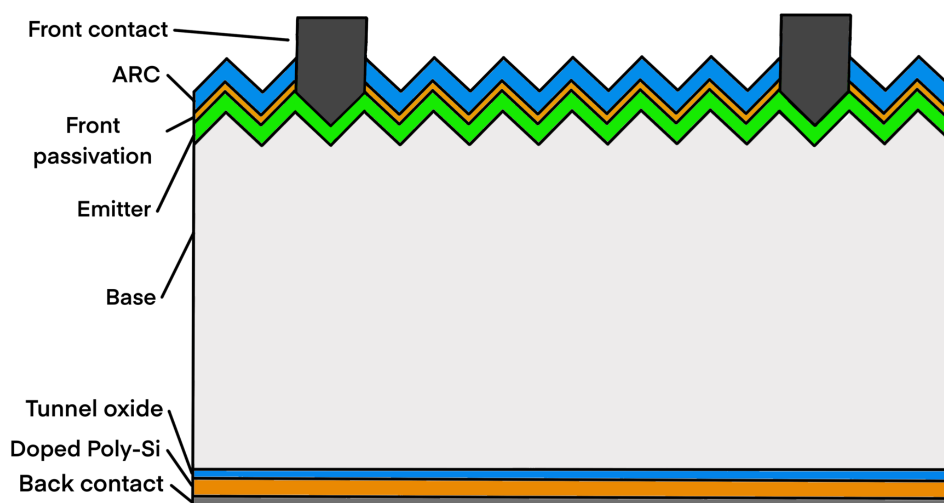

Figure 2.22: Schematic illustration of the TOPCon solar cell structure.

tunnel oxide layer, normally a thin, thermally grown layer of SiO_2, but can also by ALD grown AlO_x because of its high degree of field effect and chemical passivation, and the thickness control provided by the ALD method, which will be described later in this thesis.

2.4.3.4 Heterojunction Solar Cells

A homojunction solar cell utilize doping to create the pn-junction used to separate the charge carrier species. This is often a high temperature process requiring a high energy input into making the cell [44]. A way of avoiding this is to make a heterojunction solar cell, which instead uses two different materials with different transport mechanisms to create the pn-junction [45]. The most common example of this is the cell structured formed by adding a doped layer of amorphous silicon (a-Si:H) on the Si wafer to form the junction (often called SHJ or HIT cells). Another, more recent example of this is the hybrid inorganic-organic PEDOT:PSS / Si solar cell structure, illustrated in Figure 2.23, which utilizes a n-type Si absorber with a PEDOT:PSS layer forming the p-type emitter [46]. By combining PEDOT:PSS directly on the Si surface, a highly recombination active interface is made [47]. This is counteracted by using a thin oxide at the interface between the two [48]. Different materials have been used as interface passivation, among them is SiO_x and AlO_x [49]. The cell structure allows for a cheap, low process damage, low temperature fabrication process [50], however, with limited efficiencies reported compared to the conventional cell structures [46].

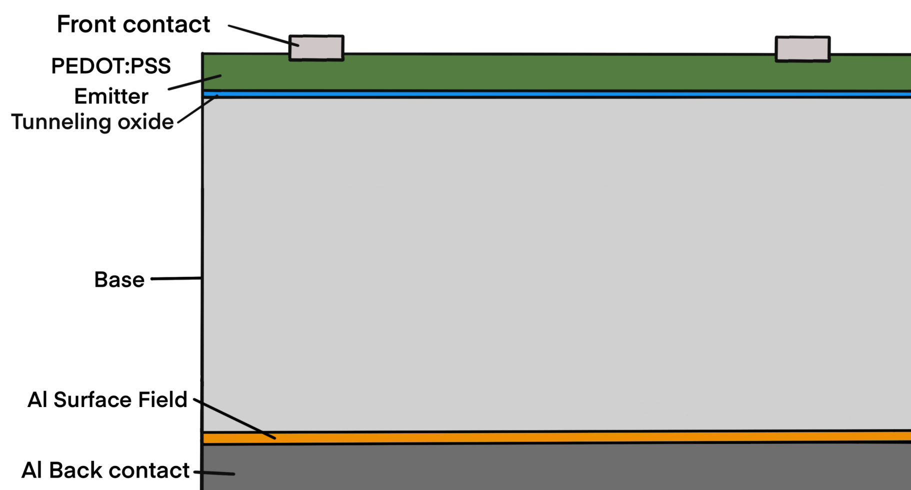

Figure 2.23: Illustration of the PEDOT:PSS / Si solar cell structure.

3 Experimental Methods

All experimental techniques used in this work, as well as detailed descriptions of the processing methods will be presented in this chapter. All relevant process parameters will also be presented. The sample cleaning, AlO_x film deposition and thickness measurements where performed at the MiNaLab at UiO, and the rest of the procedures where conducted at the IFE Sol laboratory. The chapter is divided into two main subchapters; one which handles the way samples are processed with regards to cleaning, film depositions and successive treatments, and one which describes the different measurement techniques used to acquire the data presented in this work.

3.1 Atomic Layer Deposition

There are many techniques to deposit Al_2O_3 films, such as APCVD, PECVD, sputtering and more, however, none of these have the same thickness and coverage control as ALD. Due to its dependence on surface saturation limiting the thickness rather than chemical reactions (as for CVD), it has atomic thickness control [51]. Another important factor is that ALD reacts on all surfaces regardless of their topography and can coat uniformly even on high aspect-ratio structures. Because of this, it is used for many different applications within the electronics industry, e.g. dynamic random-access memory (DRAM), metal-oxide-semiconductor field-effect transistor (MOSFET), electroluminescent display technology, solar energy and many more within the nanotechnology field [52]. During the last 15 years ALD has received increasing attention within the PV community as a technology with great potential for surface passivation layers [35]. Even though ALD is a large topic, a general introduction with the most relevant ALD theory will be given in this section, with the process example of thermal AlO_x in focus.

3.1.1 Process Description

ALD is a subclass of the CVD method where two or more reactant gases are brought into a chamber in gas phase where which they react with each other on a hot substrate surface. CVD differs from physical vapor deposition (PVD) techniques in that it utilizes chemical reactions to deposit the desired materials on the sample, rather than use physical forces like

electromagnetic fields, evaporation or ion radiation to release material from a target, which then deposits onto the sample surface by condensation. Examples of PVD are sputtering, thermal evaporation and electron-beam evaporation. In CVD it is important to control the parameters for pressure and temperature in order to avoid *homogeneous* reactions, i.e. gas phase reactions above the sample surface. If this is not executed correctly, it will push the chemical equilibrium towards particle formation “mid-air”, which will then accumulate onto the surface, leading to poor film quality [53, pp. 374-376]. A basic CVD reaction chamber, which is very similar to an ALD reaction chamber, is depicted in Figure 3.1.

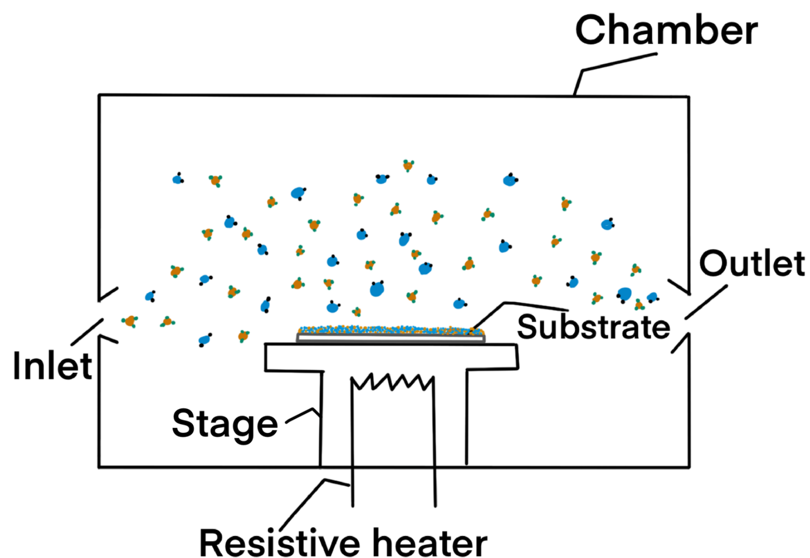

Figure 3.1: Simple illustration of a CVD reaction chamber. The two precursors are let simultaneously into the chamber. For an extended period of time.

CVD is in general a continuous process that introduces two or more precursors into the reaction chamber simultaneously. ALD, on the other hand, is a step-by-step cyclic process, relying on *surface saturation* and temporal or spatial separation of reactants. This enables the use of highly reactive precursors otherwise difficult to use controllably, giving the opportunity for low temperature deposition [54]. Process temperature naturally vary between the different processes and can range from room temperature up to several hundred degrees C. The separation of the precursors is usually achieved by separating them in time. A schematic representation of an ALD cycle is illustrated in Figure 3.2, using the TMA/H_2O process as an example. First (top panel of Figure 3.2), the sample is OH-terminated. This is typical for a Si surface pre-treated with an HF-dip and just kept in ambient atmosphere for about one minute before being put in vacuum. Going clock-wise in the figure, TMA-vapor is introduced into the chamber. This reacts with every available surface, where a chemical bond forms between the

aluminium in TMA and oxygen in the film. In this reaction, methane is also formed as a by-product, which is purged from the chamber with the hydrogen in the OH-groups, forming bonds with the surface. The chemistry of this half-reaction is described by,

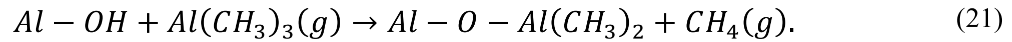

$$Al - OH + Al(CH_3)_3(g) \rightarrow Al - O - Al(CH_3)_2 + CH_4(g). \tag{21}$$

As the surfaces saturates, chemical reactions cease, and any further TMA exposure will not change the surface. Excess TMA is purged out of the chamber with nitrogen gas, and the first half-reaction is complete. The surfaces are now terminated with methyl-groups, as shown in the bottom frame of Figure 3.2. The second reactant is now introduced into the chamber, namely water vapor. The water vapor reacts with the surface methyl-groups, forming more methane and OH-terminated surfaces. As this reaction finishes, the second half-reaction is complete., and the chemistry is as follows:

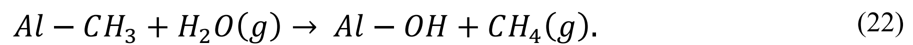

$$Al - CH_3 + H_2O(g) \rightarrow Al - OH + CH_4(g). \tag{22}$$

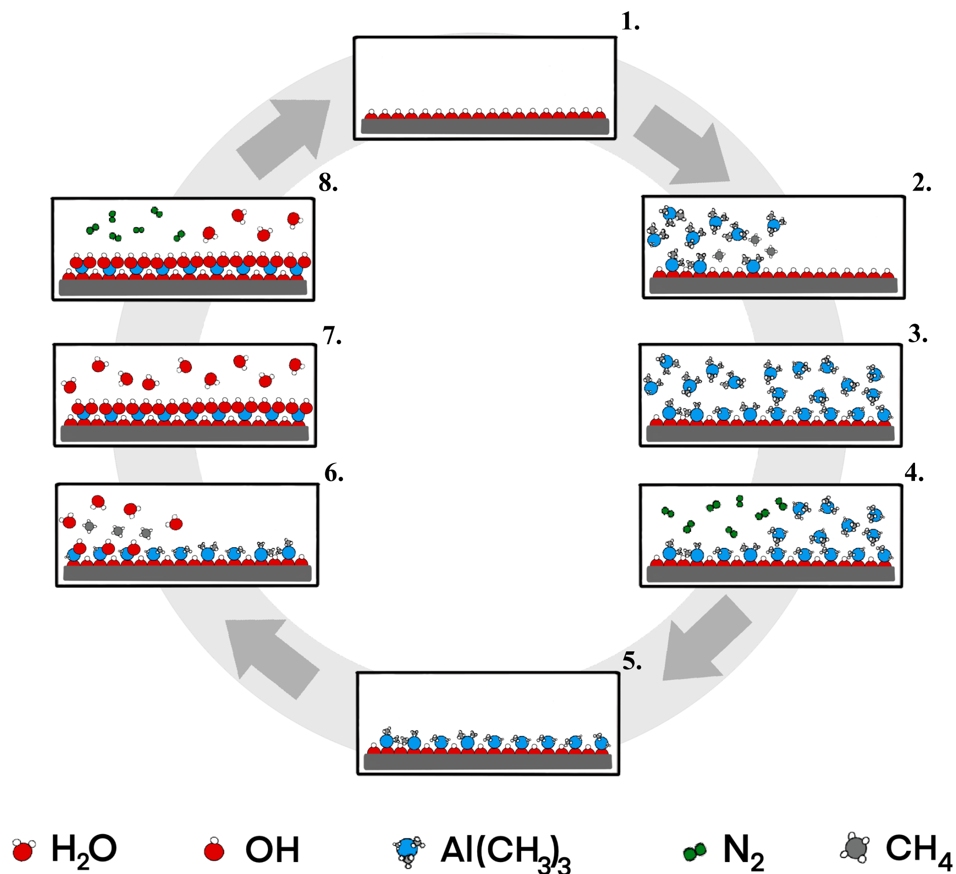

Figure 3.2: A schematic illustration of the $AlMe_3/H_2O$ process cycle on an OH-terminated surface. Figure inspired by Vee's figure in *[62]*, Fig. 2.

Any excess water vapor and methane is purged, again with nitrogen. This describes one cycle of the process, and this is repeated until the desired film thickness is achieved. There is an alternative to the cyclic, inert gas purging where which the inert gas is continuously flowing through the chamber. This purges all the same species at the same stage in the cycle, but the flow also contributes to the transport of the precursor species. This reactor variation is called a continuous-flow reactor, which is the most common type used today, and is also the type of reactor used for in this work.

The illustration in the previous section of the ALD cycle is simplified. For a more accurate account, one must assume that one cycle ads exactly one monolayer of material to the surface. This is in fact not the case for every material. The cation precursors often consist of a metal atom bonded to some sort of hydrocarbon chain. These chains can be large, which cause the molecules bonded to the surface atom to block off the neighbouring atoms to other precursor molecules, hindering them from creating bonds. This is called the *steric hinderance effect,* and it contributes to a lower growth per cycle (GPC) than what a complete monolayer would produce. Consider AlO_x as an example. First, this material grows amorphous within the ALD window, meaning it has no symmetry or repeating structure, rendering what is known about the unit cell of Al_2O_3 irrelevant. If one look at the sizes of Al and O, which are ~0.5 – 0.6 Å and ~1.2 – 1.3 Å, respectively, and assume a semi-close packed structure, the growth rate should be close to ~1.7 – 1.9 Å [55]. This, however is not the case, as the GPC have been reported to be about 0.9 Å [56], [57].

As mentioned, ALD can operate at a large range of temperatures. However, it is important to stay within the ALD-window in order to attain the advantages of the technique. To stay within this window, the temperature should be high enough to drive the reactions forward, but so low that the temperature doesn't exceed the ALD window. At too high temperatures, the precursors can start to decompose, and the already adsorbed species can desorb from the surface or the precursors can react with their own respective surface species. All of these events are unwanted and will contribute to a less controlled process and a lower quality film. Since ALD is relying on the complete separation of precursor and oxidizer for thickness control, uniformity and film composition, which is less temperature dependent, establishing the appropriate deposition temperature is very important for reproducibility and GPC stability.

To ensure precursor separation, the purging times between each step are also very important. They vary substantially between different types of reactors and reaction chamber

sizes, but also between deposition temperatures and reactants. Precursor pulsing times also vary with the same criterions as the purging times. At higher temperatures, the precursors are more reactive, which enables them to saturate the surface in a shorter period of time compared to lower deposition temperatures. Some reactants tend to stick to surfaces in the chamber without undergoing chemical reactions. Water is a good example of this, especially at low temperatures This effect can require a significantly prolonged purging step in order to get the concentration of water vapor in the chamber down. As will be shown later in this thesis, if purging times are not adjusted in relation to any deposition temperature adjustments or chamber alterations, one could get undesired CVD growth instead of pure ALD.

3.1.2 Advantages and Shortcomings

There are many advantages regarding the use of ALD as a deposition technique. It has high thickness precision, high uniformity, it can use low deposition temperatures, it requires only low vacuum and it can deposit material on high aspect ratio structures.

The thickness precision originates from the use of step-by-step, saturating, irreversible chemical reactions being the controlling factor of the thickness, adding layer by layer of atoms. Rather than a continues flow of gases reacting with the surface over a given time (which also can provide good control), as in CVD, it is the number of cycles that determines the thickness in ALD. This is very advantageous when depositing materials for tunnelling oxides that must be less than 2 nm thick.

By utilizing a self-saturating chemical surface reaction, one essentially allows the reactants to bond with all available atoms on the surface. This naturally gives very uniform films over large areas.

The low temperature aspect of ALD gives the opportunity to use heat sensitive substrates like polymers. ALD is generally a “soft” deposition technique compared to other techniques, and especially the physical ones. On the other hand, the method has very low deposition rates compared to other methods. This in turn makes it tedious for deposition of thicker films, and also rises issues within high through-put industries, like the solar cell industry [58]. This is solved by running batch processes of several hundred wafers simultaneously in a single ALD reactor. In a 2019 interview with PV magazine, the CTO of Leadmicro reports that they now load 800 wafers at a time [59].

3.2 Sample Processing

This section will introduce the reader to specific process parameters used during sample processing.

3.2.1 Sample cleaning

To achieve a high-quality surface passivation, with a repeatable process, it is necessary to have exceptional control over the surface prior to passivation layer deposition. As Si wafers are delivered from the vendors, they have a "native oxide" on the surface. This SiO_2-layer starts growing immediately after a wafer has been cut and is exposed to air [60]. The growth of such a layer saturates at a thickness of several Å [61]. By applying a HF etch, the native oxide is removed, and the surface is now hydrogen-terminated Si, which is an excellent starting point for further processing. The initial samples in this work were treated in accordance with the initial process in Table 1, and the later samples were treated as described in the later process in the table, the reason for the changes being alterations in the HSE regulations.

Table 1: Table showing the process parameters for SiO_2-layer removal for the experiments in this work.

Initial Process	Chemical	Time/temperature
HF-dip	5% HF	1min
Post HF-dip rinse	DI-water	5 min
Later Process		
HF-dip	HF, 2%	3 min, RT
Post HF-dip rinse	DI-water	3 min, RT

3.2.2 Thermal Atomic Layer Deposition

The deposition of thin film surface passivation is performed using thermal ALD, with the continuous flow reactor Beneq Thin Film System-200 (TFS-200) located at the MiNaLab facility at UiO. Since the technique is described in general in Section 3.1, this section will present the process flow and parameters utilized during experiments.

The thermal ALD AlO_x process using TMA and water is one of the most established ALD processes in the field and is close to an ideal ALD process. However, even though ALD is wide spread and extensively used, the reproducibility and results can vary between ALD reactors and labs [62]. Therefore, it was important to establish a recipe specifically for surface passivation for the reactor in MiNaLab. The standard process parameters used to deposit AlO_x prior to this work can be seen in Table 2, and was the basis for the depositions. The optimized process for this system will be presented later in this work.

Table 2: Process parameters for the already established thermal Al_2O_3 deposition process with a deposition temperature of 200°C. The reactor pressure for all depositions vary between 1.8 mBar - 2.0 mBar. 1000 cycles give approximately 132 nm of deposited film.

Process	Chemical	Pulsing Time
1st half-cycle	TMA	400 ms
2nd half-cycle	H_2O	500 ms
In-between purge	N_2	2 s

The TFS-200 is divided into two parts; the larger outer chamber and the inner reaction chamber. The outer chamber contains heating elements, the gas distribution unit (GDU) and various access point for temperature sensors and gas lines going into the GDU. The inner chamber is placed inside the outer one, centered, on top of the GDU and the exhaust line, as the illustration in Figure 3.3 shows. This inner chamber is where the samples are placed for deposition and is also referred to as the reaction chamber. It consists mainly of the sample stage but also has the gas distribution ring, which helps spread the precursors evenly throughout the chamber. The stage has room for approximately 1 cm tall samples, so the volume of inner chamber is relatively small. This small volume allows for short cycle times; about 5 s per cycle for the TMA H_2O process at 200°C.

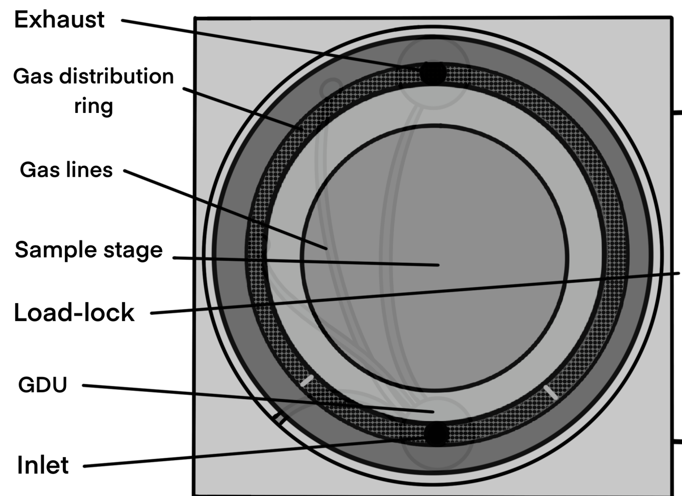

Figure 3.3: Illustration of the chamber layout of the TFS-200. The gas lines are beneath the reaction chamber.

When a process is run, the reactor is pre-heated to the desired temperature, it is then ventilated to atmospheric pressure. The sample is placed on the stage, usually on a clean dummy wafer. Next the reactor is closed and pumped down to a few millibars. The system is pumped down through the exhaust which is connected to the inner chamber. However, there is only a partial seal between the inner and outer chamber, resulting in a lower pressure in the inner chamber. This is to avoid precursors leaking outside the reaction chamber, which would result in an undesirable film deposition there. The sample is now placed inside the reactor, and as the temperature and pressure reach their set value, the deposition process can begin. The ALD process and the chemistry were explained in Section 3.1.1. After the deposition, the system is vented, and the sample is ready for further processing.

3.2.3 Annealing

In order to activate the full passivation potential of the thin film, it is necessary to perform an annealing process [23], [28], [63]. This was performed in a belt furnace used for contact firing in ambient atmosphere. Although a lot of research have been performed on the effects of different annealing atmospheres, such as N_2, O_2 and H_2 [28], [64], [65], (with differences in lifetime almost as large as one order of magnitude for ambient atmosphere and pure O_2 atmosphere. Pure O_2 being higher) this work wanted to see the potential of the simplest solutions.

3.2.4 Metallization

To electrically characterize the samples, some form of contacts needs to be applied. This was performed in a thermal evaporator, the Kurt J. Lesker Company 36 thermal evaporation system installed at IFE. Generally, thermal evaporation is a deposition technique which utilizes an electrically resistive crucible or "boat" filled with a desired amount of a highly purified metal. A high current is then run through it, heating it up to high temperatures. The metal eventually melts and starts to gradually evaporate, leading to a metal vapor throughout the chamber, depositing on every available surface within the chamber within the line-of-sight of the crucible. That is why the substrate is placed directly above the evaporating target material, as Figure 3.4 shows. Since this is performed in a vacuum chamber, the metal atoms have a long mean free path. The mean free path of an atom is the average distance an atom can travel without colliding with another atom. To improve the film quality further, with regards to uniformity, one can rotate the substrate holder. By doing this, the atoms hitting the sample are more evenly spread across its surface.

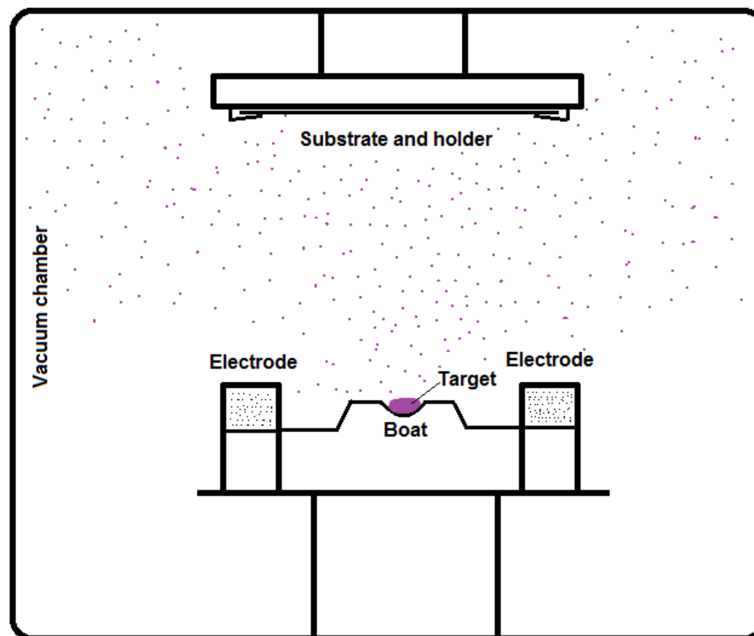

Figure 3.4: An illustration of a thermal evaporation chamber. State of the art systems usually have more than one target, and a quartz crystal microbalance (QCM) in order to measure growth rate and thickness in-situ.

In order to limit the application of metal to the desired area only, some parts of the sample need to be covered with a mask. In this case, the mask is a Si wafer with the correct geometry cut out by laser. In the Kurt J. Lesker-system, several samples can be processed

simultaneously, depending on the sample size. For the electrical measurements in this work, both sides of the wafer need to be metallized. In order to deposit on both sides, the samples have to be taken out of the system, flipped, an put back in with a different mask. A sketch of the mask for both sample sides is shown in Figure 3.5, where the white areas are opened up by the laser cutter.

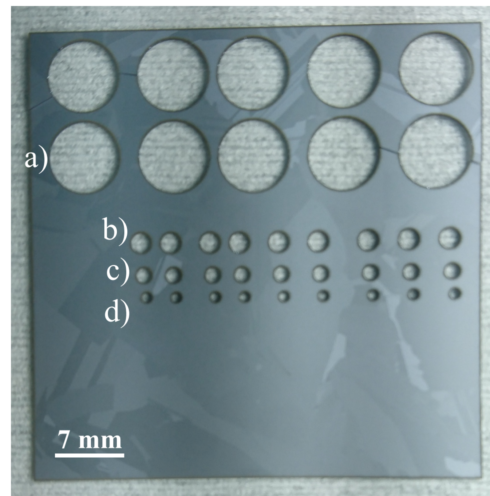

Figure 3.5: A picture of the mask used for the metallization. The radii of the holes are a) 3.5 mm, b) 1 mm, c) 0.75 mm and d) 0.5 mm.

When forming an ohmic contact with a semiconductor, it is important to choose a metal with a desirable work function. For p-type base Si solar cells, Ag and Al are the most common contacting metals on the front side and back side of the cell, respectively. In this work, however, Ag is used both as the MIS structure metal, and as the contact material for the p-type silicon, which should give some Schottky effects.

3.3 Characterization techniques and Sample Analysis

In this section, the different characterization methods will be described. The Capacitance voltage subchapter is largely based on chapter 6 in *Semiconductor Material and Device Characterization* by D. K. Schroder [66] and the PL-V section is based on several papers by Haug et al. [67], [68], [29].

3.3.1 Spectroscopic Ellipsometry

Ellipsometry is an optical method of measuring (among other things) the thickness of thin films. The technique is based upon sending polarized electromagnetic waves on a sample and measuring the change of polarization of the reflected or transmitted light. The data is then compared to a model, which then allows for the extraction of the desired characteristic. In this work ellipsometry is used as a way of measuring the thickness of the Al_2O_3 thin films. The measurements are performed on a Woolam Alpha SE located at the MiNaLab and have been analyzed using the Complete Ease software.

3.3.2 Capacitance-Voltage Measurements

The capacitance-voltage (CV) measurement method used on a metal-insulator-semiconductor (MIS) structure, shown in Figure 3.6, is well known for its ability to determine the static charge density in a dielectric film [63], [69], [70]. In this instance, the technique is performed using a Keithley 4200-scs semiconductor characterization system located at IFE.

Capacitance is defined as,

$$C = q\frac{dQ}{dV}, \tag{23}$$

where Q is the charge in coulomb and V is the applied bias, most often given in Farads (F) or Farads per area (area specific capacitance). The measurement is done by applying a bias over the MIS structure and measuring the capacitance as a function of the applied AC, which enables the measurement of variations in current. By definition, a current is the change in Q over time, hence the variations in Q can be drawn from the varying current. The small AC voltage is applied simultaneous to a DC-sweep, which is applied to achieve the desired band bending across the structure. The sum of all charges in the structure must be zero, hence the charges arising from the applied voltage is canceled by the sum of the induced charges in the space charge region Q_{SC}, the fixed charges in the dielectric layer Q_f, and the interface charges Q_{it}. If one then assumes that Q_f is independent of V, this contribution can be obtained where the band bending in the semiconductor is 0, which is at flatband conditions, V_{fb}.

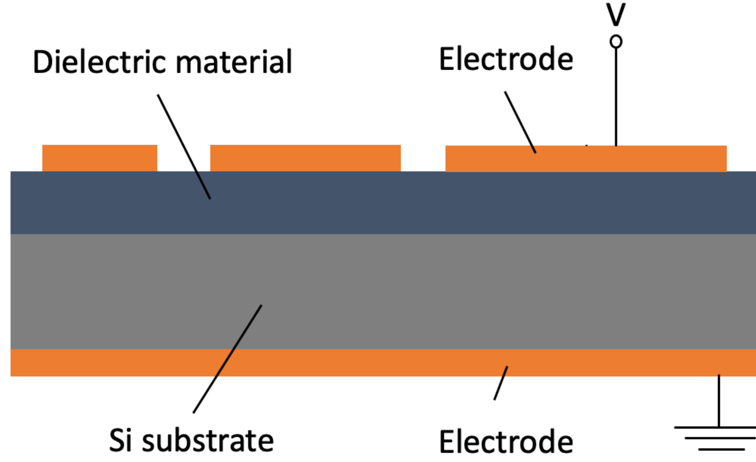

Figure 3.6: Illustration of the MIS-structures measured in this work. Different sized electrodes were fabricated as to avoid leakage currents through possible pin-holes in the dielectric thin-film.

As the applied voltage drop across the structure is a sum of the drops across the insulator and the space charge region, the total capacitance is a sum of the capacitance from these layers, which can be modeled as individual parallel plate capacitors. The capacitance arising from the interface states (C_{it}) are considered to be in parallel with the capacitance from the space charge region (C_{SC}), this implies that the total capacitance is given by,

$$C = \frac{1}{\frac{1}{C_i} + \frac{1}{C_{SC} + C_{it}}} = \frac{C_i(C_{SC} + C_{it})}{C_i + C_{SC} + C_{it}}, \quad (24)$$

where C_i is the capacitance of the dielectric layer. Considering the equation, one can see that if C_{SC} is very large compared to C_{it}, which is in fact what occurs at large negative voltages (accumulation), the total capacitance is equal to C_i. Equation (25) describes the gate charge as,

$$Q_g = \frac{C_i}{q}\left(V_g + \Delta\phi_{ms} - \psi_s\right) - \frac{Q_f d_f}{2d_i}, \quad (25)$$

where d_i is the dielectric thickness, d_f is the thickness of the region which Q_f is located, $\Delta\phi_{ms}$ is the work function difference between the metal and the semiconductor and ψ_s is the surface potential of the semiconductor. $\Delta\phi_{ms}$ for p-type Si can be calculated using

$$\Delta\phi_{ms} = W_{metal} - \chi_{Si} - \frac{E_g}{2} - \frac{k_B T}{q} ln\left(\frac{N_a}{n_i}\right), \quad (26)$$

where W_{metal} is the metal work function. By implementing flatband conditions in equation (25) i.e. $\psi_s = 0$ and $V_g = V_{fb}$, then assume that Q_f is much larger than the Q_{it} and finally that Q_f is located at the dielectric / semiconductor interface, the charge density in the dielectric film is then calculated through,

$$Q_f = \frac{C_i}{q}\left(\Delta\phi_{\mathrm{ms}} - V_{fb}\right). \tag{27}$$

The calculations in this thesis are performed with a special-made Python script, provided in Appendix A.

3.3.3 Quasi Steady-state Photoconductance

Quasi Steady-state Photoconductance (QSSPC) is a non-destructive, contactless carrier lifetime measurement technique. It was proposed by Sinton and Cuevas [71], and is now a standard setup in solar cell laboratories. The setup uses a conductive coil to measure the conductivity of a sample under illumination, which is then used to calculate the excess carrier density. In this work, QSSPC measurements are not only used as a source for determining the carrier lifetime, but also as a way of calibrating photoluminescence (PL) images. Photoluminescence is discussed below, and the QSSPC setup used is integrated in the PL imaging system.

$$\frac{d\Delta n(t)}{dt} = G(t) - U(t) + \frac{1}{q}\,\nabla J \tag{28}$$

The technique uses equation (28) as a basis for calculation of carrier lifetime, where Δn is the excess carrier density, G is the generation rate, U is the recombination rate and ∇J is the depth gradient in the current density. As the system is setup with light filters in order to generate an equal excitation of carriers throughout the sample, this value can readily be approximated to 0. By inserting the following relation,

$$U = \frac{\Delta n}{\tau_{eff}}, \tag{29}$$

an expression for the effective lifetime is obtained, which relates to the generation rate as well as the injection level:

$$\tau_{eff} = \Delta n \frac{(t)}{G(t) - \left(\frac{d\Delta n(t)}{qW_{ref}}\right)}. \quad (30)$$

From this the effective lifetime can be determined by measuring the generation rate and injection level simultaneously. The injection can be determined from the excess conductivity of the sample through

$$\Delta \mathrm{n(t)} = \frac{\Delta\sigma(t)}{q(\mu_n + \mu_p)W}, \quad (31)$$

where $\Delta\sigma$ is the excess conductivity and μ_n and μ_p are the mobilities of electrons and holes, respectively, and W is the sample thickness. From these equations, a depth average effective lifetime over different injection levels is obtained. This can be used to calculate S through equation (16), which is used as a measure for the surface passivation quality.

3.3.4 Photoluminescence Imaging

The Photoluminescence Imaging, or PL-I, here used as a camera-based carrier lifetime measurement technique and is performed on a BT Imaging LIS-R1 system located at IFE. An illustration of the setup can be seen in Figure 3.7. It is used extensively as a characterization method for crystalline silicon wafers and solar cell materials, as it does not require any contacting. The method gives a fast way of determining the quality of the material and provides a lifetime image of the sample with high spatial resolution. Since it is fast and non-destructive, it is also used as a means to characterize solar cells inline during production, which is very helpful for process control [72].

Luminescence is the emission of electromagnetic radiation at relatively low temperatures [12, pp. 450-452]. The emission is generated by radiative recombination, and if the recombining carriers are generated by light, the phenomena is called photoluminescence (PL). The PL emission rate is equal to the radiative recombination rate, since one electron-hole-pair only generates one photon when they recombine. It is the intensity of the PL signal, I_{PL}, which is used to find the injection level through

$$\Delta n(x,y) = \sqrt{\left(\frac{N_a}{2}\right)^2 + \left(\frac{I_{PL}(x,y)}{C_{cal}B_{rad}}\right)} - \frac{N_a}{2}, \quad (32)$$

where C_{cal} is a calibration constant taking instrument and sample specific parameters into account, specifying the fraction of the emitted light that is detected. At low injection conditions, I_{PL} is proportional to the injection level by setting $N_a = p$. As the measurement is performed in steady state, the effective lifetime can be calculated from the injection level through the simple relation $\tau_{\text{eff}} = \Delta n / G$. The calibration constant C_{cal} relating the injection level to the PL intensity is calculated from a separate QSSPC calibration measurement built into the PL setup.

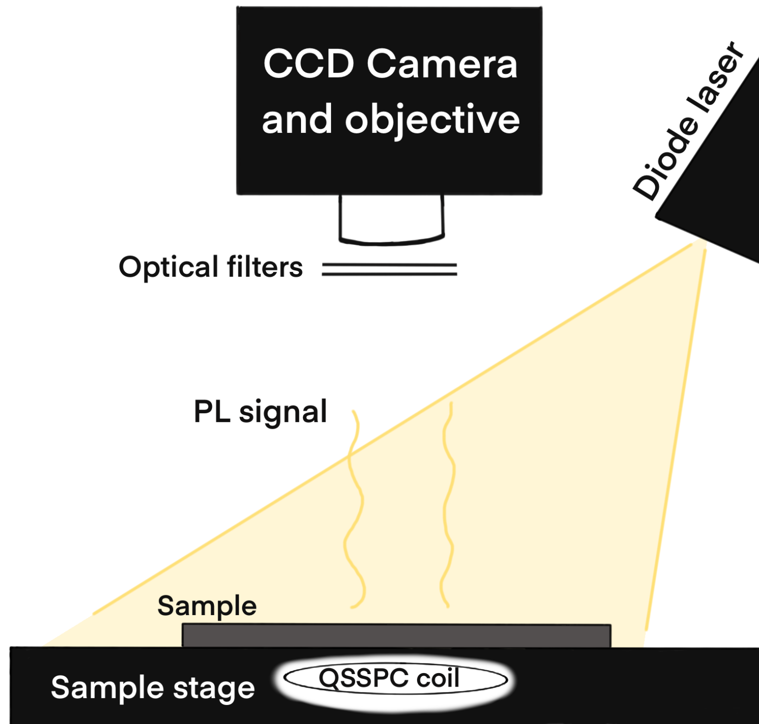

Figure 3.7: Illustration of the BT Imaging PL-I setup at IFE.

In the BT Imaging LIS-R1 there is a Sinton QSSPC stage incorporated into the measurement system. Earlier systems did not necessarily have a calibration mechanism, which made PL-I mostly useful for evaluating uniformity variations across the wafer, rather than giving specific values for the lifetime. In this work, PL-I have been used for both of the above-mentioned characteristics, which have given fruitful data in the process development phase.

3.3.5 Photoluminescence Imaging under applied Voltage

The Photoluminescence Imaging under applied Voltage (PL-V) method was first purposed by Haug et al. to measure the SRV of passivated silicon surfaces at varying band bending conditions. The most common method to achieve this is to add charged ions on top of the dielectric in a corona charging setup [67]. These techniques are used to characterize the surface passivation of a sample, determining characteristic parameters like S_{n0}, S_{p0} and Q_f. Although the surface passivation is the combined effort of both chemical and PL-V are, to some extent, able to separate the contributions from field-effect and chemical passivation.

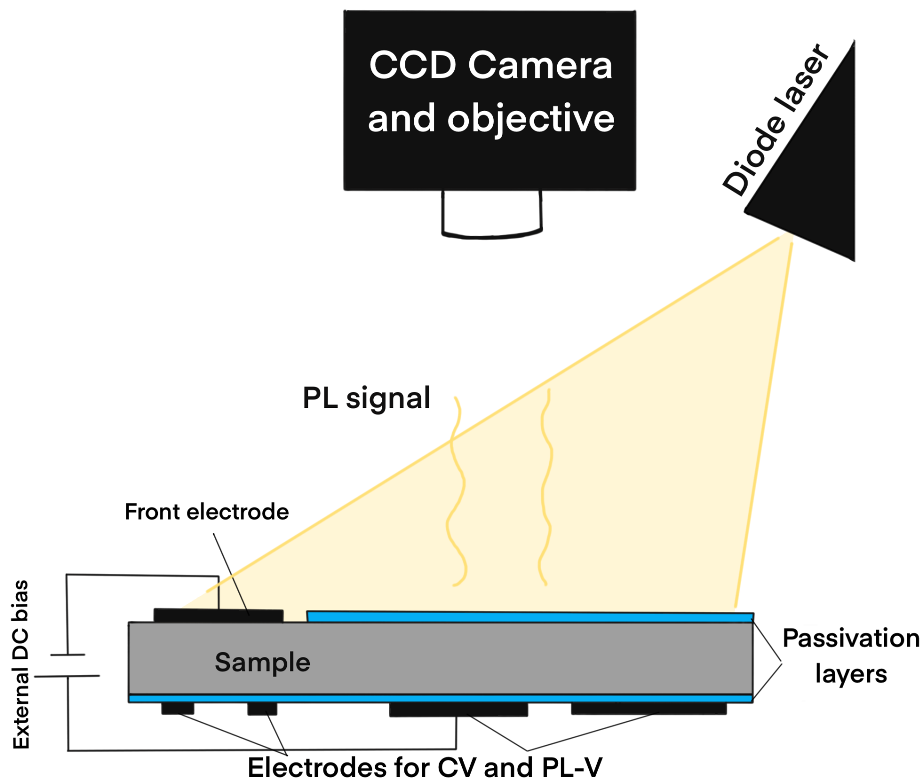

Figure 3.8: Illustration of the PL-V setup.

The measurements are performed using the BT Imaging LIS-R1 PLI setup, with additional electric probes and the internal voltage source, normally used for cell measurements, as shown in Figure 3.8. The flux was set to 2.73E+17 cm^2 and the exposure time was 0.3 s.

In corona charging, the user must deposit charged ions with a specific concentration onto the surface of the sample. This is a time-consuming process, since several measurements needs to be performed in order to achieve the resulting trend. Several depositions with subsequent measurement and ion removal must also be performed. PL-V on the other hand, enables the user to do quick measurements of the same characteristics. As the measurements

are fast, high resolution τ_{eff} vs. voltage can be acquired. The applied voltage simulates charges in the surface film contributing to the field effect passivation. By varying the voltage different charge concentrations can be simulated. By looking at the carrier lifetime at flat-band conditions, where the field-effect is canceled, a value for the contribution from the chemical passivation can be drawn.

To be able to apply bias to the samples, they need to be metallized on both sides, as described in Section 3.2.4. However, this changes the rear side reflectance of the samples, which affects the measured Δn, as the reflected wavelengths enhances the PL signal over the metalized regions. This is considered by implementing an optical enhancement factor, f_{oc}, which is determined experimentally by measuring the increase of the PL signal of the samples when they are put on top of an Al mirror.

3.3.5.1 Analysis of PL-V Measurements - Theory

The PL-V analysis was performed by Halvard Haug using a self-made Matlab script. In order to analyze the data obtained from PL-V, the Girisch model is utilized [68]. The model, described in [73], provides an approximate result to the surface band bending under the approximation of constant quasi-Fermi levels across the space charge region near the surface. The model utilizes that the effective SRV associated with the interface states is given by,

$$S_{it} = \frac{U_s}{\Delta n(x = d_{sc})}, \tag{33}$$

where U_s is the recombination rate at the surface and $x = d_{Sc}$ is the injection level at the surface space charge region. By also implementing the fact that surface recombination is a function of n_s and p_s, which is the concentration of electrons and holes at the surface, and the electrical properties of the surface defects, $D_{it}, \sigma_n, \sigma_p$, ($\sigma_{n/p}$ are the capture cross section for electrons and holes) and assuming low injection conditions, it can use that

$$\Delta n = \frac{n_i^2}{N_A}\left(e^{\beta V_b} - 1\right), \tag{34}$$

where $\beta = q/k_bT$, V_b is the separation of the quasi-Fermi levels for electrons and holes. Then, by inserting the surface potential, ψ_s, into the expression relating the carrier concentrations to the potential, we get

$$\mathrm{n_s} = n_b e^{\beta\psi_s(x)}, \tag{35}$$

where $n_b = \Delta n$ (at low injection). p_s can be calculated using the same equation, just switch out n_b with p_b. This implies that the calculation of the effective SRV when surface band bending occurs is reduced to acquiring the surface potential. This can be found by solving the continuity equation as well as the Poisson equation, which are most often not solvable analytically. The Girisch model solves this numerically. It calculates values for Q_g through (25), Q_{it} through

$$\mathrm{Q_{it}} = q \int_{E_c}^{E_v} \left[D_{it,d}(E) f_d(E) - D_{it,a} f_a(E)\right] dE, \tag{36}$$

where f_d and f_a is the occupancy function for holes and electrons, respectively, and Q_{sc} through

$$Q_{sc} = \mp \sqrt{\frac{2n_i\epsilon}{q\beta}\left(e^{\beta(\phi_\mathrm{p}-\psi_s)} - e^{\beta\phi_p} + e^{\beta(\psi_s-\phi_n)} - e^{-\beta\phi_n} + \beta\psi_s\left(\frac{N_A-N_D}{n_i}\right)\right)}, \tag{37}$$

the minus and plus sign in front of this equation is used when $\psi_s > 0$ and $\psi_s < 0$, respectively. This is done for varying ψ_s values, and the correct ψ_s is found where $Q_{tot} = 0$,using the charge neutrality condition. Now that ψ_s is determined, we can calculate n_s and p_s through (35), and the SRV and at last τ_{eff} through (33) and (16).

An additional effect, routinely attributed to the SRV parameter, is the recombination in the subsurface damage region [74]. When highly recombination active defects are present in the subsurface region and the system is in inversion conditions, implying that the concentration of electrons and holes are comparable, it leads to an asymmetry in the SRV for inversion and accumulation conditions. This is corrected for by implementing a parametrization;

$$S_{SDR} = \begin{cases} S_{min,n}\ for\ \psi_s < 0 \\ S_{min,p}\ for\ \psi_s > 0. \end{cases} \tag{38}$$

These parameters are observed values on each side of the minimum value for the SRV and are used to avoid a bloated lifetime in the theoretical model.

Two other important parameters for adjusting the model is the S_{p0} and S_{n0}, which are the SRV parameters for the majority and minority carriers. These can be determined by the ratio

of their capture cross sections. These parameters are used as free fitting variables and will affect the steepness and the asymmetry of the τ_{eff} vs. V curve.

3.3.6 Secondary Ion Mass Spectrometry

Secondary Ion Mass Spectrometry (SIMS) is a destructive characterization technique, which can be used to map impurities in a sample and can also create depth profiles of the elements. It utilizes an ion beam to sputter the sample surface, generating secondary ions from the sample. These secondary ions are extracted using an electric field and accelerated, creating a secondary ion beam, which is separated in a mass spectrometer, before they reach the detector. In order to increase the ionization of the different sputtered atoms and molecules, different ions have to be used for the primary ion beam. To enhance negative secondary ion a Cesium-beam is used, and for a positive, an Oxygen-beam is used. One of the main uses for SIMS is to characterize impurities in solids, with detection limits at ppm and ppb depending on the element of interest. In this work, the technique is used to detect impurities in the deposited Al_2O_3 films and the measurements were performed on a Cameca IMS-7f at MiNaLab.

A challenge with using SIMS for films as thin as 20 nm is that the measurement sputters quickly through the layer, giving of relatively few molecules in the process. This lowers the signal-to-noise ratio to some extent. To correct for this, one can perform several measurements at slightly different location on the sample and then taking an average of all the measurements performed, however, this was not performed in this work.

3.3.7 Fourier Transform Infrared Spectroscopy

Infrared (IR) spectroscopy is an optical technique for characterizing the chemical composition of a material from the vibration of its atomic constituents. A molecule can absorb specific energies depending on their bond strength and reduced mass, which excites it into higher vibrational states. This vibration, in turn, is detected as an absorption band that serves as a 'finger print' for that molecule.

Modern IR instruments are based on the Fourier Transform (FT) principles. Unlike ultraviolet-visible (UV-Vis) spectrometers, where light from a broad source is dispersed using prisms or gratings, FT-IR spectrometers utilize the entire source output. The IR beam is first

sent into a Michelson interferometer, which allows the amplitude of the beam to be modulated. The intensity of the amplitude-modulated beam is measured by the detector and is plotted as a function of the moving mirror position, resulting in an *interferogram*. The FT of the interferogram recovers a so-called *single channel* spectrum that is determined by all components of the instrument, i.e., the emission profile of the light source, the reflectivities of the mirrors, the efficiency of the beam splitter, and the responsivity of the detector, as well as the sample itself. Thus, FT-IR spectrometers require two measurements: with and without the sample in the beam path. The ratio of the spectrum measured with the sample to the spectrum measured without the sample is then the true spectrum of the sample.

Table 3: Setup parameters for FT-IR spectroscopy. Measurements performed at RT.

Type	Specification
Source	Mid-infrared
Beamsplitter	KBr
Detector	MCT-mid D316
Resolution	4 cm^{-1}
No. scans	256 for the reference and samples

In this work, FT-IR spectroscopy was used to measure the Al_2O_3 thin films were to check for vibrational bands indicative of either anomalies in the bonding structure (different Al-O bonding environments) or contamination from extrinsic impurities (H- and C-related bonds). FT-IR was performed on Bruker IFS 125 HR with the setup described in Table 3.

4 Results and Discussion

In this chapter the experimental results will be presented and discussed. First, the general experimental procedure for optimizing the deposition process for passivation purposes will be presented chronologically. Second, issues regarding chamber cross contamination and the effect of this will be presented and discussed. Here, FTIR and SIMS results will be discussed.

Then, electrical characterization of MIS structures will be presented, as well as some PL-V measurements. The last part focuses on AlO_x as a tunneling oxide. Simulations of a tunneling contact structure will be presented here, and lastly IV characterizations of hybrid PEDOT:PSS / Si solar cells, with an ultrathin passivating AlO_x interlayer will be presented and discussed.

4.1 Passivation Process Development and Optimization

One of the objectives for this work was to develop a process for surface passivation using the TFS-200 for ALD-grown Al_2O_3 films at the MiNaLab.

4.1.1 Initial Experiment

The pre-existing recipe for Al_2O_3 deposition on the equipment were tested on a CZ grown p-type Si wafer cut in smaller samples using a diamond pen. The samples went through a HF-dip in accordance with the "later process" in Table 1, then put on a clean dummy wafer on the sample stage inside the reactor. The reason for the change in cleaning parameters were changes in the HSE regulations for the HF concentration, which were lowered to 2% after the initial experiments. This, in turn, led to changes in etching times. The deposition parameters for the standard process are given in Table 2, with 167 cycles at 200°C for a 20 nm thick film. In order to acquire film on both sides of the samples, the deposition process was repeated once after the samples were flipped. This turned out to give issues with the thickness of the films, as the precursors were able to penetrate beneath the sample to some extent, depositing film on the back side of the sample as well. The measured thickness, performed with the ellipsometer presented earlier, where therefore split between approximately 20 nm in the center, and close to 40 nm at the area around it.

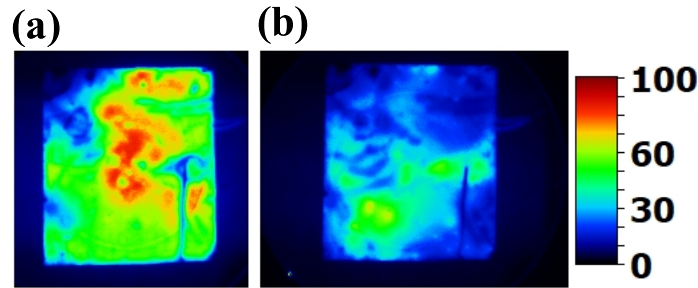

Figure 4.1: PL-I mapping of sample CZ_003 (a) before and (b) after a 25 min anneal at 425°C. Passivation has not been achieved and is even weakened over time, or after the annealing step. Annealing parameters obtained from *[63]* Scale in μs.

PL-I were performed on the samples in order to determine if any passivation effects could be observed prior, and subsequent, to annealing, as shown in Figure 4.1. The figure shows some indications of passivation, although not to the expected extent. The timing for the experiment made it impossible to do PL-I measurements and annealing on the same day. Samples were stored in ambient atmosphere and room temperature for 41 days before annealing. The stability of the passivation is not known for these samples, and for that reason, the samples were abandoned from further characterization, as we wanted to optimize lifetime and uniformity prior to electrical characterization. Another issue with this experiment were the sample sizes. They were smaller than the calibrating QSSPC coil, which could contribute to some losses in accuracy with regards to the lifetime measurement.

4.1.2 Surface Passivation Quality

In this section, the experiments and results for the surface passivation process that was developed and optimized will be presented and discussed.

4.1.2.1 Two-sided oxide layer deposition and uniformity

In order to realize the potential uniformity of ALD and to increase the repeatability of the process, a two-sided deposition was deemed important. Although some previous work showed good results by taking the sample out of the ALD chamber, flipping it, and loading it in again [64], the preliminary experiment in this work showed that the precursors penetrate beneath the sample if put directly on a Si substrate placed on the sample holder. By performing a one-sided deposition, the sample is then bound to acquire twice the thickness at the edges of the sample,

extending some distance in towards the center. At the ALD setup in MiNaLab the two-sided deposition is not a standard alternative. Several solutions are proposed for this in this section. The different prototypes are shown in Figure 4.2.

For the first experiment, two parts of a Si wafer were stacked on top of each other; Stand A (Figure 4.2 (a)). However, the uniformity of the passivation on these samples were insufficient as shown in Figure 4.3. In addition, a "dead zone" at the stand's point-of-contact indicates that the film coverage here is far from ideal. This indicates that the uniformity of the film is affected by the lifting technique, or that the ALD process is unsaturated. There were two possible approaches two meet this issue; change the ALD recipe, lengthening the pulsing times of the precursors, and/or improve the stand enabling two-sided deposition. As the process parameters used was well established prior to this work, it is more likely that it is the stand causing the low uniformity of the samples. Therefore, a Stand B were made out of folded aluminum foil to only contact small points at the edges in order to support the sample, which is illustrated in Figure 4.2 (b).

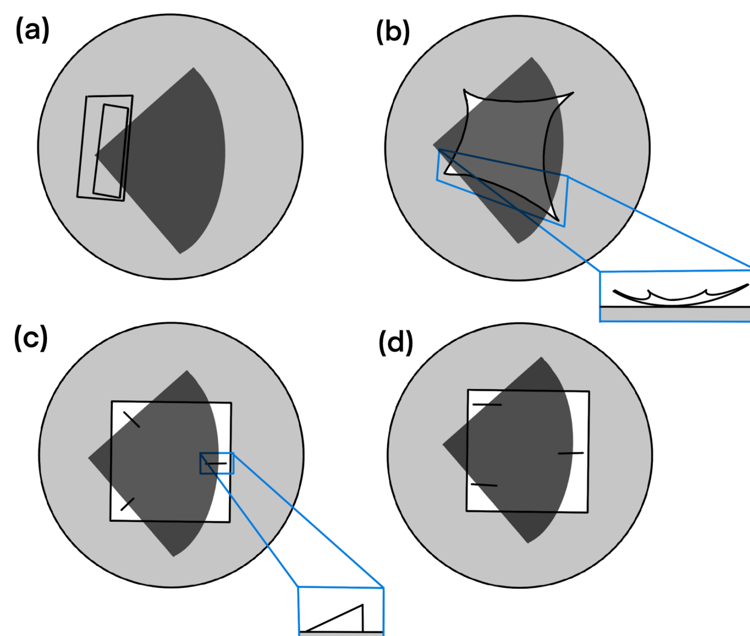

Figure 4.2: Illustration of the different prototypes of sample stands. Where (a) Stand A is consisting of two pieces of Si wafer stacked on top of each other, (b) Stand B is the first of the three aluminum foil stands, (c) Stand C is the first with fins and (d) Stand D is the final stand, giving the most promising results.

As Stand B only touches the edges, the precursors are able to cover the entire surface area on the sample, as well as to penetrate beneath the stand contact points. The deposited films on the samples using Stand B showed promising improvements to the uniformity of one sample, as seen in Figure 4.3 (b), although still below expectations. Note that the samples used from

here on are FZ Si from Topsil, with a τ_{bulk} of approximately 2 ms. The experiment with Stand B showed that there where potential in the stand design. However, the stand's shape could give some turbulence in the chamber since its shape is curled and therefore forcing some precursor gas underneath itself. On that background, Stand C was designed, not only to counteract the probable turbulence, but to have fewer contact points with less contact area. This stand is based on a flat base with three fins supporting the sample above. The positioning and angling of these fins are showed in Figure 4.2 (c), which give a uniformity that is sufficient for the planned experiments. After issues with cross contamination in the chamber, which will be addressed later in this chapter, the stand was deemed as contaminated, and Stand D was prepared. The only difference between Stand C and D is the angle of the fins, which are better lined up with the gas flow in the reaction chamber. A possible effect of changing the angle of the fins in Stand C can be seen in the distinction between Figure 4.3 (c) and (d).

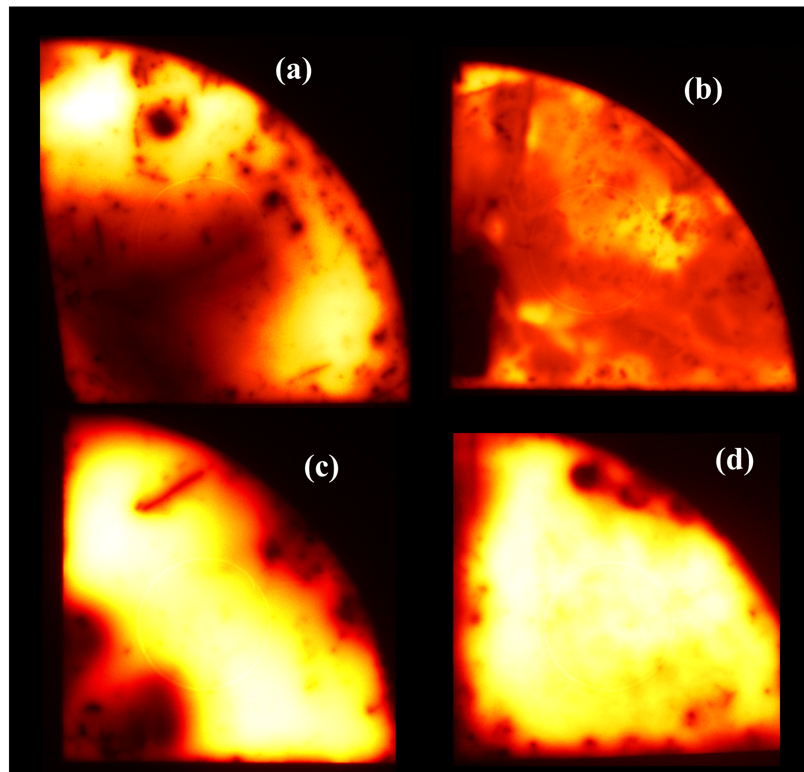

Figure 4.3: PL-I mappings of samples deposited with Stands A-D corresponding to (a)-(d). Note that no units are provided, since we are now looking at the stands effect on uniformity only. The dark spot in (b)-(d) most likely originate from poor handling and not the film deposition.

In Figure 4.3 (a)-(d), samples deposited on using the different stand are presented. The figure shows an increase in uniformity from (a) to (d). The lines of black spots found in (d) are a typical example of damage occurring when using a metal tweezer to handle the samples prior to the application of the passivation layer. The improvement in uniformity lead to the continuing

use of Stand D throughout this work. The use of a metal tweezer was abandoned, and a plastic tweezer were utilized as a replacement for the remaining experiments.

4.1.2.2 Passivation layer activation

In order to activate the passivation quality of the AlO_x layer, a post deposition annealing step must be performed [23], [35], [64], [70]. Different annealing temperatures and duration for passivation layer activation have been previously investigated/optimized and can be seen in Table 4. On the basis of these references, giving the anticipated optimum temperature range of a post deposition annealing, two annealing experiments were done with 9 samples. In order to investigate the passivation layer activation, lifetime measurements were carried out. These were performed in accordance with Section 3.3.4, with the calibrating QSSPC measurement giving the effective lifetime at 1 sun reported later in this section. S_{eff} was calculated using equation (16), with τ_{bulk} being 2 ms. The samples were prepared as described in Sections 3.2.1 and 3.2.2, with 167 cycles giving a 20 nm AlO_x film on both sides of the samples. Next, they were annealed at temperatures between 350°C and 450°C for 10 minutes, as this was reported to be in the range for passivation layer activation [35].

Table 4: Overview of some of the previously investigated/optimized annealing parameters.

Source	**Temperature**	**Time**
Kerstens et al. **[28]**	470 °C	10 min
Dingemans et al. **[35]**	350 °C – 450 °C	25 min
Vanadana et al. **[64]**	400 °C	100 s
Kühnhold-Posposchil et al. **[70]**	420 °C – 500 °C	2 min – 16 min

The results for the annealing experiment can be seen in Figure 4.4, where a peak in lifetime and low point in SRV is found at an annealing temperature of 400°C. From Figure 4.4 it becomes clear that the passivation activation temperature for a 10 minute anneal is found lower than 350°C, and full activation occurring close to 400 °C for the samples in this work. The optimum conditions in this work is shifted somewhat to a lower annealing temperature and a shorter duration compared to [70]. The origin of this shift is challenging to reveal, as the

literature does not specify what precursors were used for the AlO_x deposition. As the oxygen source in this work is water vapor, the hydrogen content in the film might play a larger role than if ozone is used as the oxygen source. Assuming that [70] used ozone, the hydrogen content is already lower than in our samples, decreasing the effect of increased hydrogen effusion occurring at higher annealing temperatures, which could give a partial explanation for the results. Another possible explanation could be calibration differences in the measured annealing temperature and the actual temperature in the annealing furnace.

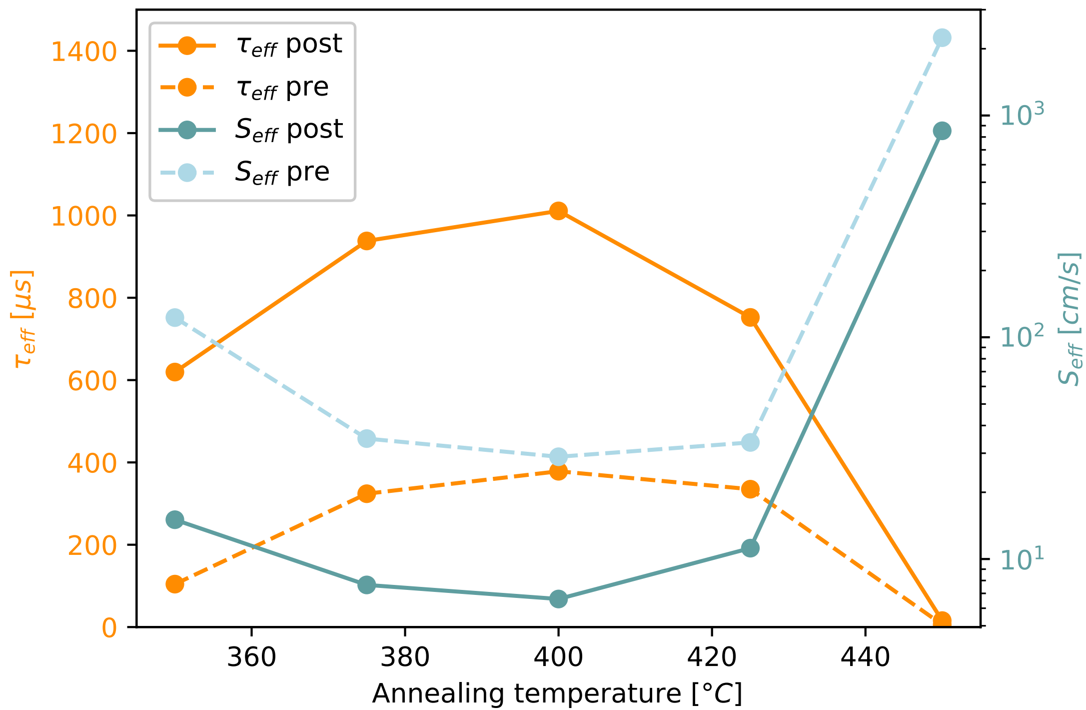

Figure 4.4: The orange graphs shows the effective lifetime against annealing temperature at values of 350°C to 450°C, with steps of 25°C. The stippled lines represent the samples prior to annealing. The annealing time were set to 10 min for this experiment, after the preliminary experiment tested 25 min, giving poor activation of the passivation layer. The blue plots are of the SRV vs. the annealing temperature, giving a more comparable view of the results. As the figure shows, values close to 10 cm/s are achieved for the optimum temperature in this experiment, which is evidence for a good surface passivation.

The shift could be due to natural variations within deposition systems or annealing methods. In the mentioned references in Table 4, most anneals performed in ambient atmosphere were done using a hot plate rather than an oven. This could also lead to some differences in the thermal gradients within the samples, as the ramp up time (i.e. the time it takes for the sample to reach the annealing temperature from room temperature) is probably somewhat shorter when the heat is radiating from all directions, rather than just one.

4.1.2.3 Effects of deposition temperature

The deposition temperature is reported to have a significant effect on the passivation quality for ALD AlO_x films deposited on silicon [35], [75]. The typical deposition temperature for thermal ALD using the TMA/water process is $\leq 300°C$ [52]. Results from several experiments performed are shown in Figure 4.5, with deposition parameters provided in Table 5. The figure shows a relatively flat SRV vs. dep. temp. curve from 50 °C to 200 °C, then the SRV increases drastically towards 350 °C. The rapid increase in SRV above 200 °C is an expected behavior as previously reported in the literature [76], and in [35] the relevant deposition temperature range referred to is 150°C - 250°C. Hydrogen and carbon content were observed to decrease with increasing deposition temperature. Although hydrogen is known for its contribution to passivation of dangling bonds, carbon is more known for the opposite. Hence, a trade-off between carbon and hydrogen content in the film should yield a better passivation. The passivation quality achieved at low temperatures is unexpected, as good passivation results for low temperature (below 200°C) thermal ALD is rare to locate in the literature. On the other hand, low-temperature ALD AlO_x have been reported to give extremely conformal and high-quality films with otherwise good electrical and optical properties [77]. The higher hydrogen content in the low temperature films might also contribute to a better passivation.

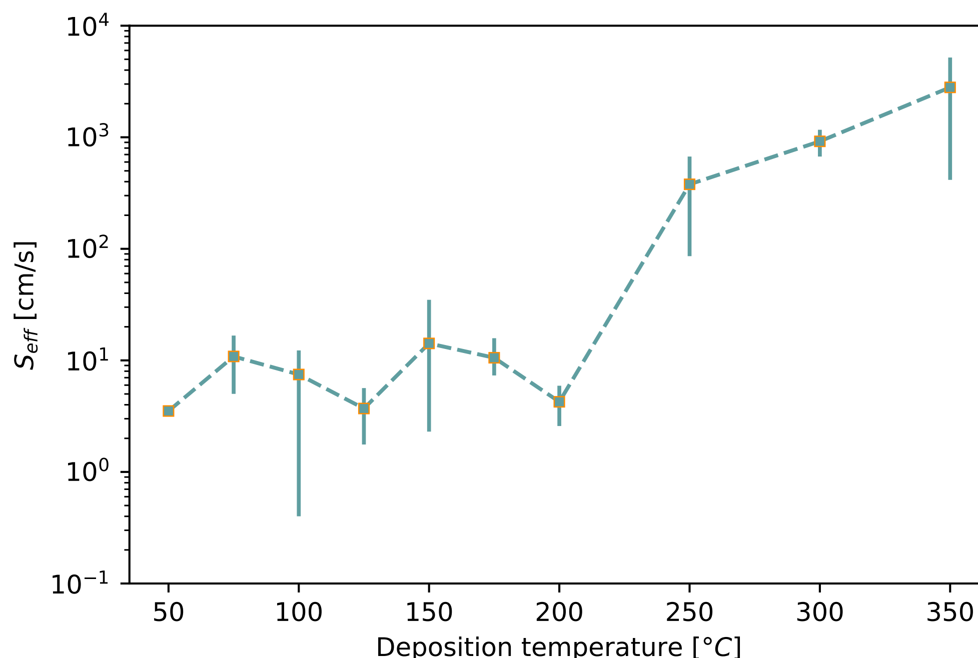

Figure 4.5: The figure shows the results of the deposition temperature experiments. The dots and the stippled line is the average value at each temperature. The deposition temperature with the least spread in measured lifetime is 50 °C, where the difference from highest to lowest lifetime was 93 μs. Too few samples were made in order to determine with certainty which deposition temperature provided the most reproducible result, however as 100 °C showed the lowest SRV-value, it was decided to continue with this as the deposition temperature. It should be noted that the initial results

From this data it is hard to determine an optimum deposition temperature since there are large variations in SRV for the same temperatures. However, the potential passivation quality at 100 °C is seemingly larger than at other temperatures. Thus, it was determined to use this temperature for the later processes.

Table 5: Overview of the process parameters for the different deposition temperatures. All depositions where done with 167 ALD cycles, for which the expected thickness is 20 nm. However, a variance in thickness is expected as the growth rate of the TMA/water process is known to decrease outside the ALD window. All samples were annealed as described in Section 3.2.3.

Deposition Temperature	Puls time (TMA/H_2O/purge)
175°C, 200°C, 250°C, 300°C, 350°C	400 ms / 500 ms/ 3 s
150°C	500 ms / 600 ms / 3 s
100°C, 125°C	600 sm / 700 ms / 5 s
50°C, 75°C	750 ms / 750 ms / 10 s

The consistency and reproducibility of an ALD process is a known challenge within the ALD community [62]. As an example, the GPC for seemingly identical processes performed on different reactors by different researchers can vary significantly [78], [79]. In this work, the growth rate was relatively stable within the parameter range, however, the passivation quality of the films grown were not as stable. Figure 4.5 shows a plot which displays the achieved S_{eff} at various deposition temperatures, with the average values provided by the squares and stippled line, and the vertical lines representing the span of the S_{eff} values achieved at the given deposition temperature. As the figure shows, the span at certain temperatures ranges above one order of magnitude even when samples were made from the same wafer, and depositions on these were performed successive to one another.

These variations are seemingly occurring at random, as all sample handling are done as similar as humanly possible. Variations in bulk lifetime of the different samples can occur, this however should be of minimal impact as some samples from the same wafer are processes identically. Table 6 shows the results for four samples originating from the same wafer. Although the differences are not too large, they are definitively noticeable. A trend for this experiment in particular is the fact that the first sample processed at the specific temperature

has a lower τ_{eff} than the second. This could indicate that the temperature in the reactor has not yet stabilized at the set point before the process is initiated. This could support that the variations in deposition temperature during the process have some effect on the outcome. More research is needed to verify this.

Table 6: An overview of the latest processed samples. A wafer from a different batch is used for this experiment. 20 nm AlO_x layers, 400 °C annealing temp. Odd numbered samples are processed first at their respective temperatures.

Sample (dep. Temp.)	**15_1** (100°C)	**15_2** (100°C)	**15_3** (150°C)	**15_4** (150°C)
Post annealing τ_{eff} [μs]	709	950	882	1193

One possible reason for the scarcity of publications on low-temperature thermal ALD AlO_x for passivation purposes can be the slightly lower growth per cycle (GPC) and severe reduction in growth rate. The growth per cycle is determined by the reaction kinetics and the number of available surface species as described in [80]. The lower temperature depositions will have more available species, as the surface coverage is better, however the reaction kinetics are much slower because of the thermal activation barrier. At higher temperatures, the behavior is opposite; the reaction kinetics is faster, but the available surface states are limiting the growth rate as the coverage is lower. This leads to some decrease in the GPC, which is shown in Figure 4.6. This does not affect the growth rate to a significant extent. The determining factor is the pulsing times, given in Table 5, which increases drastically with decreasing temperature below 150 and with increasing temperature above 250. These results correlate with the existing literature on ALD AlO_x [52].

From this series of experiments, an optimum process flow for passivating Si in MiNaLab were established, and the parameters are listed in Table 7. These parameters where used for the samples made for electrical characterization with CV and PL-V, as well as for the verification experiment performed later.

A final note on this chapter is that the deposition temperature might have an effect on the annealing temperature. However, this was not explored in this work.

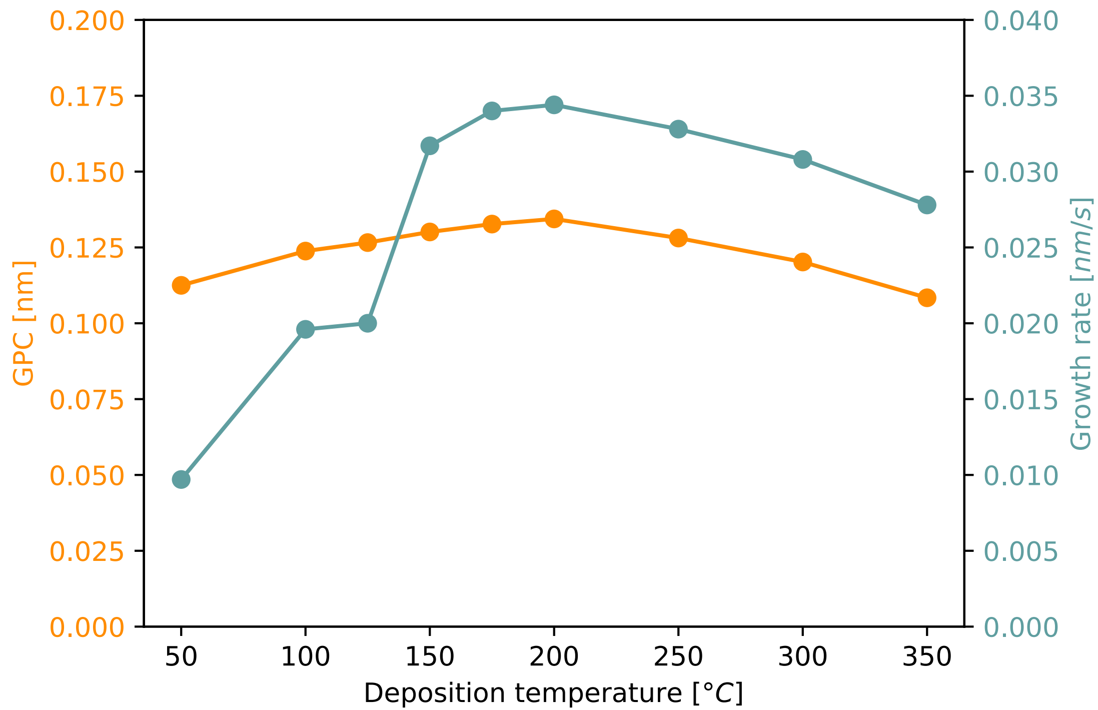

Figure 4.6: Plots of the Growth rate and GPC as a function of deposition temperature. This is an indication of why a higher deposition temperature is preferable to a lower temperature with regards to operational through put, as the growth rate is at its peak within the ALD window.

Table 7: List of the process parameters acquired in the series of experiments.

Process	Procedure/Parameters
Native oxide removal	2% HF-dip: 3 min Di-water rinse: 3 min
ALD Al_2O_3 deposition	Deposition temperature: 100°C Pulse times TMA/H_2O/N_2: 500ms/600ms/3s
Annealing	Temperature: 400°C Time: 10 min Atmosphere: open air

4.2 Cross Contamination of the ALD System

In parallel with this work, many other processes where performed on the ALD reactor at MiNaLab. Most processes were with the same material system as in this work, so these did not affect the quality of the passivation to any noticeable degree. However, one process had a detrimental effect on the passivation quality of the films made subsequent to that process. The effects of this and the work done to correct it will be discussed in this section.

4.2.1 The effect on lifetime

The process affecting the lifetime were an attempt to develop an ALD process for luminescent films using $Y(thd)_3$ (thd = 2,2,6,6-tetramethyl-3,5-heptanedionato) and naftalene-1-sulfonic acid ($C_{10}H_8SO_3H$). Samples deposited on some days after this material system where used in the same reactor showed zero effective lifetime. This were verified by additional samples processed some days later. No figures of these samples are shown, as no mappings were recorded by the PLI system because no PL signal was detected.

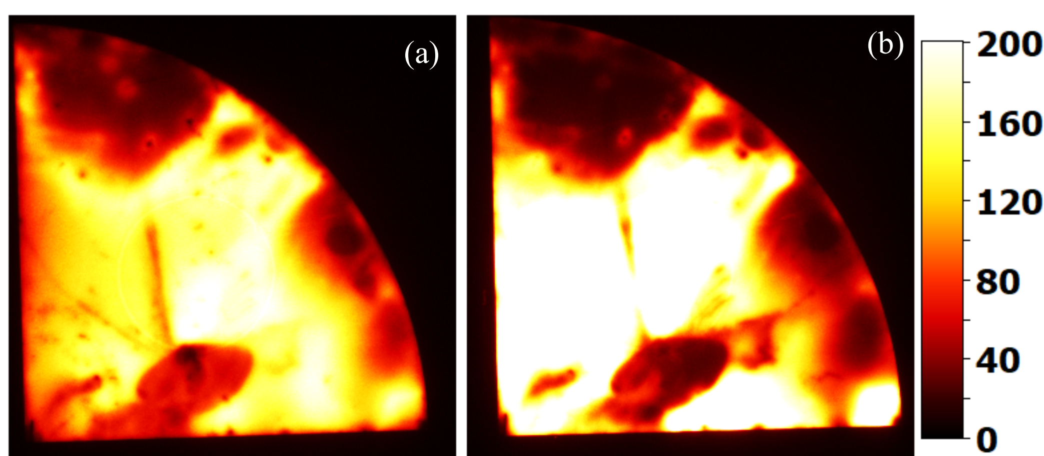

Figure 4.7: Lifetime mapping of the sample processed after the ozone purge of the chamber (a) before and (b) after annealing at 400°C. The effect of the ozone purge is significant, and the sample seems passivated in some areas. However, large "dead zones" can be seen, indicating that there still are contaminants present in the system. Scale in μs.

An attempt to clean the chamber of any organics where made by purging the chamber with ozone for 10 minutes. A sample processed subsequent to his purge can be seen in Figure 4.7. From these mappings, it becomes clear that the ozone has had an effect on the contamination level in the chamber. However, they also show large areas with no passivation, which indicates that there still are contaminants remaining in the system that is incorporated

into the film. As samples prior to the contamination showed promising results with regards to both passivation activation and uniformity. Figure 4.8 shows samples from the series previous to the zero-lifetime samples, where the passivation quality seems promising.

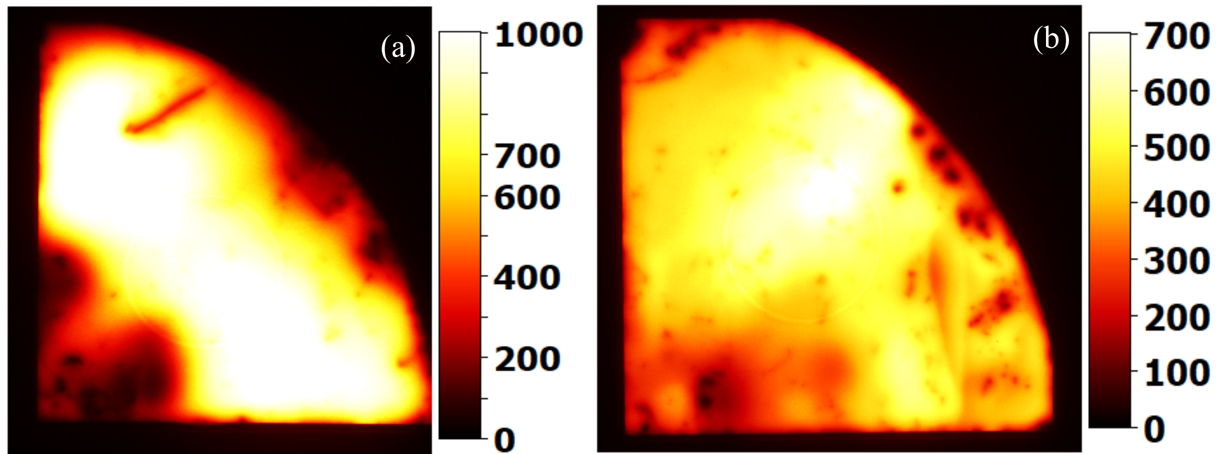

Figure 4.8: Samples from the latest series prior to contamination, annealed at (a) 400°C and (b) 375°C. Scale in μs

4.2.2 Determining the Impurity Species

As reported by Peaker et al. in [14], the effect metallic impurities can have on recombination in Si can be significant even at parts per billion (ppb) levels depending on the impurity species. This makes the detection of the specific impurity causing the decline in lifetime challenging. The material system used for the process suggests that the most likely candidates are Y, C, CH-groups or S that are causing the observed effects.

4.2.2.1 SIMS

Mass spectra of three samples processed in the ALD reactor prior to the contamination, during contaminated period and after the O_3-purge can be seen in Figure 4.9 and Figure 4.10, with Cs- and O_2+ as sources for the primary ion beam, respectively. The energy of the beams are 15keV for the Cs-, and 10 keV for the O_2+. In the spectra, the x-axis is atomic mass units, which is used to indicate which atomic or molecular species are detected. The y-axis represents the intensity of the detected species, which is related to the relative concentration of the specie in the material being investigated. A table of the relevant atomic and molecular species with their respective mass are provided in Table 8. To limit the search, the table is limited to the atomic and molecular species found in the substrate, the passivation layer, and in the precursors, both

used for the passivation layer deposition, and from the luminescent film process. By using this table in combination with Figure 4.9 and Figure 4.10, one can determine if any species' concentration are changing with the contamination level in the ALD reactor. It should be noted that SIMS have a detection limit of ppm for all elements and ppb for some elements, so the detection of species with concentrations lower than ppm level may be challenging. S for instance cannot be detected using SIMS for concentrations of 0.3 ppm and below [81].

Table 8: List of relevant atomic and molecular species possibly detected by SIMS.

Species	A.M.U.
H	1.008
C	12.011
CH_3	*15.035*
O	*15.999*
OH	17.007
Al	26.982
CO	28.01
Si	28.085
O_2	*31.998*
S	*32.06*
AlO	*42.981*
Al_2	53.964
AlO_2	*58.98*
$Al(OH)_2$	60.996
Al_2O	69.963
AlO_3	74.979

Figure 4.9 shows clear peaks in all samples at 1, 16, 26, 32, 43, 59, 75 and 83, which represents the species listed in Table 8. All these species are expected and are most likely originating from the passivation layer deposition. High peaks at different oxygen and aluminum

species is dominating, but the missing silicon peak at 28 a.m.u. indicates that the sputtering time could have been increased. The peak at 32 is most likely originating from the molecule O_2, and not S, and similar interpretations can be made for some of the other peaks in the spectra as well. From Figure 4.9 it becomes clear that no significant differences in species concentration is detected, and no apparent contaminant is determined from the Cs-beam. Cs is used in an attempt to detect carbon; however, no significant signal was detected at the carbon mass.

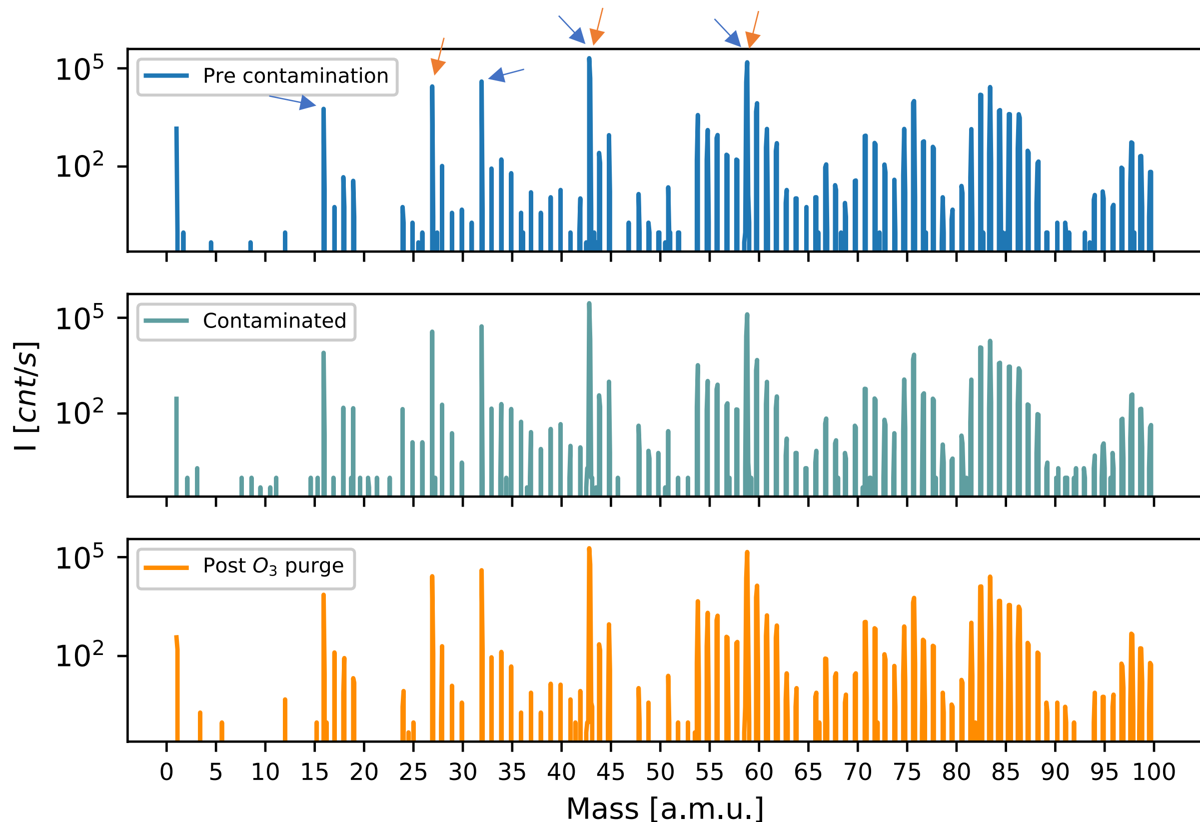

Figure 4.9: Results from SIMS using Cs for the primary ion beam. Blue and orange arrows indicate oxygen and aluminium-species, respectively

Figure 4.10 shows peaks at 1, 16, 27, 28, 43, 44, 54 and 70, all represented in Table 8. The 1-peak is very similar for the pre-contamination sample and the contaminated sample, however, for the post O_3-purge sample it is practically gone. This is the only significant difference in the three spectra, and the detected species in each sample is most likely originating from the deposition process itself. This indicates that the specie(s) responsible for the loss of passivation quality is below ppm levels, which is very much possible considering Peaker et al.'s paper mentioned earlier.

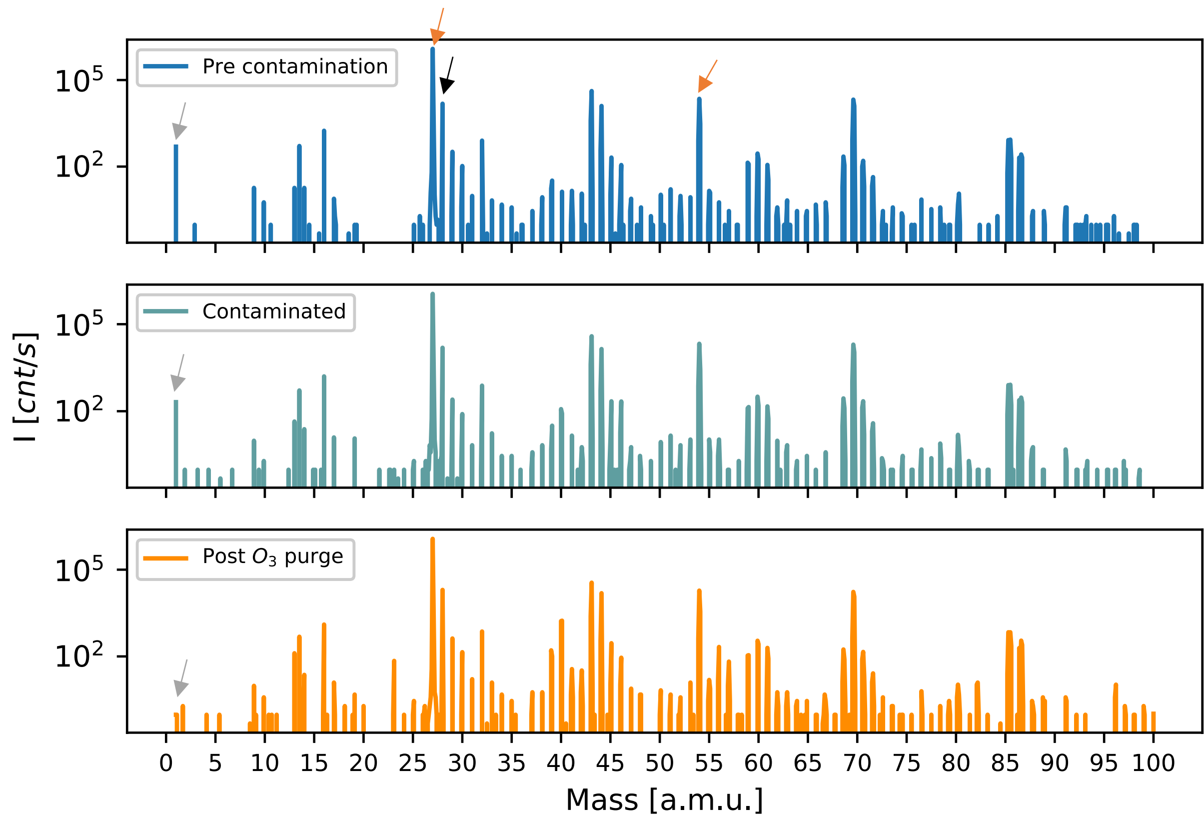

Figure 4.10: Results from SIMS using O2 for the primary ion beam. Gray arrows indicate the biggest change between the plots. The orange and black arrows indicate Al and Si, respectively.

4.2.2.2 FT-IR Measurements

In order to investigate if the binding structure of the contaminated Al_2O_3-films had any correlation with their passivation quality, FT-IR spectroscopy was utilized. Three 1 cm x 1 cm samples with varying passivation quality where investigated, with two of them (FT-IR_1 and FT-IR_2) being made out of one quarter 4”-wafer, and the third (FT-IR_3) was cut out from one sample showing τ_{eff} = 0. No PL image was saved of FT-IR_3 since the sample showed 0 lifetime which disables the PLI program to store any images taken. Figure 4.11 shows a PL image of where the samples FT-IR_1 and FT-IR_2 were cut from. The figure shows the lifetime of FT-IR_1 and FT-IR_2 being 30 µs – 40 µs and +200 µs, respectively.

The results from the FT-IR spectroscopy can be seen in Figure 4.12, as the absorbance spectra of the three samples. The main plot in Figure 4.12 shows the measured spectra, and the highlighted plot shows one region of interest between 400 cm^{-1} and 1000 cm^{-1}, which is related to the Al-O stretching vibrations [82]. The differences in the Al-O peak between the three samples do not correlate with the surface passivation quality in any distinct way, indicating that

it is not the Al-O bonding environment being the dominating factor for the passivation quality in this case. The peaks are comparable, which is expected as the samples received the same temperature treatment both during deposition and post deposition annealing, which is to a large extent detrimental to the bonding environment and crystal structure of the film [83].

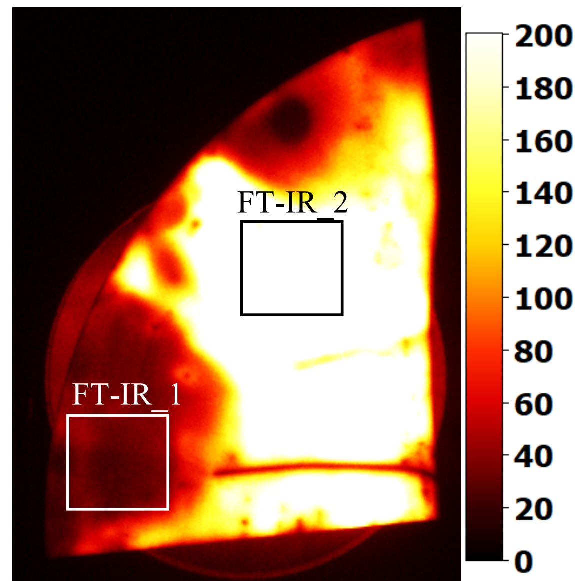

Figure 4.11: This figure shows approximately where FT-IR_1 and FT-IR_2 was cut out from the main sample.

The 1200 cm^{-1} to 2000 cm^{-1} region represents the specter of C-O vibrations, which stems from double bonded CO molecules and CO_2 stretching. These vibrational modes should, if present, give peaks at 1480 cm^{-1}, 1550 cm^{-1} and 1600 cm^{-1}, making them difficult to distinguish as a result of their spacing [84]. From the data it is challenging to differentiate the samples in the region, and could be indicative of similar vibrational behavior in the CO-region, however, the signal-to-noise ratio in this region is too low to. The noise in this region are very distinct, most likely originating from the atmosphere in the measurement setup.

From 2500 cm^{-1} to 4000 cm^{-1} represents the Al-H and O-H stretching modes in the material. A peak in this region should be very broad compared to peaks in the other regions, which originates from the sum of the large polarity of all the O-H bonds affecting the other O-H bonds in their close proximity. This effect creates a tail towards the lower wavenumbers and is more prominent in FT-IR_1 than in the other two samples, which is indicative of a higher hydrogen content in that particular sample than in the other two, as hydrogen most often manifests itself in AlO_x films as OH-groups [82]. Within the broad OH peak of the spectra there is also a contribution from the C-H stretching vibrations, at approximately 2950 cm^{-1}, for which the amplitude is similar for all three samples. However, the results from this region is of

low confidence as the measurement setup have lower sensitivity here, so the readings from 3500 cm^{-1} are not reliable.

The rise in absorbance for FT-IR_1 from 2500 cm^{-1} is most likely explained by a combination of fluctuations in the spectrometer ambient and the measurements of the thin films, which naturally leads to a lower absorbance. Similar measurements are usually performed on thicker films, from 50 nm and up towards several hundred nanometers, which probably would lead to better readings [82], [85]. Longer measurement times, i.e. the average of more measurements would also provide higher signal-to-noise ratio.

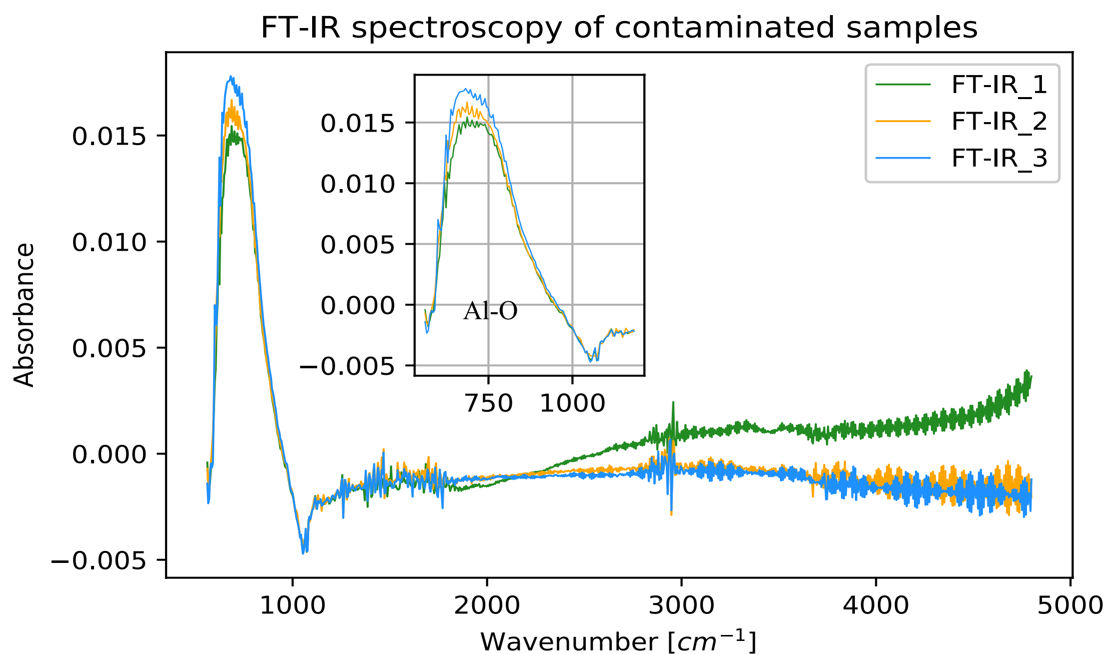

Figure 4.12: FT-IR absorbance spectra for three samples, two of the samples being made from a single process quarter wafer at different locations with varying effective lifetime. The small plot highlights one region of interest, where the peak of the Al-O stretch. The figure indicates some variations in the Al-O bonding environment, although no particular correlation between this and lifetime is found.

From these observations no clear correlation between the different contributions to the absorbance spectra and the passivation quality could be found. No anomalies in the absorbance spectra was seen in this experiment, the only peak were the Al-O stretch and information on the C- or H- bonding were not acquired, hence the contaminant causing the drop in surface passivation is still not determined.

4.2.3 Cleaning Procedure and the Effects on Passivation Quality

In order to address the cross contamination, the reactor went through a cleaning protocol. This includes etching of stainless-steel components, sand blowing of other reactor parts and a chamber passivation of 1000 cycles of ALD Al_2O_3 at 200°C. The etchant used were 10% HCl and the sand blowing particles were SiO_2. All parts where rinsed in isopropanol and DI-water after the cleaning procedure prior to re-mounting them.

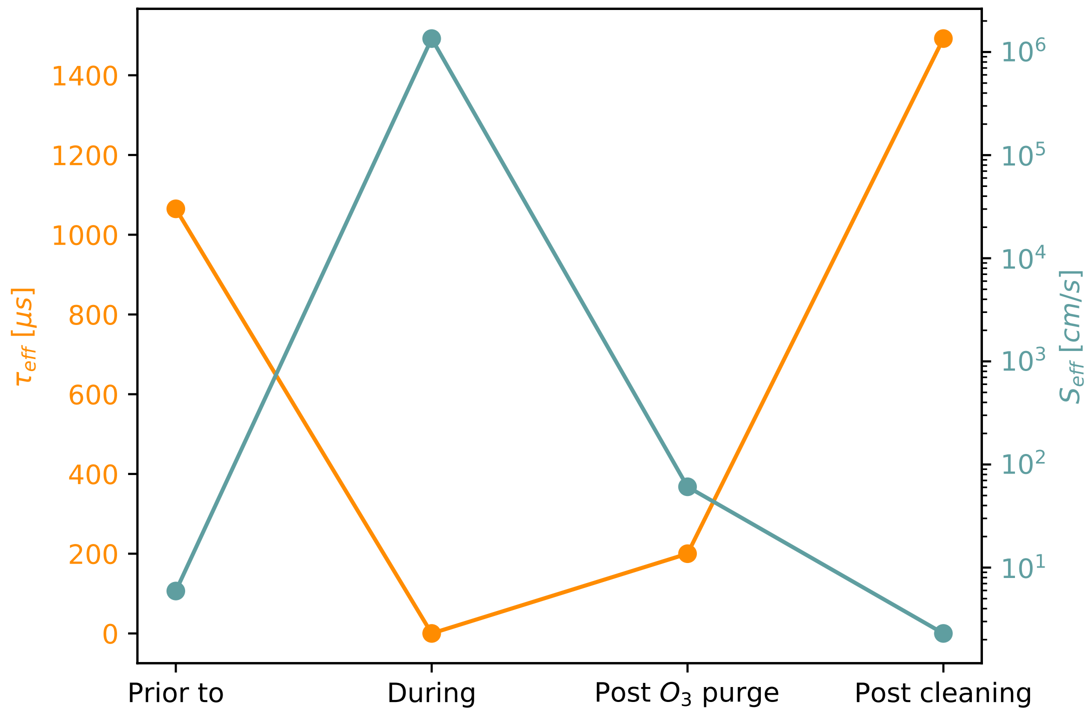

Figure 4.13: Plot of the achieved effective lifetime of samples processed prior to contamination, during the contaminated state, after the O_3-purge and directly after the cleaning process. The plot shows that the surface passivation is back at the same level as before the contamination.

A plot of the τ_{eff} measured on samples prior to, during contamination and after the cleaning procedure is shown in Figure 4.13. From this plot it becomes clear that the reactor cleaning has had a significant effect on the surface passivation quality compared to the contaminated state. In addition, the cleaning seems to have improved the passivation quality compared to the "clean" state prior to the contamination as well. When we compared the effective lifetime of the samples "Prior to" and "Post cleaning", it increased by 40%. This indicates that the trace amounts of materials in the reactor from earlier work which most likely were introduced into the thin films, have now been removed from the system. The differences in lifetime before and after the cleaning is a strong example on the impact of impurities on the passivation quality of a film, and ultimately on the efficiency of the solar cell.

4.3 Characterization of MIS-structures – Determining Q_f

Electrical characterization of MIS-structures is known to provide useful information about passivating films, with regards to the different contributions from the chemical and field effect passivation. In this section, electrical characterization of the films, in the form of CV and PL-V, will be presented.

4.3.1 CV measurements

CV measurements can be used to determine the fixed charge density, Q_f, in a dielectric film, as described in Section 3.3.2. This in turn helps separate the contributions from the chemical and field effect parts of the passivation. The parameters used for these measurements are provided in Table 9. Some of the measurements were performed on different sized electrical pads, because of the high leakage currents through the MIS structure in some pads, so the measured capacitance is normalized in accordance with the pad area.

Table 9: Parameter list for CV-measurements. *4 V for 07_2.

Parameter	Value
Pre-soak Voltage	3 V*
DC Sweep Start / Stop	3 V* / -2 V
Sweep Step	$\pm$0.2 V (2-way sweep)
AC probing Amplitude/Frequency	30mV / 100kHz

A plot of the normalized signals can be seen in Figure 4.14 for samples with 20 nm AlO_x layers deposited on p-type Si with approximately 200 nm thick Ag electrodes deposited using thermal evaporation. The opaque vertical lines represent the calculated V_{fb} for each sample used to calculate the shift from the ideal V_{fb}, which in turn is used to determine Q_f as this shift reflects the number of charges present at the AlO_x/Si-interface. It should be noted that the metal semiconductor work function difference arising from the use of Ag contacts accounts for 0.33 V of the observed shift in V_{fb}. From the figure, one can see a clear shift towards a

positive voltage, indicating some concentration of *negative* charges present in the dielectric, which was previously reported the literature [26], [33], [35], [36].

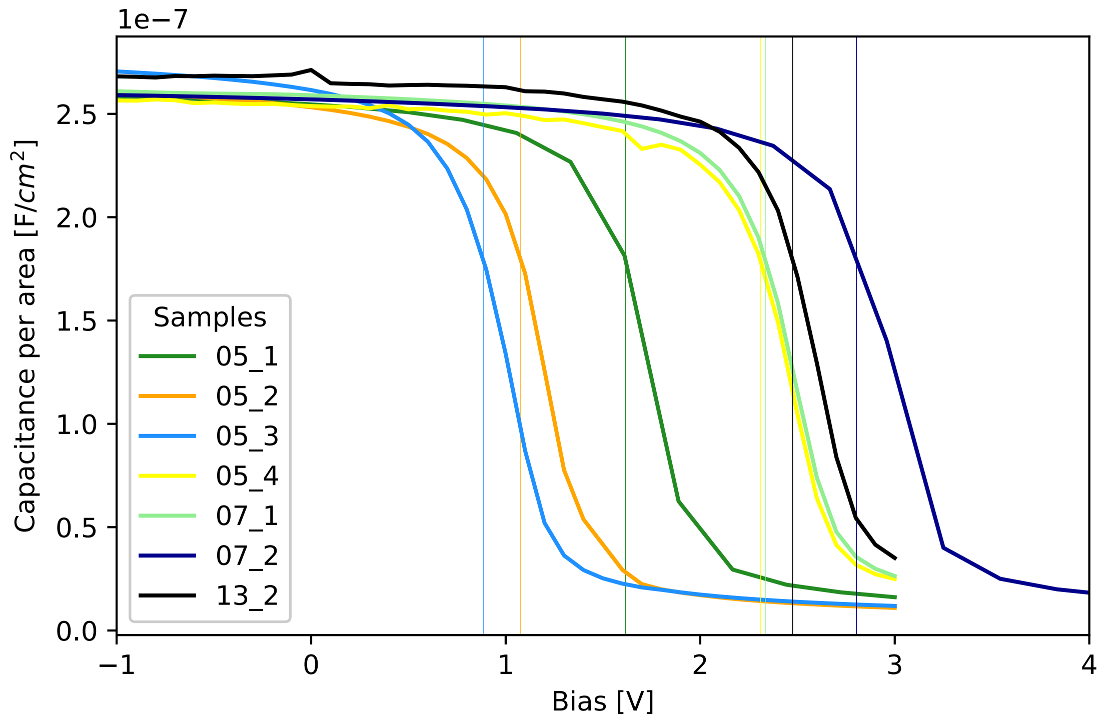

Figure 4.14: Plots of the normalized CV measurments, normalized with pad area, performed on varuios samples with AlOx-films deposited at different temperatures. Vertical lines indicate the flatband voltage for each sample.

Table 10: Calculated τ_{eff}, Q_f-values for samples prepared with different deposition temperatures.

Sample	Deposition Temp. [C]	τ_{eff} [μs]	-Q_f [cm^{-2}]
13_2	50	1270	$3.2148 \cdot 10^{12}$
07_2	100	1888	$3.6173 \cdot 10^{12}$
07_1	150	1492	$3.1858 \cdot 10^{12}$
05_1	200	1065	$1.6910 \cdot 10^{12}$
05_2	250	145.6	$8.2232 \cdot 10^{11}$
05_3	300	11.5	$5.2453 \cdot 10^{11}$
05_4	350	2.6	$2.7949 \cdot 10^{12}$

The calculated concentration of Q_f for the measured samples can be found in Table 10, together with their respective deposition temperature and τ_{eff}-value, which are plotted in Figure 4.15 (a) and (b), respectively. Q_f follows a similar behavior, with regards to deposition temperature, as the SRV reported Section 4.1.2.3, that is, it peaks at 100°C, then falls towards both higher and lover temperatures. This is somewhat expected since a higher Q_f leads to a higher field effect passivation, which leads to higher lifetime. The data indicates an almost linear correlation between lifetime and Q_f, as can be seen in Figure 4.15 (b), where the green line is a linear curve fit of the data. Note that the data from FZ_05_4 is removed from this figure as to create a better fit. One could argue that the result for this sample is not reliable as the deposition temperature is outside the ALD window, which might lead to large variations in all aspects of the film quality. Although it is difficult to conclude that this result is an anomaly, as more samples should have been characterized. However, it is fascinating that a film with so low lifetime contains such a high level of fixed charges, however other mechanisms, such as high concentration of interface states, i.e. bad chemical passivation, or low bulk lifetime, might play a larger role in this particular sample.

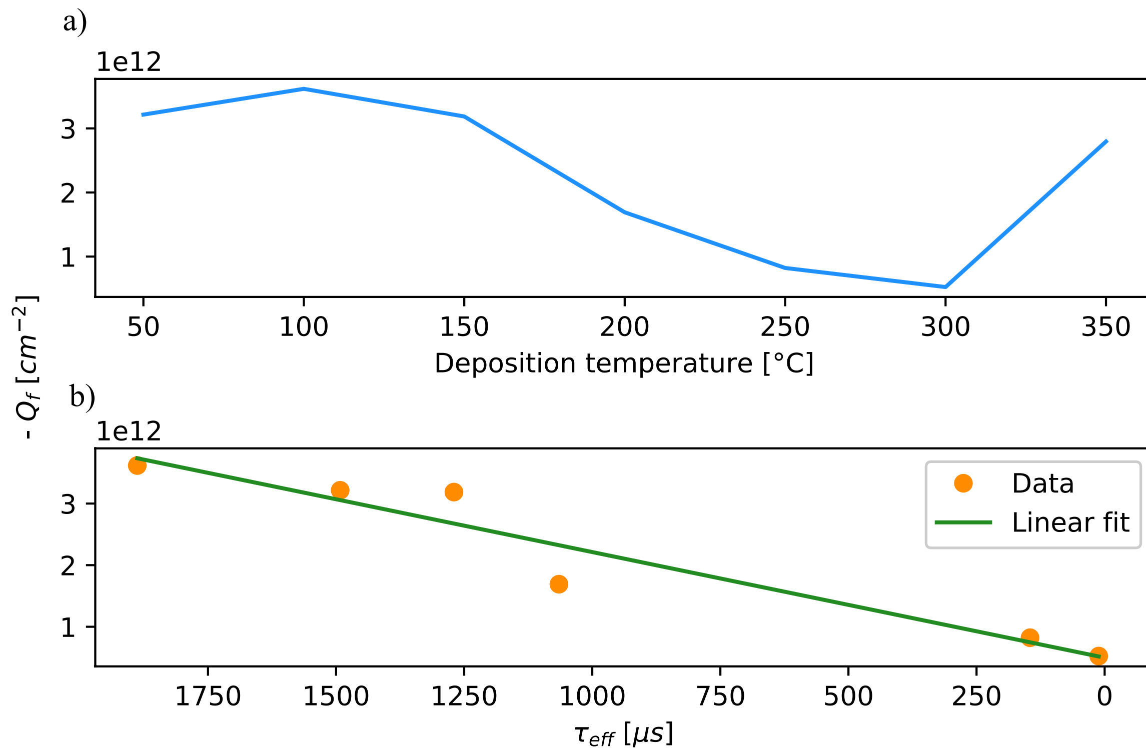

Figure 4.15: The plot in a) shows the correlation between Q_f and deposition temperature, and b) shows the correlation between Q_f and τ_{eff}. Fitting parameters: a = $-1.714 \cdot 10^9$, b = $4.981 \cdot 10^{11}$. FZ_05_4 has been removed from the dataset in b) to make a better fit.

FZ_07_2 had a $Q_f = 4.0238 \cdot 10^{12}$ cm^{-2}, which is comparable to the Q_f reported in the mentioned literature [26], [33], [35], [36]. This indicates the potential of the process established in this work, although more work is needed to improve the reproducibility.

4.3.2 PL-V

The PL-V measurement was performed in accordance with Section 3.3.5 and have been analysed using the Girisch model as described in Section 3.3.5.1. The results of the measurement and analysis for sample 07_2 can be seen in Figure 4.16 together with the fitting parameters and calculated values. PL-V measurements of the other samples were regrettably hindered by excessive leakage currents. The electrode size needed for PL-V measurements are much larger than those used for C-V, hence the chance of pinholes influencing the measurements is much larger. The figure shows the low-point in τ_{eff} at ~2 V, indicating a slightly different flatband voltage compared to the CV-measurements. This discrepancy of approximately 0.5 V – 0.6 V could be attributed to leakage currents in either of the measurements, or bad/different contacting, resulting in varying contact resistance. The lower flat band voltage inherently leads to a lower calculated Q_f. However, at $-3.617 \cdot 10^{12}$ cm^2

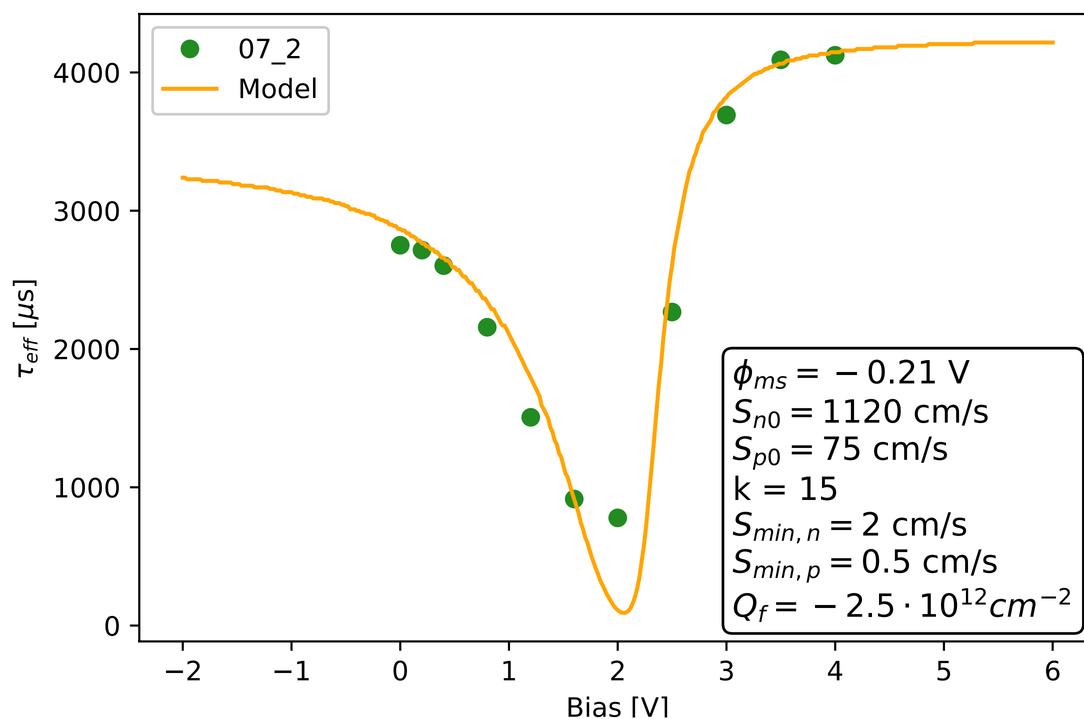

Figure 4.16: This graph shows how τ_{eff} changes with the applied bias. A clear low-point can be found at ~2 V, which is the flat band voltage. Fitting parameters for the model are also provided. K is the ratio between S_{n0} and S_{p0}.

and $-2.5 \cdot 10^{12}$ cm^2, for the CV and PL-V methods, respectively, they are highly comparable, which supports the passivation characteristics for this sample.

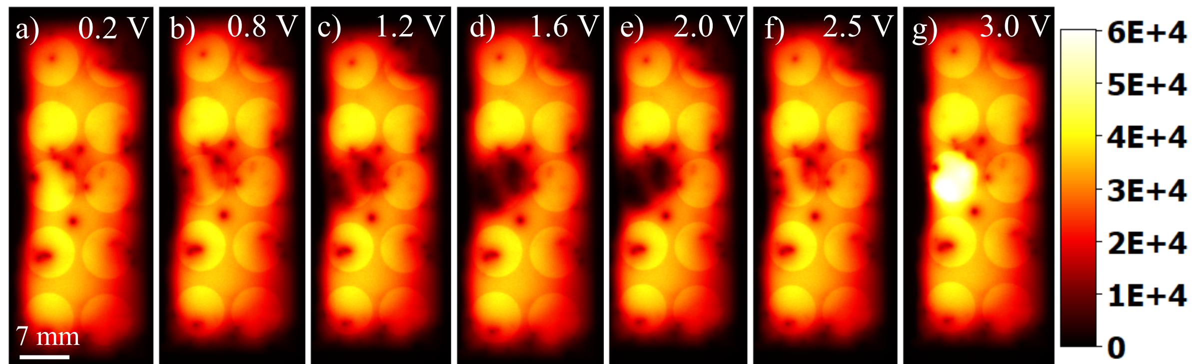

Figure 4.17: PL-V images showing the effects on the biased pad. The "stretching" of the black spots indicate some leakage current. The scale represents the PL intensity as number of counts.

Figure 4.17 (a)-(g) shows the effects of varying bias on the PL images used for the data presented in Figure 4.16. It shows how the electrical pads on the backside of the sample enhancing the PL signal as discussed in Section 3.3.5, which is also taken into account as specified in [68]. In Figure 4.17 (c) – (e) one can see the dark area expanding beyond the contact pad, which might be due to leakage currents across the surface dielectric. As some of the other samples not shown here showed signs of some Ag deposition over a larger area than the actual pad. This could lead to a buildup of Q_g outside of the pad as well, which will either enhance or reduce the field-effect passivation depending on the polarity. As we can see in the figure, the charges induced in the electrode counteracts the negative Q_f concentration in the oxide, then cancel them out at the flatband voltage (depletion) and as the voltage is increased further, the surface is driven into accumulation, where the field-effect is enhanced.

4.4 AlO_x as a Tunneling Oxide Material

As was mentioned in Section 2.4.3, AlO_x can be used as a passivation layer both in the TOPCon cell structure and in the interface between the base and the emitter of a heterjunction solar cell. The reported thickness of this passivation layer is between 1.2 nm and 1.4 nm [7]. Results from simulations of oxide thickness in a MIS contact-structure (TOPCon) is presented together with some IV measurements of a PEDOT:PSS / AlO_x / n-type silicon solar cell structure using different interface passivation layer thicknesses.

4.4.1 Simulations of I-V characteristic of MIS-structures

The MIS structure utilizing a tunneling oxide where performed in the technology computer aided design (TCAD) software Silvaco Atlas, using Deckbuild to generate the structure file. The code is provided in Appendix B. The simulation is based upon the "quantumex10.in Tunneling in a Silicon Diode"-example from the Silvaco homepage (accessed nov. 2019), which was changed to fit the scope of this simulation. The simulation utilizes the Drift-Diffusion model to calculate the charge transport in the bulk of the structure, and the Fowler-Nordheim model to calculate the transport by quantum tunneling. The calculation mesh is shown as green lines and the point at which they intersect in Figure 4.18, where a) is the entire structure and b) is a focus of the oxide region. The mesh in b) is defined by using a QTREGION statement, which takes quantum effects into consideration. The current transport relevant for this work is in the y-direction, hence the numerous calculation points and the few points is the x-direction. The materials used for this model is p-type Si with ~10^{15} doping concentration,

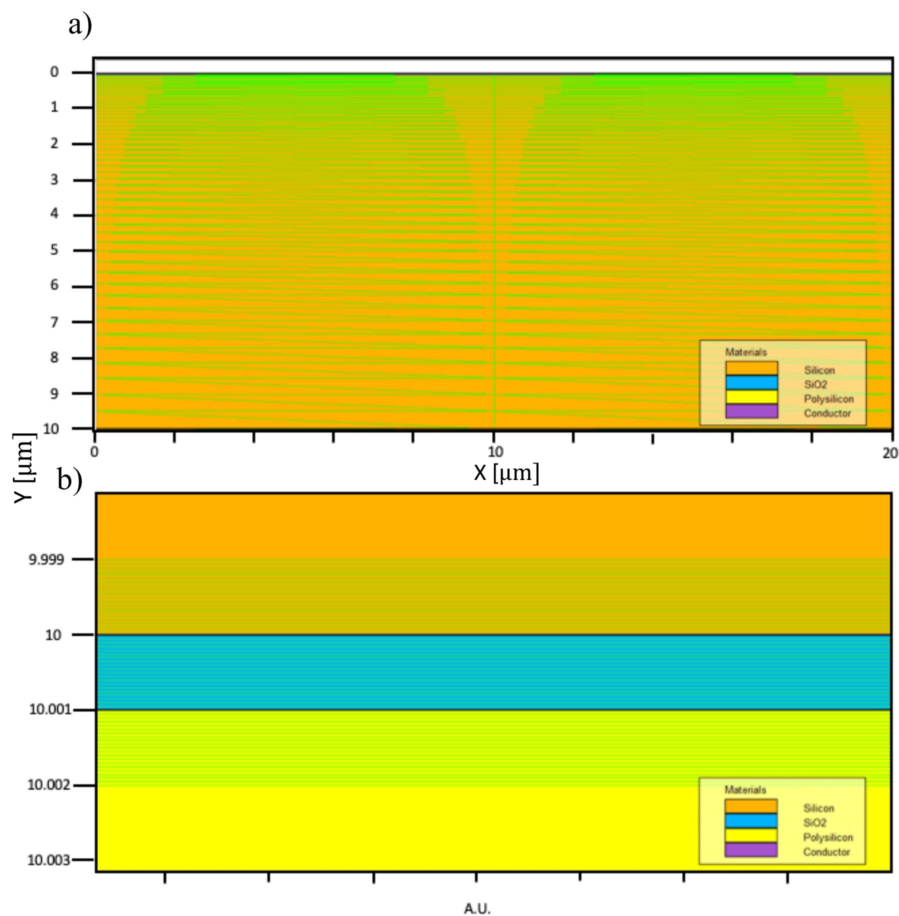

Figure 4.18: Plot of the structure file used in the Atlas MIS simulations.

SiO_2 as the oxide and heavily doped n-type poly-Si with ~10^{19} dopants per cm^{-3} and then standard contacts at each side of the structure.

The results of a simulated voltage sweep from 0 V to 2 V of the structure with varying oxide thicknesses is shown in Figure 4.19. The plots show a clear threshold voltage for current transport, which increases with increasing oxide thickness. This seems reasonable; as the potential barrier becomes wider, the amplitude of the wavefunction on the far side will be lower, hence the applied voltage must be higher to obtain the same current. The current-voltage relationship after the threshold voltage is fairly linear, indicating that a good ohmic contact is made to the outside electrodes, although not perfect.

As one might notice, the currents through the structure are very small. When compared to other work, like Mudanai et al. [86] where they simulated similar structures, the current at 1 V for a 1 nm thick SiO_2 was ~ $5 \cdot 10^2$ A/cm^2. This indicates that the model used in this work does not describe the physics sufficiently. In addition, it is well known that oxide thicknesses in excess of 1 nm can be used in solar cell applications, which operates at voltages below 1 V.

Either way, a clear correlation between the oxide thickness and the threshold voltage is obtained from these simulations.

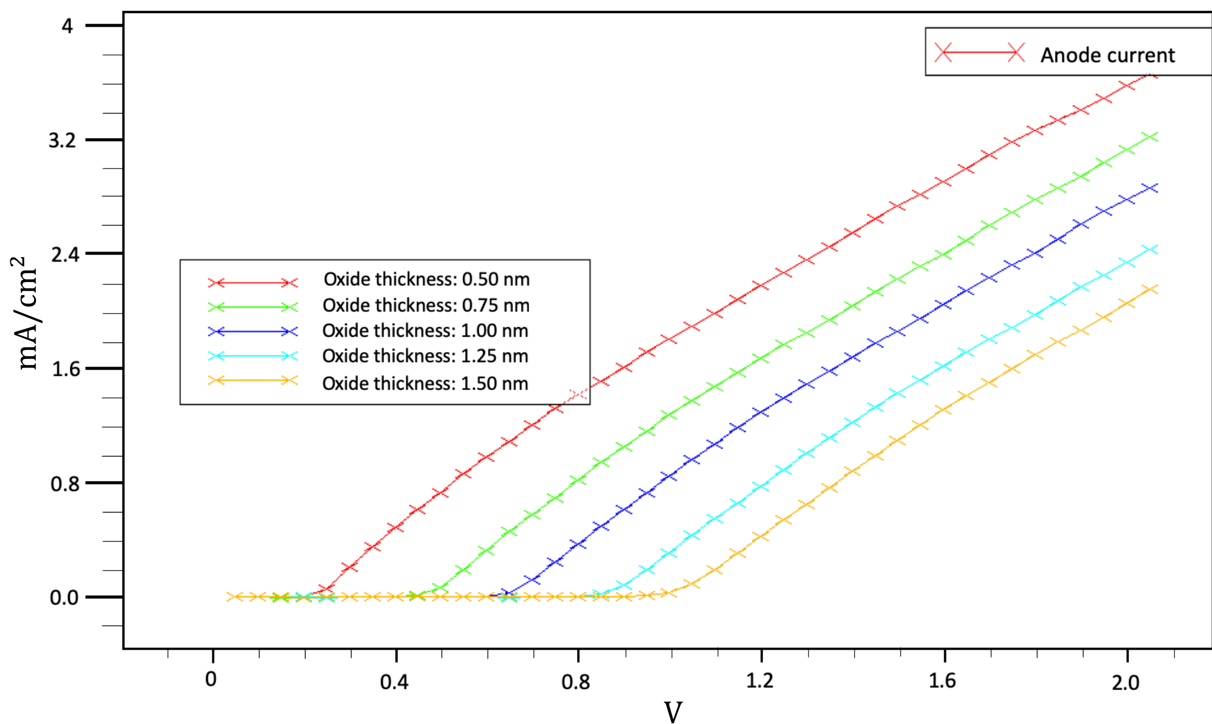

Figure 4.19: Silvaco simulation results of the MIS structure.

4.4.2 I-V measurements of PEDOT:PSS / AlO_x / Si solar cells

A small collaboration project investigating the properties of utilizing a AlO_x interface passivation layer in a heterojunction PEDOT:PSS / Si hybrid solar cell were performed. Varying thicknesses of AlO_x was deposited on n-type Si substrates using ALD, then, a 120 nm thick PEDOT:PSS layer was spin coated on top, and then electrodes (Front: Au+Ag, back: Ag) where deposited on both sides using a thermal evaporator. Erlend Hall performed the spin coating, the electrode deposition and the electrical measurements. The goal for this work was to investigate how oxide thickness affected the current through the solar cell. The attempted oxide thicknesses vs the actual thickness was 0.5 nm / 1.3 nm, 1.0 nm / 1.7 nm, 1.5 nm / 2.1 nm and 2.0 nm / 2.6 nm. It is difficult to explain the large variance in expected vs actual thickness. One could be that a native oxide is formed rather quickly when the samples are exposed to air. This hypothesis is supported by the consistency of the thickness deviation, which is between 0.6 nm and 0.8 nm. The thickness deviation on these samples seems much larger than previous samples, as the percentage error is on the 0.5 nm sample above 100%. This might not be the case, even as all samples processed in this work have some varying excess thickness compared to the expected, the percentage difference becomes much more prominent on films in the 0.5 nm to 2 nm range.

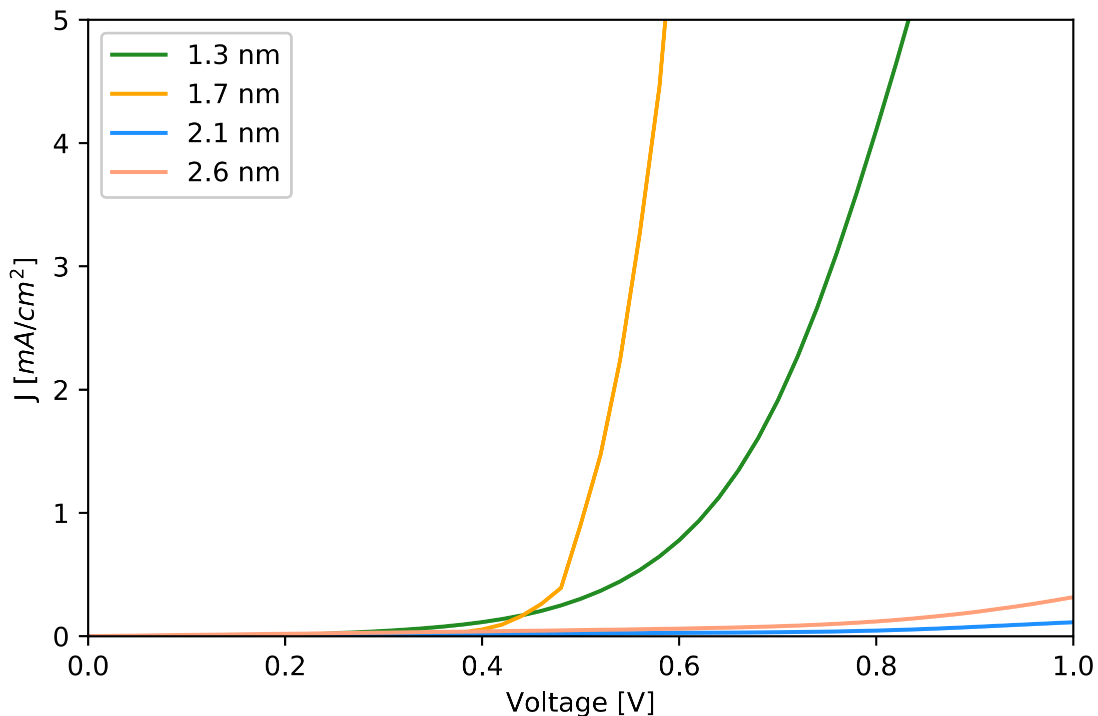

Figure 4.20: IV-characteristics of hybrid solar cells in the dark with varying oxide thickness.

The IV data acquired in the dark are shown in Figure 4.20. Samples 1.3 nm and 1.7 nm shows promising characteristics, with decent diode performance, although fairly low threshold voltage, which would lead to a low FF. The two other samples however, are non-responding with in the measured voltage range, that is, the current does not increase remarkably compared to the other two samples. This could be a result of different sample handling or varying deposition quality for the oxide or the PEDOT:PSS layers, but could also mean that the threshold voltage is beyond 1 V, which either way means that these thicknesses is unsuitable for solar cell applications as the voltage across the pn-junction is lower than this. The results seem promising for the development of hybrid cell using PEDOT:PSS layers, however more experiments are needed.

5 Conclusion and Further Work

In this final chapter, the work done in this thesis will be summaries and concluded. In addition, some suggestions for improvements and further work is also presented.

5.1 Conclusion

ALD Al2O3 is a well-known passivation layer for crystalline Si solar cells, and is considered the state-of-the-art for industrial cell production. However, no established process has so far been developed for this material at IFE and UiO. In this work, a surface passivation focused ALD Al_2O_3 process at MiNaLab have been developed and characterized, giving excellent passivation quality with SRV values below 0.5 cm/s shown to be within reach. Characterization of the passivation quality have been done through QSSPC and PLI, and the oxide charge concentration have been determined through CV measurements and analysis at flat band conditions. Concentrations of negative charges in the highest quality films are in the same range as the literature from $-5.245 \cdot 10^{11}\ cm^{-2}$ to -3.617 $\cdot\ 10^{12}\ cm^{-2}$. The PL-V method has also been utilized to determine the charge concentration, as well as the S_{n0} and S_{p0} parameters.

Investigation of impurities or defects in the films created by cross contamination in the chamber using SIMS and FTIR did not reveal large impurity concentrations introduced in the contaminated samples, which indicates a defect concentration below ppm levels.

AlO_x as an ultra-thin tunneling oxide have been simulated through a MIS structure with the Silvaco Atlas program. The simulations revealed a correlation between the oxide thickness and the threshold voltage, although only a small current was found at standard solar cell operating voltages between 0.5 V and 1 V. The threshold voltage increased with increasing oxide thickness.

AlO_x interface passivation layers have also been characterized using the hybrid PEDOT:PSS / Si heterojunction solar cell structure. The IV characteristic of solar cells was measured, where some of the samples showed promising results.

5.2 Further Work

Although many of the findings in the work is backed up by a substantial amount of research, some are of anecdotal nature and will require more experiments for verification. Among them are the optimum deposition temperature for ALD AlO_x in the reactor at MiNaLab. The highest surface passivation potential shown in this work was at 100 °C, which is different from that normally reported in the literature. One sample showed SRV as low 0.4 cm/s, however this work was not able to reproduce this result, thus it is necessary to do more experiments.

The research performed to obtain an optimized annealing temperature was performed at samples where the deposition temperature was 200 °C. This do not imply that the optimal annealing temperature for samples with films deposited at 100 °C are the same. More experiments are needed to verify this.

A drawback with the PL-V method is the need for deposited electrodes. Some work into producing a less invasive, but as efficient way of applying surface potential controllably could be performed. Liquid metal contacts might be a feasible candidate. Furthermore, many of the attempted PL-V measurements were hindered by leakage currents. In further experiments, thicker AlOx layers or capping layers could be produced in order to mitigate this issue.

Hopefully, the potential shown in this work will lead to more research into ALD AlO_x as surface and interface passivation. For the PERC solar cell based on Si, this material is already known to provide good interface passivation characteristics, but for the coming generation of tandem solar cells and passivated contacts, ALD AlO_x should certainly be among the candidates for further exploration.

6 Bibliography

[1] A. McCrone, U. Moslener, F. s'Estais and C. Grüning, “Global Trends in Renewable Energy Investment 2018,” FS-UNEP Collaborating Centre, Frankfurt am Main, 2018.

[2] International Energy Agency, “International Technology Roadmap for Photovoltaic (ITRPV),” 2018.

[3] S. W. Glunz and F. Feldmann, “SiO2 Surface Passivation Layers - a key technology for silicon solar cells,” *Solar Energy Materials and Solar Cells,* vol. 185, pp. 260-269, 2018.

[4] J. Meleskens, B. W. H. V. d. Loo, B. Macco, L. E. Black, S. Smit and W. M. M. Kessels, “Passivating contacts for crystalline solar cells: from concepts and materials to prospects,” *IEEE Journal of Photovoltaics,* vol. 8, pp. 373-388, 2018.

[5] P. Saint-Cast, J. Benick, D. Kaina, L. Weiss, M. Hofmann, J. Rentsch, R. Preu and S. W. Glunz, “High-Efficiency c-Si Solar Cells Passivated with ALD and PECVD Aluminum Oxide,” *IEEE Electron Device Letters,* vol. 31, no. 7, pp. 695-697, 201.

[6] D. Zielke, J. H. Petermann, F. Werner, B. Veith, R. Brendel and J. Schmidt, “Contact passivation in silicon solar cells using atomic-layer-deposited aluminun oxide layers,” *Rapid research letters,* vol. 5, no. 8, pp. 298-300, 2011.

[7] J. Benick, A. Richter, R. Müller, H. Hauser, F. Feldmann, P. Krenckel, S. Riepe, F. Schindler, M. C. Schubert, M. Hermle, A. W. Bett and S. W. Glunz, “High-Efficiency n-Type HP mc Silicon Solar Cells,” *IEEE Journal of Photovoltaics,* vol. 7, no. 5, pp. 1171-1175, 2017.

[8] B. G. Streetman and S. K. Banerjee, “Metals, Semiconductors, and Insulators,” in *Solid State Electronic Devices*, Austin, Pearson Education Limited, 2016, pp. 89-90.

[9] A. Smets, K. Jäger, O. Isabella, R. van Swaaij and M. Zeman, “12.4 Fabricating c-Si solar cells,” in *Solar Energy*, Cambridge, UIT Cambridge Ltd, 2016, pp. 166-169.

[10] J. Nelson, "3.3.4. Direct and indirect band gaps," in *The physics of solar cells*, London, Imperial College Press, 2003, pp. 50-51.

[11] J. E. Brady, "7.4 Electron spinn and the Pauli principle," in *General Chemistry: Principles and Structures*, New York, Wiley, 1978, pp. 190-191.

[12] R. J. D. Tilley, "2.3.1 Molecular orbitals and energy bands," in *Understanding Solids: The scinence of materials 2nd ed.*, Chichester, Wiley, 2013, pp. 36-37.

[13] W. Shockley and W. T. Read Jr., "Statistics of the Recombination of Holes and Electrons," *Physical Review,* vol. 87, no. 5, pp. 835-842, 1952.

[14] A. R. Peaker, V. P. Markevich, B. Hamilton, G. Parada, A. Dudas, A. Rap, E. Don, B. Lim, J. Schmidt, L. Yu, Y. Yoon and G. Rozgonyl, "Recombination via point defects and their complexes in solar silicon," *Physica Status Solidi A,* vol. 209, no. 10, pp. 1884-1893, 2012.

[15] Seimconductor Equipment and materials International, "International Technology Roadmap for Photovoltaic (ITRPV) - Results 2012," 2012.

[16] A. G. Aberle, S. Glunz and W. Warta, "Impact of illumination level and oxide parameters on Schokley-Read-Hall recombination at the Si-SiO2 interface," *Journal of applied Physics,* vol. 71, no. 9, pp. 4422-4431, 1992.

[17] A. G. Aberle, Crystalline Silicon Solar Cells: Advanced Surface Passivation and Analysis, Sydney: University of New South Wales, 2004.

[18] M. J. Kerr and A. Cuevas, "Very low bulk and surface recombination in oxidized silicon," *Semiconductor Science and Technology,* vol. 17, no. 1, pp. 35-38, 2001.

[19] T. Mishima, M. Taguchi, H. Sakata and E. Maruyama, "Development status of high efficiency HIT solar cells," *Solar Energy Materials and Solar Cells,* vol. 95, pp. 18-21, 2011.

[20] Masuko et al., "Achievement of more than 25% Conversion Efficiency with Crystalline Silicon Heterojunction Solar Cell," *IEEE Journal of Photovoltaics,* vol. 4, no. 6, pp. 1433-1435, 2014.

[21] Y. Wan, K. R. McIntosh and A. F. Thomson, "Characterisation and optimisation of PECVD SiNx as an antireflection coating and passivation layer for silicon solar cells," *AIP Advances,* vol. 3, no. 3, pp. 0321131-03211314, 2013.

[22] M. Z. Rahman and S. I. Khan, "Advances in surface passivation of c-Si solar cells," *Materials for Renewable and Sustainable Energy,* vol. 1, no. 1, pp. 1-11, 2012.

[23] G. Dingemans, F. Einsele, W. Beyer, M. C. M. van de Sanden and W. M. M. Kessels, "Influence of annealing and Al2O3 properties on the hydrogen-induced passivation of the Si/SiO2 interface," *Journal of Applied Physics,* vol. 111, no. 9, p. 093713(9), 2012.

[24] G. Dingemans, M. C. M. van de Sanden and W. M. M. Kessels, "Excellent Si surface passivation by low temperature SiO2 using an ultrathin Al2O3 capping film," *PSS rapid research letters,* vol. 5, no. 1, pp. 22-24, 2011.

[25] G. Dingemans, C. A. A. van Helvoirt, D. Pierreux, W. Keuning and W. M. M. Kessels, "Plasma-Assisted ALD for the Conformal Deposition of SiO2: Process, Material and Electrical Properties," *Journal of the Electrochemical Society,* vol. 59, no. 5, pp. H277-H285, 2012.

[26] D. K. Simon, P. M. Jordan, I. Dirnstorfer, F. Benner, C. Richter and T. Mikolajick, "Symetrical Al2O3-based passivation layers for p- and n-type silicon," *Solar Energy Materials & Solar Cells,* vol. 131, pp. 72-76, 2014.

[27] R. S. Bonilla, B. Hoex, P. Hamer and P. R. Wilshaw, "Dielectric surface passivation for silicon solar cells: A review," *Physica Status Solidi a,* vol. 214, no. 7, p. 1700293, 2017.

[28] F. Kresten, A. Schmid, S. Borihn, M. J. W. and J. Heitmann, "Role of annealing conditions on surface passivation properties of ALD Al2O3 films," *Energy Preocedia,* vol. 38, pp. 843-848, 2013.

[29] H. Haug, B. Yameng, H. Savin and E. S. Marstein, “Investigation of Al2O3 Passivation layers by photoluminescence imaging under applied voltage,” in *32nd European Photovoltaic Solar Energy Conference and Exhibition*, Munich, 2016.

[30] P. Saint-Cast, J. Benick, D. W. L. Kaina, M. Hofmann, J. Rentsch, R. Preu and W. S. Glunz, “High-Efficiency c-Si Solar Cells Passivated with ALD and PECVD Aluminum Oxide,” *IEEE Electron Device Letters,* vol. 31, no. 7, pp. 695-697, 2010.

[31] L. E. Black and K. R. McIntosh, “Surface passivation of c-Si by atmospheric pressure chemical vapor deposition of Al2O3,” *Applied Physics Letters,* vol. 100, no. 20, pp. 202105-202107, 2012.

[32] T. T. Li and A. Cuevas, “Effective surface passivation of crystalline silicon by RF sputtered aluminum oxide,” *Physica Status Solidi - Rapid Research Letters,* vol. 3, no. 5, pp. 160-162, 2009.

[33] D. K. Simon, P. M. Jordan, T. Mikolajick and I. Dirnstorfer, “On the Control of the Fixed Charge Densities in Al2O3-Based Silicon surface Passivation Schemes,” *ACS Applied Materials and Interfaces,* vol. 7, no. 51, pp. 28215-28222, 2015.

[34] N. M. Terlinden, G. Dingemans, M. C. M. van de Sanden and W. M. M. Kessels, “Role of field-effect on c-Si surface passivation by ultrathhin (2-20 nm) atimoc layer deposited Al2O3,” *Applied Physics Letters,* vol. 96, no. 11, pp. 112101-112103, 2010.

[35] G. Dingemans and W. M. M. Kessels, “Status and prostects of Al2O3-based passivation schemes for silicon solar cells,” *Journal of Vacuum Science & Technology A,* vol. 30, no. 4, pp. 040801-0408027, 2012.

[36] G. Dingemans, N. M. Terlinden, M. A. Verheijen and M. C. M. van de Sanden, “Controlling the fixed charge and passivation properties of Si(100)/Al2O3 interfaces using ultrathin SiO2 interlayers synthesized by atomic layer deposition,” *Journal of Applied Physics,* vol. 110, no. 9, pp. 093715-6, 2011.

[37] N. C. Kluksdahl, A. M. Kriman and D. K. Ferry, “Self-consistent study of the resosnant-tunneling diode,” *Physical Review B,* vol. 39, no. 11, pp. 7720-7735, 1989.

[38] Müller et al., “Loss analysis of 22% efficient industrial PERC solar cells,” *Energy Procedia,* vol. 124, pp. 131-137, 2017.

[39] X. Gu, X. Yu and D. Yang, “Efficiency improvement of crystalline silicon solar cells with a back-surface field produced by boron and aluminum co-doping,” *Scripta Materialia,* vol. 66, no. 6, pp. 394-397, 2012.

[40] Forster et al., “Impact of compensation on th eboron and oxygen-related degradation of upgraded metallurgical-grade silicon solar cells,” *Solar Enrgy Materials and Solar Cells,* vol. 120, no. Part A, pp. 390-395, 2014.

[41] A. Rehman and S. H. Lee, “Advancements in n-type base crystalline silicon solar cells and their emergence in the photovoltaic indusrty,” *The Scientific World Journal,* vol. 2013, pp. 1-13, 2013.

[42] F. Feldmann, M. Bivour, C. Reichel, M. Hermle and G. S. W., “A PASSIVATED REAR CONTACT FOR HIGH-EFFICIENCY n-TYPE SILICON SOLAR CELLS ENABLING HIGH VocS AND FF>82%,” in *28th European PV solar energy conferencr and exhibition*, Paris, France, 2013.

[43] S. J., R. Singh and M. A. Green, “Theory of metal-insulator.semiconductor solar cells,” *Journal of Applied Physics,* vol. 48, no. 2, pp. 765-770, 1977.

[44] J. Yoo, G. Yu and J. Yi, “LArge-area multicrystalline silicon solar cell fabrication using reactive ion etching (RIE),” *Solar Energy Materials and Solar Cells,* vol. 95, no. 1, pp. 2-6, 2011.

[45] J. P. Thomas and K. T. Leung, “Defect-minimized PEDOT:PSS/Planar.Si Solar Cell with Very High Efficiency,” *Advanced functional materials,* vol. 24, no. 31, pp. 4978-4985, 2014.

[46] K. A. Nagamatsu, S. Avasthi, J. Jhaveri and J. C. Sturm, “A 12% Efficient Silicon/PEDOT:PSS Heterojunction Solar cell Fabricated at < 100C,” *IEEE Journal of Photovoltaics,* vol. 4, no. 1, pp. 260-264, 2014.

[47] S. Jäckle, M. Liebhaber, C. Gersmann, M. Mews, K. Jäger, S. Christiansen and K. Lips, "Potetnial of PEDOT:PSS as a hole selective front contact for silicon heterojunciton solar cells," *Scientific Reports,* vol. 7, p. 2170, 2017.

[48] S. Jäckle et al., "Junction formation and current transport mechanisms in hybrid n-Si/PEDOT:PSS solar cells," *Scientific Reports,* vol. 5, 2015.

[49] P. R. Pudasaini, M. Sharma, F. Ruiz.Zepeda and A. A. Ayon, "Efficiency improvement of a nanostructured polymer solar cell employing atomic layer deposited Al2O3 as a passivation layer," *Microelectronic Engineering,* vol. 119, pp. 6-10, 2014.

[50] García-Tecedor et al., "Silicon surface passivation by PEDOT:PSS functionalized by SnO2 and TiO2 nanoparticles," *Nanotechnology,* vol. 29, no. 3, p. 035401, 2018.

[51] S. M. George, "Atomic Layer Deposition: An Overview," *American Chemical Society,* vol. 110, no. 1, pp. 111-131, 2010.

[52] V. Mikkulainen, M. Leskelä, M. Ritala and R. L. Puurunen, "Crystalinity of inorganic films grown by atomic layer deposition: over view and general trends," *Journal of Applied Physics,* vol. 113, no. 2, pp. 021301-92, 2013.

[53] A. S. Campbell, "Czochralski Growth," in *Fabrication Engeneering at the Micro- and Nanoscale*, New York, Oxford University Press, 2013, pp. 23-31.

[54] R. L. Puurunen, "Surface chemistry of atomic layer deposition: A case study of the trimethylaluminum/water process," *Journal of Applied Physics,* vol. 97, no. 12, pp. 121301-52, 2005.

[55] R. D. Shannon, "Revised Effective Ionic Radii and Systematic Studies of interatomic Distances in Halides and Chalcogenides," *Acta Crystalographica Section A,* vol. 32, pp. 751 - 767, 1976.

[56] M. Putkonen, N. M. and L. Niinistö, "Magnesium aluminate thin films by atomic layer deposition from organometallic precursoes and water," *Thin Solid Films,* vol. 466, no. 1-2, pp. 103 - 107, 2004.

[57] J. M. Jensen, A. B. Oelkers, R. Toivola, D. C. Johnson, J. W. Elam and G. S. M., “X-ray Reflectivity Characterization of ZnO/Al2O3 Multilayers Prepared by Atmic Layer Deposition,” *Chemical Materials,* vol. 14, no. 5, pp. 2276 - 2282, 2002.

[58] I. T. Heikkinen, “Efficient surface passivation of black silicon using spatial atomic layer deposition,” *Progress in Photovoltaics,* vol. 19, no. 6, pp. 733-739, 2011.

[59] B. O'Donnell, “www.pv-magazine.com,” pv magazine, 29 June 2019. [Online]. Available: https://www.pv-magazine.com/2019/06/29/the-weekend-read-atomic-layer-deposition-storms-market-for-perc/. [Accessed 22 March 2020].

[60] M. Morita, T. Ohmi, E. Hasegawa, M. Kawakami and M. Ohwada, “Growth of native oxide on a silicon surface,” *Journal of Applied Physics,* vol. 68, no. 3, pp. 1272-1281, 1990.

[61] M. Morita, T. Ohmi, E. Hasegawa, M. Kawakami and M. Ohwada, “Growth of native oxide on a silicon surface,” *Journal of Applied Physics,* vol. 68, no. 3, pp. 1272 - 1281, 1990.

[62] H. H. Sønsteby, A. Yanguas-Gil and J. W. Elam, “Concistency and reproducibility in atomic layer deposition,” *Journal of Vacuum Science and Technology A,* vol. 38, no. 2, pp. 020804-1-17, 2020.

[63] J. Benick, A. Richter, T.-T. A. Li, K. R. McIntosh, Y. Ren, K. J. Weber, M. Hermle and S. W. Glunz, “Effects of a post-deposition anneal on Al2O3/Si interface properties,” in *2010 35th IEEE Photovoltaic Specialist Conference*, Honolulu, HI, USA, 2010.

[64] Vandana et al., “Effect of low thermal budget annealing on surface passivation of silicon by ALD based aluminum oxide films,” *Physical Chemistry Chemical Physics,* vol. 16, no. 39, pp. 21804-21811, 2014.

[65] S. Bordihn, I. I. Kiesow, V. Mertens, P. Engelhart, J. W. Müller and W. M. M. Kessels, “Impact of the Depositin and Annealing Temperature on the Silicon Surface Passivation of ALD Al2O3 Films,” *Energy Procedia ,* vol. 27, pp. 396-401, 2012.

[66] D. K. Schroder, “Oxide and Interface Trapped Charges, Oxide Thickness,” in *Semiconductor Material and Device Characterization*, Tempe, AZ, John Wiley & Sons, Inc., 2005, pp. 319-387.

[67] H. Haug, Ø. Nordseth, E. V. Monakhov and E. S. Marstein, “Photoluminescence imaging under applied bias for characterization of Si surface passivation layers,” *Solar Energy Materials and Solar Cells,* vol. 106, pp. 60-65, 2012.

[68] H. Haug, S. Olibet, Ø. Nordseth and E. S. Marstein, “Modulating the field-effect passivation at the SiO2/c-Si interface: Analysis and verification of the photoluminescence imaging under applied bias method,” *Journal of Applied Physics,* vol. 114, no. 17, pp. 174502-1 - 174502-10, 2013.

[69] H. Okumura, S. Misawa and S. Yoshida, “Reliability of the band disconuity determination by capacitance-voltage method: Relation of the interface charge density and the trap ceoncentration,” *Surface science,* vol. 174, no. 1, pp. 324-330, 1986.

[70] S. Kühnhold-Posposchil, P. Saint-Cast, A. Richter and M. Hofmann, “Activation energy of negative fixed charges in thermal ALD Al2O3,” *Applied Physics Letters,* vol. 109, no. 6, pp. 061602-1 - 061602-4, 2016.

[71] R. A. Sinton, A. Cuevas and M. Stuckings, “Quasi-Steady-State Photoconductance, A new method for solar cell material and device characterization,” in *25th IEEE Photovoltaic Specialist Conference*, San Jose, CA, USA, 1996.

[72] T. Trupke, J. Nyhus and J. Haunschild, “Limunescence imaging for inline characterization in silicon photovoltaics,” *Physica Status Solidi - Rapid research letters,* vol. 5, no. 4, pp. 131-137, 2011.

[73] R. B. M. Girisch, R. P. Mertens and R. F. De Keersmaecker, “Determination of Si-SiO2 interface recombination parameters using a gate controlled point-junction diode under illumination,” *IEEE Transactions on Electron Devices,* vol. 35, no. 2, pp. 203-222, 1988.

[74] S. W. Glunz, D. Biro, S. Rein and W. Warta, “Field-effect passivation of the SiO2/Si interface,” *Journal of Applied Physics,* vol. 86, no. 1, p. 683, 1999.

[75] N. Batra et al., “Influence of deposition temperature of thermal ALD deposited Al2O3 films on silicon surface passivation,” *AIP Advances,* vol. 5, no. 6, pp. 067113-1 - 067113-10, 2015.

[76] W. M. .. K. G. Dingemans, “Aliuminum Oxide and Other ALD Materials for Si Surface PAssivation,” *Electrochemical Society Transactions,* vol. 41, no. 2, p. 293, 2011.

[77] G. M. D., F. H. Fabreguette, J. W. Elam and G. S. M., “Low-Temperature Al2O3 Atomic Layer Deposition,” *Chemical Materials,* vol. 16, no. 4, pp. 639-645, 2004.

[78] M. Ritala, M. Leskelä, L. Niinistö and P. Haussalo, “Titanium isopropoxide as a precursor in atomic layer epitaxy of titanum dioxide thin films,” *Chemistry of Materials,* vol. 5, no. 8, pp. 1174-1181, 1993.

[79] R. Matero, A. Rahtu, M. Ritala, M. Leskelä and T. Sajavaara, “Effect of water dose on the atomic layer deposition rate of oxide thin flims,” *Thin Solid Films,* vol. 368, no. 1, pp. 1-7, 2000.

[80] A. W. Ott, J. W. Klaus, J. J. M. and S. M. George, “Al2O3 thin film growth on Si(100) using binary reaction sequence chemistry,” *Thin Solid Films,* vol. 292, no. 1-2, pp. 135-144, 1997.

[81] Nishi et al., “Determination of Trace Amounts of Oxygen and Sulfur in Copper by Secondary Ion Mass Spectrometry (SIMS),” *Journal of the Japan Institute of Metals and Materials,* vol. 54, no. 6, pp. 692-699, 1990.

[82] V. Verlaan, L. R. J. G. van den Elzen, G. Dingemans, M. C. M. van den Sanden and W. M. M. Kessels, “Composition and bonding structure of plasma-assisted ALD Al2O3 films,” *Physica Status Solidi C,* vol. 7, no. 3-4, pp. 976-979, 2010.

[83] S. Jakschik, U. Schroeder, M. Gutsche, H. Seidl and J. W. Bartha, “Crystallization behavior of thin ALD-Al2O3 films,” *Thin Solid Films,* vol. 425, pp. 216-220, 2003.

[84] T. O. Käärläinen, D. C. Cameron and M. Tanttari, “Adhesion of Ti and TiC Coatings on PMMA Sunject to Plasma Treamtent: Effect of Intermediate Layers of Al2O3 and TiO2 Deposited By ALD,” *Plasma Processes an Polymers,* vol. 6, pp. 631-641, 2009.

[85] Z. Kataz-Tsameret and A. Raveh, “Characterization of aluminum based oxide layers be microwave plasma,” *Journal of Vacuum Science & Technology A,* vol. 13, no. 3, pp. 1121-1127, 1995.

[86] Sivakumar Mudanai et al., “Modeling of Direct Tunneling Current Through Gate Dielectric stacks,” *IEEE Transactions on Electron Devices,* vol. 47, no. 10, pp. 1851-1857, 2000.

[87] M. J. Kerr, J. Schmidt and A. Cuevas, “Surface recombination velocity of phosphorus-diffused silicon solar cell emitters passivated with plasma enhanced chemical vapor deposited silicon nitride and thermal silicon oxide,” *Journal of Applied Physics,* vol. 89, no. 7, pp. 3821-3825, 2001.

Appendix A – CV-analysis code (python)

```
import matplotlib.pyplot as plt
import numpy as np
import csv

#--------------------------------
figname = ‘<<insert figure name>>’
filenames = [“<<insert file name>>”,“<<insert file name>>”],…]
labellist = [‘<<insert label>>’, ‘<<insert label>>’,…]
colorlist = [‘<<insert color name>>’, ‘<<insert color name>>’,…]

Qf_list = []

fig = plt.figure()                  #creates figure with subplots
ax = fig.add_subplot(111)
j = 0                               #counter
#--------------------------------------
#Define material parameters
p_dop = 5e15
workf_Si = 4.85 #V p-type Si
workf_Ag = 4.26 #V
eps_Si = 11.7 * 8.85e-14 #F/cm
eps_alox = 7.13 * 8.85e-14 #F/cm
aff_Si = 4.05 #eV
T = 300
kT = 8.6e-5*T
q = 1.6e-19

#----------------------------------------
#defines a list which removes zeros from result list
def remove_false(liste):
   liste = np.delete(liste, np.where(liste == False))
   return liste
```

```
#-----------------------------------------------
#function makes a file of the values extracted
def verdi_fil(name, value_list):
   infile = open (name + ".txt" ,"w")   #creates and opens file, enables writing
   line = infile.write(name + '\n')        #writes a to the file

   for text in value_list:
      line = infile.write(text + '\n')      #writes to the file

   infile.close()                           #closes the file

#------------------------------------------------
#reads from data files
for name in filenames:
   f = open (name + ".txt" ,"r")
   readCSV = csv.reader(f, delimiter='\t')

   v = []
   c = []
   valuelist = []

   for row in readCSV:

      vi = row[2]
      ci = row[0]

      v.append(vi)
      c.append(ci)

   v = np.array(v[1::])
   c = np.array(c[1::])

   V = v.astype(np.float)
   C = c.astype(np.float)
```

```
f.close()
A = np.pi*r**2
valuelist.append("Pad area = %f cm2" %A)


ind = np.zeros(len(V),dtype=bool)



for i in range(len(C)-1):
    if V[i] < V[i+1]:
        ind[i] = 1

ind[-1] = ind[-2]

C_i_measured = max(C)
C_i_theo = eps_alox * A / 20e-7



valuelist.append("C_i_measured = %f F/cm" %C_i_measured)
valuelist.append("C_i_theo = %f F/cm" %C_i_theo)

C_i = C_i_measured # choose the theoretical or the measured value of C_i

Vmp = V*ind
Cmp = C*ind

Vpm = V*[not i for i in ind]
Cpm = C*[not i for i in ind]

Vmp = remove_false(Vmp)
Cmp = remove_false(Cmp)

Vpm = remove_false(Vpm)
```

```
Cpm = remove_false(Cpm)


Ld = np.sqrt(eps_Si * kT / (q * p_dop))

valuelist.append("Ld = %f" % Ld)

Vfb_ideal = workf_Si - aff_Si - 1.12 / 2 + kT*np.log(p_dop/1e10)
valuelist.append( "Vfb_ideal = %f V" %Vfb_ideal)

d_i = (eps_alox * A / C_i) * 1e7



C_i_norm = C_i / A
valuelist.append("C_i_norm = %f F/cm" %C_i_norm )
Cmp_norm = Cmp / A
Cpm_norm = Cpm / A

#Cfb      = 1/(1/(C_i_norm + Ld/eps_Si))

Cfb = eps_Si/Ld
valuelist.append("Cfb = %f" %Cfb)

Vfb_pm = np.interp(Cfb, Cpm_norm, Vpm)

Qf_pm = (Vfb_ideal - Vfb_pm) * C_i_norm / q
Qf_pm_text = format_e(Qf_pm)

valuelist.append("Qf = " + Qf_pm_text )
valuelist.append("Vfb = %f" %Vfb_pm)

ax.plot(Vpm, Cpm_norm,color=colorlist[j], label = (labellist[j]))
ax.axvline(Vfb_pm, 0, 3, linewidth  = 0.3, color = colorlist[j])
```

```
    verdi_fil(labellist[j], valuelist)
    j = j+1

ax.set_xlabel('Bias [V]')
ax.set_ylabel('Capacitance per area [F/$cm^{2}$]')

ax.legend(loc = 'lower left', title="Samples")

plt.show()

fig.tight_layout()
fig.savefig(figname + '.eps', format='eps')
```

Appendix B - Silvaco MIS simulation code

```
go internal
set emitter_thickness = 0
set bulk_thickness = 1.0
set oxide_thickness = 0.001
set poly_thickness = 0.1

# defines y-mesh intervals
set y_int1 =     0
set y_int2 =     $emitter_thickness
set y_postint2 = 2*$emitter_thickness
set y_preint3 =  $emitter_thickness+$bulk_thickness-$oxide_thickness
set y_int3 =     $emitter_thickness+$bulk_thickness
set y_int4 =     $emitter_thickness+$bulk_thickness+$oxide_thickness
set y_postint4 = $emitter_thickness+$bulk_thickness+2*$oxide_thickness
set y_int5 =     $emitter_thickness+$bulk_thickness+$oxide_thickness+$poly_thickness

go atlas

mesh space.mult=1.0  ^diag.flip
# defines mash spacing
x.mesh location=0.0 spacing=10
x.mesh location=20 spacing=10

y.mesh loc=0 spacing=0.05
y.mesh loc=$y_int1 s=0.05
y.mesh loc=$y_int2 s=0.05
y.mesh loc=$y_postint2 s=0.5
y.mesh loc=$y_preint3  s=0.5
y.mesh loc=$y_int3 s=$oxide_thickness*0.1
y.mesh loc=$y_int4  s=$oxide_thickness*0.1
y.mesh loc=$y_postint4 s=0.05
y.mesh loc=$y_int5 s=0.05
```

```
#defines material regions
region num=1 material=silicon  y.min=$y_int1 y.max=$y_int2
region num=1 material=silicon y.min=$y_int2 y.max=$y_int3
region num=2 material=oxide y.min=$y_int3 y.max=$y_int4
region num=3 material=poly y.min=$y_int4 y.max=$y_int5

#ELECTRODES
electrode number=1  name=anode  top
electrode number=2  name=cathode  bottom

#QUANTUM MESH
qtregion number=1 pts.normal=3 pts.tunnel=20 x1=0.0 y1=$y_postint4 x2=20.0 y2=$Y_postint4 x3=20.0 y3=$y_preint3 x4=0.0 y4=$y_preint3

# DOPING
doping uniform n.type conc=2e19 y.min=$y_int1 y.max=$y_int2

doping uniform  p.type conc=2e15 y.min=$y_int2 y.max=$y_int3

doping uniform  p.type conc=2e20 y.min=$y_int4

#defines models used in the simulation
models temperature=300 srh auger print fermi ni.fermi bbt.forward bbt.nlderivs fnord cvt
output band.temp traps u.srh

method climit=1.0 dvmax=0.005
solve init

save outf="Si_SiO2_$"oxide_thickness".str"
tonyplot "Si_SiO2_$"oxide_thickness".str"


log outf=rev_oxide_thickness_$"oxide_thickness".log
#defines voltage sweep – negative direction
solve name=anode vanode=-0.0 vstep=-0.1 vfinal=-3
```

```
log off

solve init

log outf = fwd_oxide_thickness_$"oxide_thickness".log

#defines voltage sweep – positive direction
solve name=anode vanode=0.0  vstep=0.1 vfinal=3

tonyplot -overlay fwd_oxide_thickness_$"oxide_thickness".log rev_oxide_thickness_$"oxide_thickness".log

exit
```